

Simulations of Radiation Pressure Experiments

by

Maximilien Bethune-Waddell

B.A.Sc., The University of British Columbia, 2013

A THESIS SUBMITTED IN PARTIAL FULFILLMENT OF THE
REQUIREMENTS FOR THE DEGREE OF
MASTER OF APPLIED SCIENCE

in

THE COLLEGE OF GRADUATE STUDIES

(Electrical Engineering)

THE UNIVERSITY OF BRITISH COLUMBIA

(Okanagan)

August 2016

© Maximilien Bethune-Waddell, 2016

The undersigned certify that they have read, and recommend to the College of Graduate Studies for acceptance, a thesis entitled:

Simulations of Radiation Pressure Experiments

Submitted by Maximilien Bethune-Waddell in partial fulfillment of the requirements of

The degree of MASc-Electrical Engineering

Dr. Kenneth Chau

Supervisor, Professor (please print name and faculty/school above the line)

Dr. Joshua Brinkerhoff

Supervisory Committee Member, Professor (please print name and faculty/school in the line above)

Dr. Jonathan Holzman

Supervisory Committee Member, Professor (please print name and faculty/school in the line above)

Dr. Ahmed Idris

University Examiner, Professor (please print name and faculty/school in the line above)

Dr. Murray Neuman

External Examiner, Professor (please print name and university in the line above)

August 10th 2016

(Date submitted to Grad Studies)

Additional Committee Members include:

Please print name and faculty/school in the line above

Please print name and faculty/school in the line above

Abstract

Electromagnetic radiation, such as light, can exert a force on objects. This phenomena is referred to as radiation pressure. A popular example would be the radiation pressure from the sun which is presently the only force pushing NASA's Kepler II satellite out of our solar system. The most important material property relevant to radiation pressure is the refractive index n . The vacuum of space around the Kepler satellite has a refractive index of $n = 1$. For this situation our ability to model radiation pressure is quite certain. There has been a debate over the last century on how to model radiation pressure in the presence of matter, where the refractive index of the surrounding medium can be $n > 1$. Five prevalent models exist for electrodynamics, namely the Abraham, Minkowski, Einstein-Laub, Chu, or the Amperian formulations. Various electrodynamic theories presented over the last century have differences that only arise in exotic situations such as objects in liquid environments, material moving at relativistic speeds, and short timescales difficult to measure. Because technology has now advanced to potentially include these situations, this thesis addresses the renewed attention this debate requires. Each of these models are tested against two criteria using a simulation tool that solves for both electromagnetic and fluid dynamic phenomena. First, their compliance with the conservation laws of energy, momentum, and center-of-mass velocity. Second, their accord with experimental results. A simulation environment is used to calculate the conserved quantities and observable effects that each model predicts under various experimental conditions. The simulation tool is a Matlab script that allows us to consider and compare the results of many experiments simultaneously. Five significant experiments are analyzed in this thesis: the radiation pressure observed on metallic and dielectric mirrors, the deformation of a water-air interface, the deformation of a fluid-fluid interface, the displacement of polystyrene beads submerged in water, and the displacement of an oil droplet on a water surface. This thesis reaches the conclusion that not enough data is available from past experiments to verify a single electrodynamic theory. Our work suggests simple new experiments that could.

Preface

This thesis was written under the supervision of Dr. Kenneth Chau, who co-authored the content and planned the analysis. The majority of this thesis represents the work done to create a published article on radiation pressure authored by Dr.Chau and me [1]. The waveguide experiments in Section 4.1 were carried out by Saimoom Ferdous and Dr. Thomas Johnson, a publication is in progress based on the results of their experiments. Two paragraphs within Section 4.1 that describe and discuss the experiments were originally drafted by Saimoom Ferdous and Dr. Thomas Johnson.

Table of Contents

Abstract	iii
Preface	iv
Table of Contents	vi
List of Figures	vii
List of Tables	xi
Acknowledgments	1
Chapter 1: Introduction	1
Chapter 2: Theory	5
2.1 Maxwell's Equations	6
2.2 Energy Continuity and the Poynting Theorem	7
2.3 Momentum Continuity	9
2.3.1 Example Calculation of Force Using the Stress Tensor	13
2.4 Center-of-Mass Velocity Conservation	15
Chapter 3: Methods	16
3.1 Finite-Difference Methods	17
3.1.1 The FDTD Method	18
3.1.2 One-Dimensional Force Discretization and Field Averaging	20
3.1.3 Two-Dimensional Force Discretization	21
3.2 Finite-Difference Methods in Fluid Dynamics	26
Chapter 4: Results	27
4.1 The Balazs Thought Experiment	28
4.1.1 Momentum and Center-of-Mass Calculations	30
4.1.2 An Experimental Variant on the Balazs Thought Experiment	34
4.2 Discussion and Conclusions on the Balazs Thought Experiment	36
4.3 Momentum and Center-of-Mass Conservation For All Five Forms	37

4.4	Conservation in Two Dimensions	40
4.5	Radiation Pressure on Submerged Mirrors	43
4.6	Radiation Pressure at Fluid Interfaces	55
4.7	Optical Tweezing	62
4.8	Radiation Pressure in Negative Index Materials	68
4.8.1	Optical Tweezing With a Negative Index Bead	73
Chapter 5:	Conclusion	74
Appendix A:	Speeding up Matlab Code	77
Bibliography		80

List of Figures

Figure 2.1 Demonstration of a pulse entering a lossy medium and leaving energy behind in the form of work done on the internal charges.	8
Figure 2.2 Differential volume element where the components of stress and shear are displayed for the plane defined with unit normal $+\hat{x}$	12
Figure 2.3 A piece of steel immersed in a magnetic field \vec{B} feels a force proportional to the spatial gradient of the magnetic field.	13
Figure 2.4 Force versus separation z , normalized to the magnet length L . Values agree with simulated results except at very close proximity, where permanent magnet field modeling requires more advanced methods [51].	14
Figure 3.1 Figure showing how the derivative of $f(x)$ can be expressed by the finite difference between two points.	17
Figure 3.2 The numerical error produced when field averaging is not implemented.	22
Figure 3.3 Figure showing the discretized locations of the electromagnetic field and force values on the Yee grid.	22
Figure 3.4 The general algorithm to solve for fluid deformation under radiation pressure.	27
Figure 4.1 Illustration of the Balazs thought experiment.	28
Figure 4.2 A plane wave at the interface between free space and an impedance-matched medium ($\mu_r = \epsilon_r$). The plane wave is shown in terms of \vec{D} and \vec{B} fields to illustrate the discontinuous nature of the Minkowski momentum density. The free space wavevector is described by k_1 and propagation within the impedance-matched medium is described by k_2	30
Figure 4.3 Energy density distributions at three moments in time predicted by the Abraham (a) and the Minkowski (b) postulates, for the case of a pulse normally incident onto a slab under conditions identical to those in Figure 4.4.	31
Figure 4.4 Pulse momentum exchange with an impedance-matched medium.	33

Figure 4.5 (a) Infrared image at 4 minutes showing the temperature at points (1) and (2) on either end of the Teflon segment.(b) The waveguide experimental setup where a 13.56 MHz source propagates a TEM wave in the \vec{k} direction along an impedance-matched waveguide that is terminated with a matched load.	35
Figure 4.6 Salient dimensions for the impedance-matched waveguide labeled on the waveguide with their values tabulated. This configuration represents a close analogue to the impedance-matched medium of the Balazs thought experiment.	36
Figure 4.7 Simulations of the Minkowski, Abraham, Einstein-Laub, Amperian, and Chu postulates with conservation of momentum and center-of-mass velocity.	38
Figure 4.8 Instantaneous energy density distributions at three moments in time predicted by (a) the Abraham, Einstein-Laub, and Chu postulates, (b) the Minkowski postulates, and (c) the Amperian postulates, for the case of a pulse normally incident onto a slab under conditions identical to those in Figure 4.7.	39
Figure 4.9 Two-dimensional field-based implementation of the Balazs thought experiment.	41
Figure 4.10 Non-degenerate center-of-mass displacement predictions made by the Minkowski (MN), Abraham (AB), Einstein-Laub (EL), Chu, and Amperian (AMP) postulates for closed systems in which finite pulses are obliquely incident onto tilted impedance-matched slabs having (a) $n = \sqrt{3}$ (blue) and (b) $\tilde{n} = -1.3 + i0.07$ (yellow).	42
Figure 4.11 Momentum transfer between a pulse ($\lambda_0 = 632$ nm, $\tau = 2$ fs) in an enclosure containing a fluid ($n = 1.6$) and a submerged mirror approximated as a perfect electric conductor.	45
Figure 4.12 Momentum transfer between a pulse ($\lambda_0 = 632$ nm, $\tau = 2$ fs) in an enclosure containing a fluid ($n = 1.6$) and a submerged mirror approximated as a perfect magnetic conductor.	47
Figure 4.13 Key assumptions used to model the Jones-Richards experiment.	49
Figure 4.14 Normalized time-averaged radiation pressure on submerged mirrors predicted by the Minkowski, Abraham, Einstein-Laub, Chu, and Amperian postulates.	51

Figure 4.15 Time-averaged force density distributions predicted by the Minkowski, Abraham, Einstein-Laub, Chu, and Amperian postulates, shown for the case of a continuous-wave beam ($\lambda_0 = 632.8$ nm) normally incident onto a dielectric mirror composed of alternating $\lambda_0/4$ -thick layers of MgF ₂ and ZnS submerged in a fluid of refractive index $n = 1.6$	53
Figure 4.16 Normalized radiation pressure on a submerged dielectric mirror predicted by the Einstein-Laub, Chu, and Amperian postulates as a function of the force density integration distance into the fluid for cases in which the dielectric mirror is capped by either the lower-index layer (blue solid) or the higher-index layer (red dashed).	54
Figure 4.17 Instantaneous (top row) and time-averaged (bottom row) electromagnetic force density distribution exerted by a continuous-wave beam ($\lambda_0 = 632.8$ nm) normally incident from air onto water ($n = 1.33$) predicted by (a) the Abraham (solid blue) and Minkowski (dashed red) postulates and (b) the Einstein-Laub and Chu postulates (solid black) and the Amperian postulates (dashed orange).	57
Figure 4.18 Two-dimensional fluid dynamic simulations representative of the Ashkin-Dziedzic experiment [15]. The lower fluid (blue) represents water ($n=1.33$) and the upper fluid (white) represents air ($n=1$).	59
Figure 4.19 Two-dimensional fluid dynamic simulations representative of the experiments by Casner et al. [19, 20].	61
Figure 4.20 Simulated radiation pressure on a polystyrene bead (green) placed at the edge of the focal point of a continuous-wave beam ($\lambda_0 = 532$ nm) in a background medium of water ($n = 1.33$).	64
Figure 4.21 Simulated dynamics of an air bubble placed at the edge of the focal point of a TM-polarized, continuous-wave beam ($\lambda_0 = 532$ nm) in a background medium of water ($n = 1.33$, $\sigma = 0.7$ mN/m, $\eta = 1$ mPa·s).	65
Figure 4.22 Tractor beaming of an oil droplet ($n = 1.42$) resting at the interface between air ($n = 1.0$) and water ($n = 1.33$).	66
Figure 4.23 Tractor beaming of a dielectric particle using two obliquely incident plane waves.	67
Figure 4.24 A perfectly absorbing enclosure is partially filled with a negative-index slab.	69
Figure 4.25 A perfectly absorbing enclosure is filled with negative index fluid and an Ag mirror.	71

Figure 4.26 Demonstration of the momentum a mirror experiences with respect to its surrounding refractive index. All forms predict degenerate results for a refractive index $n > 1$, but differences arise for $n < 1$.	72
Figure 4.27 Optical tweezing of an impedance matched negative index bead under TM illumination.	73
Figure 5.1 A minimum working example (MWE) to demonstrate how to use handles to update a figure as opposed to re-calling the “figure” function. The code above will produce a figure of a simple sine wave.	78
Figure 5.2 An example to demonstrate how vectorizing for loops improves the speed of matlab code.	79

List of Tables

Table 1.1 : Momentum density, stress tensor, and power flux corresponding to the Minkowski, Abraham, Einstein-Laub, Amperian, and Chu formulations of electrodynamics.

Acknowledgments

Foremost, I would like to acknowledge Dr. Kenneth Chau for his unwavering support, motivational character, dedication to quality, and for being a good example as a human being. The mindset and skills I have developed by working under Ken have proven my most valuable assets and will surely continue to shape my professional and personal life for the better. Ken and I had a lot of fun during this work exploring different aspects of science ranging from the fundamentals of quantum mechanics, the nature of absorption, the mysteries of radiation pressure, and in developing numerical methods for electrodynamic modeling.

As well, I would like to thank Dr. Joshua Brinkerhoff for his contribution to the fluid dynamics portion of this thesis and his role as a committee member. Also, a thank you to Dr. Jonathan Holzman for his thoughtful comments in reviewing this thesis and letting me join his lab's lunch meetings, where I have developed many friendships and gained exposure to teamwork driven experiments. I would additionally like to thank Dr. Stephen O'Leary for his role in creating a Mitacs internship where I have applied the simulation tools of this thesis in an industry setting. Another acknowledgment to Ken, Holzman, and Stephen for their roles as academic supervisors during the various research projects I have completed over the last five years during my undergraduate and graduate degrees. These projects have led to me being awarded an NSERC PGS-D scholarship. I will use this scholarship to further my understanding of nature and contribute to reducing society's entropy under a subsystem assumption. Lastly, I have enjoyed the good company of my fellow graduate students and want acknowledge the influence of Waqas Maqsood, Reyad Mehfuz, Samuel Schaefer, Naomi Fredeen, Mohammed Al Shakhs, Asif Al Noor, Brandon Born, Iman Aghanejad, and Chris Collier.

Chapter 1: Introduction

In the early 1900s, works such as James Maxwell's treatise [2] developed most of the theory behind our present understanding of electromagnetic phenomena. One of the most important results within Maxwell's work was the proof that light was an electromagnetic wave carrying momentum, meaning they could exert a force via Newton's first law. This led Maxwell to predict light could produce a pressure on objects, a phenomenon now referred to as radiation pressure. Shortly after Maxwell's prediction, measurements of mirror deflection due to incident radiation from a vacuum [3, 4, 5] confirmed the existence of radiation pressure. In vacuum, mass-energy equivalence ($E = mc^2$) and the definition of linear momentum can be combined to show that the momentum of light is related to its energy content via $p = E/c$. Experiments in vacuum have confirmed that a mirror gains momentum of $2E/c$ due to the change in momentum upon reflection. In the presence of matter, competing theories have been introduced to model radiation pressure. Authors such as Minkowski [6] and Abraham [7] began a now century-old debate over how to model the momentum density of light in matter. Minkowski proposed a form of momentum density given by $\vec{D} \times \vec{B}$, with \vec{D} representing the displacement field and \vec{B} the magnetic flux density. On the other hand, Abraham introduced a form given by $(\vec{E} \times \vec{H})/c^2$, with \vec{E} representing the electric field, \vec{H} the magnetic field, and c the speed of light. Although identical in vacuum, the Abraham and Minkowski forms give divergent predictions of the electromagnetic momentum density in matter. If we consider an electromagnetic wave entering a dielectric medium of refractive index n from free space, the Minkowski form predicts an electromagnetic momentum increase proportional to n , whereas the Abraham form predicts an electromagnetic momentum decrease proportional to $1/n$. Dichotomy between the theories of Abraham or Minkowski became known as the Abraham-Minkowski controversy. This debate has grown in scope over the past century to include alternative electrodynamic theories such as the Einstein-Laub, Amperian, and Chu formulations [8, 9, 10, 11, 12].

Among these electrodynamic theories, compelling claims have been made in support of either the Minkowski or Abraham forms of electromagnetic momentum. Experimental measurements of radiation pressure on submerged mirrors [13, 14], fluid interfaces [15, 16, 17, 18, 19, 20], semiconductors carriers [21, 22, 23], and dilute atom gases [24] have consistently revealed a refractive-index proportionality most commonly interpreted to support the Minkowski momentum density [25, 26, 27, 28]. On the other hand, convincing theoretical arguments have been developed in support of the Abraham momentum density. Balazs [29] put forward an extension of the Einstein photon-in-box thought experiment [30] to show that only the Abraham momentum density preserves linear center-of-mass translation in a closed system consisting of a rigid, reflection-less dielectric block and an electromagnetic pulse. Center-of-mass translation, in combination with energy and momentum, is a quantity that must be conserved for a closed system [30, 31]. Strong evidence for the Minkowski and Abraham momentum densities has led to an acceptance of the potential correctness of both [26, 32, 27, 33] and a heuristic approach to their application: The Minkowski or “wave” momentum can be used to predict radiation pressure phenomena, whereas the Abraham or “kinetic” momentum can be used to predict center-of-mass translations [34, 35, 36, 37, 38, 39].

In the 1960s, Penfield and Haus [11] showed that multiple electrodynamic formulations can be consistent with global energy and momentum conservation by separating a closed system into sub-systems. For example, a closed system containing matter and electromagnetic fields could be broken down into a kinetic sub-system describing the mechanical motion of matter, a thermodynamic sub-system describing the energy flow in matter, and an electrodynamic sub-system describing the momentum and energy stored in the fields. Each sub-system is modeled using energy and momentum continuity equations, which take on the generic forms

$$\nabla \cdot \vec{S} + \frac{\partial}{\partial t} W = -\phi, \quad (1.1)$$

and

$$\nabla \cdot \bar{\vec{T}} + \frac{\partial}{\partial t} \vec{G} = -\vec{f}. \quad (1.2)$$

where $\bar{\vec{T}}$ is the stress tensor, \vec{G} the electromagnetic momentum density, \vec{f} the force density, \vec{S} the energy flux density, W the energy density, and ϕ the power density. In a closed system, the continuity equations of the various sub-systems, indexed by the variable l , are coupled so that

$$\Sigma \phi_l = 0, \quad (1.3)$$

and

$$\Sigma \vec{f}_l = 0, \quad (1.4)$$

which means that energy and momentum move between systems via ϕ_l and \vec{f}_l to enable the entire model to conserve energy and momentum.

Attempts were made in the mid-1900's [13, 14, 15] to test different postulates of momentum by measuring radiation pressure on illuminated objects, but consistent interpretation of these experiments has been elusive. Radiation pressure on submerged mirrors [14], for example, has been explained in terms of the Minkowski momentum [25, 26, 27, 28], the Abraham momentum [40], the arithmetic mean of the two [41, 42, 43, 44], or a canonical momentum of quantum mechanical origins [45]. To reconcile the disparate literature, two mutually-exclusive hypotheses have emerged: either the definition of momentum is totally arbitrary and there are many simultaneously valid electrodynamic theories [33, 46, 47, 39] or there is a single theory that uniquely predicts observable phenomena but has escaped experimental detection [48]. This thesis presents evidence to argue the latter.

A consolidated analysis is performed on the five electrodynamics theories mentioned so far (namely: Abraham (AB), Minkowski (MN), Amperian (AMP), Einstein-Laub (EL), and Chu) to investigate their theoretical and experimental consistency. Table 1.1 shows each of their respective combinations of stress tensor, power flux density, and momentum density.

Table 1.1 . Momentum density, stress tensor, and power flux corresponding to the Minkowski, Abraham, Einstein-Laub, Amperian, and Chu formulations of electrodynamics. [†]The Minkowski energy-momentum tensor is presented in its classical asymmetric form [6, 49] as well as it's symmetric form using a power flux of $c^2 \vec{D} \times \vec{B}$ [8].

Form	Momentum Density	Power Flux	Stress Tensor
Minkowski [†]	$\vec{D} \times \vec{B}$	$\vec{E} \times \vec{H}$	$(\vec{D} \cdot \vec{E} + \vec{B} \cdot \vec{H}) \bar{I}/2 - \vec{D}\vec{E} - \vec{B}\vec{H}$
Abraham	$\vec{E} \times \vec{H}/c^2$	$\vec{E} \times \vec{H}$	$[(\vec{D} \cdot \vec{E} + \vec{B} \cdot \vec{H}) \bar{I} - \vec{D}\vec{E} - \vec{B}\vec{H} - \vec{E}\vec{D} - \vec{H}\vec{B}]/2$
Einstein-Laub	$\vec{E} \times \vec{H}/c^2$	$\vec{E} \times \vec{H}$	$(\varepsilon_o \vec{E}^2 + \mu_o \vec{H}^2) \bar{I}/2 - \vec{D}\vec{E} - \vec{B}\vec{H}$
Amperian	$\varepsilon_o \vec{E} \times \vec{B}$	$\vec{E} \times \vec{B}/\mu_o$	$(\varepsilon_o \vec{E}^2 + \mu_o^{-1} \vec{B}^2) \bar{I}/2 - \varepsilon_o \vec{E}\vec{E} - \mu_o^{-1} \vec{B}\vec{B}$
Chu	$\vec{E} \times \vec{H}/c^2$	$\vec{E} \times \vec{H}$	$(\varepsilon_o \vec{E}^2 + \mu_o \vec{H}^2) \bar{I}/2 - \varepsilon_o \vec{E}\vec{E} - \mu_o \vec{H}\vec{H}$

In this thesis, Section outlines the fundamental theory of how energy and momentum conservation is modeled for electromagnetic field quantities. Section uses numerical methods to solve for field and force density, and explains them in detail, as they are used to present the results. These methods are implemented using finite-difference techniques. Using this solver, results are presented as numerical calculation of various important radiation pressure experiments conducted to date. First, we re-visit Balazs' thought experiment in Section 4.1 to demonstrate its bias towards favoring the Abraham momentum density using arguments of center-of-mass translation. Following this, numerical methods are further used in Sections 4.5- 4.8 to recreate the results from experiments on fluid-submerged mirrors, radiation-induced deformation of fluid interfaces, the manipulation of small dielectric particles by laser beams, and a thought experiment concerning radiation pressure in negative index media. Our calculations show that all five postulates can be made consistent with conservation laws; however, not all forms are consistent with experimental results. In particular, the postulates proposed by Abraham and Einstein-Laub are shown to have the most consistency with all radiation pressure experiments considered.

Chapter 2: Theory

2.1 Maxwell's Equations

As we are concerned with electromagnetic fields, the most fundamental equations to consider are Maxwell's equations, namely: Ampere's law, Faraday's law, Gauss's law, and Gauss's law for magnetics, given by 2.1 to 2.4.

$$\nabla \times \vec{H} = \frac{\partial}{\partial t} \vec{D} + \vec{J}, \quad (2.1)$$

$$\nabla \times \vec{E} = -\frac{\partial}{\partial t} \vec{B} + \vec{J}_m^1, \quad (2.2)$$

$$\nabla \cdot \vec{D} = \rho, \quad (2.3)$$

and,

$$\nabla \cdot \vec{B} = 0, \quad (2.4)$$

respectively, where \vec{E} is the electric field, \vec{H} the magnetic field strength, \vec{J} the current density, and \vec{J}_m the magnetic current density. These equations completely describe the spatial and temporal evolution of electromagnetic field quantities in the presence of sources.

The force on a test charge q can be described by the Lorentz force density

$$\vec{f} = q\vec{E} + q\vec{v} \times \vec{B}, \quad (2.5)$$

where the charge q experiences force components due to electric and magnetic fields. Because the force contribution of the magnetic field component is perpendicular to the direction of particle motion, the magnetic field can not do work on moving charges. It will be shown in later sections that this is different than situations where magnetic fields *can* do work such as in the case of magnetic materials. The description of motion resulting from electromagnetic influences is the study of electrodynamics. A correct electrodynamic theory

¹does not exist, but provides a mathematical tool for useful features numerically, for example a perfectly matched layer.

must obey conservation of energy, momentum, and center-of-mass velocity. Conservation of energy for an electromagnetic system is mathematically stated as

$$\int_v (\nabla \cdot \vec{S}) dv + \int_v (\frac{\partial}{\partial t} W) dv = - \int U_w dv, \quad (2.6)$$

where \vec{S} is the power flux density in [W/m²], W_{tot} is the energy density, and U_w is the work done between the fields and any free charges. Any electrodynamic theory must also obey conservation of momentum

$$\int_v (\nabla \cdot \bar{\bar{T}}) dv + \int_v (\frac{\partial}{\partial t} \vec{G}) dv = - \int \vec{f} dv, \quad (2.7)$$

where $\bar{\bar{T}}$ is the stress tensor [Pa], \vec{G} the electromagnetic momentum density [Kg/(s · m²)], and \vec{f} the force density [N/m³]. All quantities in equations 2.6 and 2.7 are assumed here to only be associated with interaction between fields and charges, meaning they will only consist of field and current density values. However it should be noted these equations are generalizable to many different systems. For example, the Navier-Stokes equation that describes fluid dynamics is derived from momentum continuity very similar to equation 2.7.

2.2 Energy Continuity and the Poynting Theorem

Equation 2.6 is called Poynting's theorem [50]. Derivation of \vec{S} and W for an electromagnetic system will typically start with an expression for the work done by the fields. As previously mentioned only electric fields can do work on charges. Using this principle we can generalize the work done, U_w , as a function of only the electric field \vec{E} and the current density \vec{J} as

$$U_w = \int_v (\vec{J} \cdot \vec{E}) dv, \quad (2.8)$$

which can be inserted into equation 2.6 by integrating over an area A_c that encloses v to give

$$\int_{A_c} (\vec{S} \cdot \hat{n}) dA + \int_v (\frac{\partial}{\partial t} W) dv = - \int_v (\vec{J} \cdot \vec{E}) dv. \quad (2.9)$$

We can further re-arrange equation 2.9 using Maxwell's equations to arrive at expressions for W and \vec{S} based only on field quantities. Substituting Ampere's law and setting $\vec{J} = \nabla \times \vec{H} - \frac{\partial}{\partial t} \vec{D}$ along with the vector identity $\nabla \cdot (\vec{E} \times \vec{H}) = \vec{H} \cdot (\nabla \times \vec{E}) - \vec{E} \cdot (\nabla \times \vec{H})$ gives

$$-\int_v (\vec{J} \cdot \vec{E}) dv = \int_v (\nabla \cdot (\vec{E} \times \vec{H})) + \frac{\partial}{\partial t} \frac{1}{2} [\vec{E} \cdot \vec{D} + \vec{H} \cdot \vec{B}] dv. \quad (2.10)$$

Identification of the terms on the right side leads us to the conventional expression for the Poynting vector

$$\vec{S} = \vec{E} \times \vec{H}, \quad (2.11)$$

and energy density,

$$W = \frac{1}{2} [\vec{E} \cdot \vec{D} + \vec{H} \cdot \vec{B}]. \quad (2.12)$$

Equation 2.10 can now be used to describe wave dynamics in lossy systems. For example, Figure 2.1 depicts a pulse initially entering a system with 1 J and leaving behind half of its energy due to damping associated with induced charge movement. This loss can be calculated either directly using equation 2.8, or with only field values using equation 2.12. The best way will depend on what numerical or analytical technique is being used. For most numerical methods the fields (\vec{E} , \vec{D} , \vec{B} , and \vec{H}) are more readily available than the current density, making equation 2.12 a preferred choice to solve for the energy density.

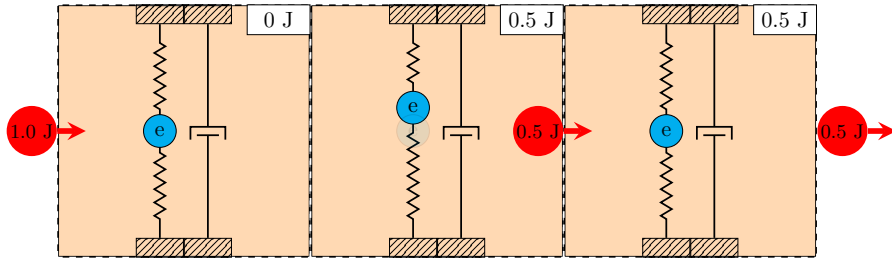


Figure 2.1: Demonstration of a pulse entering a lossy medium and leaving energy behind in the form of work done on the internal charges.

2.3 Momentum Continuity

We next explore the implications of momentum continuity by examining equation 2.7

$$\int_{A_c} (\nabla \cdot \bar{\bar{T}}) dA + \int_v \left(\frac{\partial}{\partial t} \vec{G}_{tot} \right) dv = - \int \vec{f} dv.$$

The stress tensor, $\bar{\bar{T}}$, is a second rank tensor and its divergence results in a vector with \hat{x} , \hat{y} , and \hat{z} components. The approach to derive the conventional forms of the Maxwell stress tensor $\bar{\bar{T}}$ is to start by equating the force density in equation 2.7 to the Lorentz force density in equation 2.5,

$$\int_v \vec{f} dv = \int_v (\rho \vec{E} + \vec{J} \times \vec{B}) dv. \quad (2.13)$$

We assume our expression for \vec{f} is solely responsible for any mechanical momentum and can then parse \vec{G}_{tot} into mechanical and electromagnetic parts, $\vec{G}_{tot} = \vec{G}_{EM} + \vec{G}_{mech}$. For now we assume there is no mechanical component to $\bar{\bar{T}}$ but note that many models incorporate a view where $\bar{\bar{T}} = \bar{\bar{T}}_{EM} + \bar{\bar{T}}_{mech}$ and argue that the use of $\bar{\bar{T}}_{mech}$ is how different forms of momentum density can be proven to be equivalent [33]. For now we will assume only an electromagnetic component to the stress tensor. To derive $\bar{\bar{T}}$ and G_{EM} one can plug $\rho = \varepsilon_o \nabla \cdot \vec{E}$ and $\vec{J} = \frac{1}{\mu_o} (\nabla \times \vec{B}) - \varepsilon_o \frac{\partial}{\partial t} \vec{E}$ into equation 2.13 to get

$$\int_{A_c} (\nabla \cdot \bar{\bar{T}}) dA + \int_v \left(\frac{\partial}{\partial t} \vec{G}_{EM} \right) dv = - \int \left(\frac{d}{dt} \vec{G}_{mech} \right) dv = - \int_v \vec{f} dv \quad (2.14)$$

and

$$\int_v \vec{f} dv = \int_v \varepsilon_o [\vec{E}(\nabla \cdot \vec{E}) - c^2 (\vec{B} \times (\nabla \times \vec{B})) + \vec{B} \times \frac{\partial}{\partial t} \vec{E}] dv.$$

Next, we use the identity $\vec{B} \times \frac{\partial}{\partial t} \vec{E} = - \frac{\partial}{\partial t} \vec{E} \times \vec{B} + \vec{E} \times \frac{\partial}{\partial t} \vec{B}$ and add $c^2 (\nabla \cdot \vec{B}) = 0$ to get

$$\int_v \vec{f} dv = \int_v \varepsilon_o [\vec{E}(\nabla \cdot \vec{E}) - \vec{E} \times (\nabla \times \vec{E}) - c^2 (\vec{B} \times (\nabla \times \vec{B})) + c^2 \vec{B}(\nabla \cdot \vec{B}) - \frac{\partial}{\partial t} (\vec{E} \times \vec{B})] dv,$$

which can be re-written as

$$\begin{aligned} & - \int_v \varepsilon_o [\vec{E}(\nabla \cdot \vec{E}) - \vec{E} \times (\nabla \times \vec{E}) + c^2 \vec{B}(\nabla \cdot \vec{B}) - c^2 (\vec{B} \times (\nabla \times \vec{B}))] dv + \varepsilon_o \mu_o \int_v \frac{\partial}{\partial t} (\vec{E} \times \vec{H}) dv \\ & = - \int_v \vec{f} dv. \end{aligned} \quad (2.15)$$

From the left-hand side of equation 2.3, we can identify the momentum density

$$\vec{G}_{EM} = \frac{1}{c^2}(\vec{E} \times \vec{H})$$

and in order to view our expression as a continuity equation we need to re-phrase the other terms to fit into a stress tensor

$$\nabla \cdot \bar{T} = - \int_v \varepsilon_o [\vec{E}(\nabla \cdot \vec{E}) - \vec{E} \times (\nabla \times \vec{E}) + c^2 \vec{B}(\nabla \cdot \vec{B}) - c^2 (\vec{B} \times (\nabla \times \vec{B}))] dv. \quad (2.16)$$

We consider only the x -component of the electric terms, knowing that similar analysis can be carried out for the other components. Development of equation 2.3 gives the \hat{x} -component of

$$\begin{aligned} & [\vec{E}(\nabla \cdot \vec{E}) - \vec{E} \times (\nabla \times \vec{E})] \hat{x} \\ &= E_x \left(\frac{\partial}{\partial x} E_x + \frac{\partial}{\partial y} E_y + \frac{\partial}{\partial z} E_z \right) \hat{x} - E_y \left(\frac{\partial}{\partial x} E_y - \frac{\partial}{\partial y} E_x \right) + E_z \left(\frac{\partial}{\partial z} E_x + \frac{\partial}{\partial x} E_z \right) \hat{x} \end{aligned} \quad (2.17)$$

and now we add $0 = \frac{1}{2} \frac{\partial}{\partial x} E_x^2 - \frac{1}{2} \frac{\partial}{\partial x} E_x^2$ and group the product rule terms to get

$$\frac{\partial}{\partial x} E_x^2 + \frac{\partial}{\partial y} E_x E_y + \frac{\partial}{\partial z} E_x E_z - \frac{1}{2} \frac{\partial}{\partial x} (E_x^2 + E_y^2 + E_z^2).$$

This same form repeats for each Cartesian component to give

$$[\vec{E}(\nabla \cdot \vec{E}) - \vec{E} \times (\nabla \times \vec{E})] \hat{\alpha} = \sum_{\beta=[x,y,z]} \frac{\partial}{\partial \beta} (E_\alpha E_\beta - \frac{1}{2} (\vec{E} \cdot \vec{E}) \delta_{\alpha\beta}) \quad (2.18)$$

and

$$\delta_{\alpha\beta} = \begin{cases} 1 & \text{if } \alpha = \beta \\ 0 & \text{else} \end{cases}. \quad (2.19)$$

Equations 2.18 and 2.19 describe the divergence of a second rank tensor. When expanded, the notation for each component is given by

$$\nabla \cdot T_{\alpha\beta} = \nabla \cdot \begin{bmatrix} T_{xx} & T_{xy} & T_{xz} \\ T_{yx} & T_{yy} & T_{yz} \\ T_{zx} & T_{zy} & T_{zz} \end{bmatrix}, \quad (2.20)$$

where, for example, the x components T_{xx} , T_{xy} , and T_{xz} would be stated as

$$\begin{aligned}
T_{xx} &= \varepsilon_o [E_x^2 - \frac{1}{2}(E_x^2 + E_y^2 + E_z^2)] \\
T_{xy} &= \varepsilon_o [E_x E_y] \\
T_{xz} &= \varepsilon_o [E_x E_z]
\end{aligned} \quad . \quad (2.21)$$

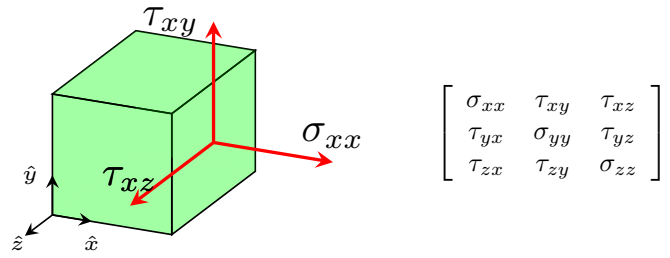
The total electric-field-dependent components for all terms in equation 2.3 are

$$\begin{bmatrix} [E_x^2 - \frac{1}{2}(E_x^2 + E_y^2 + E_z^2)] & [E_x E_y] & [E_x E_z] \\ [E_y E_x] & [E_y^2 - \frac{1}{2}(E_x^2 + E_y^2 + E_z^2)] & [E_y E_z] \\ [E_z E_x] & [E_z E_y] & [E_z^2 - \frac{1}{2}(E_x^2 + E_y^2 + E_z^2)] \end{bmatrix} . \quad (2.22)$$

Through a similar derivation, the magnetic-field-dependent components of equation 2.3 are

$$\begin{bmatrix} [B_x^2 - \frac{1}{2}(B_x^2 + B_y^2 + B_z^2)] & [B_x B_y] & [B_x B_z] \\ [B_y B_x] & [B_y^2 - \frac{1}{2}(B_x^2 + B_y^2 + B_z^2)] & [B_y B_z] \\ [B_z B_x] & [B_z B_y] & [B_z^2 - \frac{1}{2}(B_x^2 + B_y^2 + B_z^2)] \end{bmatrix} . \quad (2.23)$$

Each of these terms are the electromagnetic contributions to the components of shear, τ , and normal force, σ , within a volume density. For example, Figure 2.2 shows a small differential volume element with components of normal force, σ_{ij} , and shear, τ_{ij} . If we consider a differential cube such as in Figure 2.2, each face of that particle has a normal force and a shearing force. The first subscript, i , defines the normal axis plane, and the second subscript j refers to the force direction on that plane. Shown in Figure 2.2 are the components associated with the plane normal to the x -axis, where the shear on this plane in the \hat{z} direction is given by τ_{xz} , the shear in \hat{y} direction is given by τ_{xy} and the force normal to this plane is σ_{xx} . This treatment can be applied to all six faces of the particle.



$$\begin{bmatrix} \sigma_{xx} & \tau_{xy} & \tau_{xz} \\ \tau_{yx} & \sigma_{yy} & \tau_{yz} \\ \tau_{zx} & \tau_{zy} & \sigma_{zz} \end{bmatrix}$$

Figure 2.2: Differential volume element where the components of stress and shear are displayed for the plane defined with unit normal $+\hat{x}$.

2.3.1 Example Calculation of Force Using the Stress Tensor

Equation 2.7 is not used often in electromagnetics as a means to calculate force. Typically, the Lorentz force equation 2.5 is used directly. To understand this equation, we can consider it within a simple situation where electric and magnetic fields are not time varying. In Figure 2.3, a piece of steel is immersed in a static magnetic field \vec{B} . We wish to calculate the attraction between a bar magnet and a piece of steel. There is no electric field present, to simplify analysis further we can assume the magnetic field is $\vec{B} = B_o \hat{z}$ in free space and $B_o/\mu_r \hat{z}$ in the steel which has relative permeability μ_r . Under these assumptions, equation 2.7 has no time derivative terms and becomes

$$\int_v (\nabla \cdot \bar{T}) dv = - \int_v \vec{f} dv. \quad (2.24)$$

Force exists only where $(\nabla \cdot \bar{T})$ is non-zero. This occurs at the interface between steel and air. Using the B_z dependent terms of equation 2.23, we can solve for the force as an integral at the surface of the steel. If we consider the bottom face of the steel to have surface area S' , the force on this surface is

$$\int_v (\nabla \cdot \bar{T}) dv = \int_v -\vec{f} dv = \int_v \left(-\frac{\partial}{\partial z} \frac{B_z^2}{2\mu_0} \right) dv = F \hat{z}.$$

Assuming dz straddles the interface equally from $-dz/2$ to $dz/2$, the net force F is

$$F = \frac{1}{2\mu_0} \left[B_o^2 - \frac{B_o^2}{\mu_r} \right] S'. \quad (2.25)$$

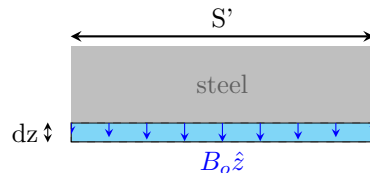


Figure 2.3: A piece of steel immersed in a magnetic field \vec{B} feels a force proportional to the spatial gradient of the magnetic field.

Equation 2.3.1 can be interpreted as a “gradient” force due to the spatial variation in \vec{B} . As well this force is associated with the work done in moving the steel a small dz within the external magnetic field [51]. This example is comparatively simpler then using the Lorentz force density, which would involve modeling the steel as a volume density of circulating current loops. Using equation 2.3.1, the force on steel from a permanent magnet as a function of distance is shown below in Figure 2.4. Experimental measurements of the magnet force data was obtained from a permanent magnet manufacturer [52].

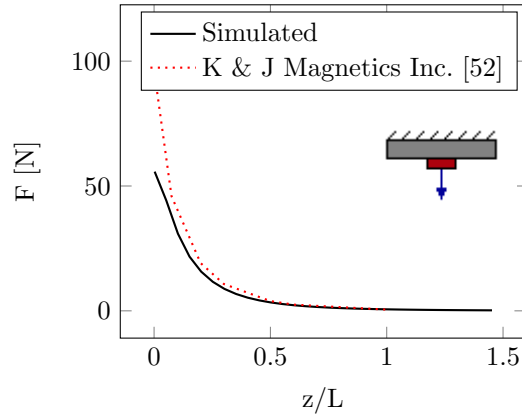


Figure 2.4: Force versus separation z , normalized to the magnet length L . Values agree with simulated results except at very close proximity, where permanent magnet field modeling requires more advanced methods [51].

2.4 Center-of-Mass Velocity Conservation

The final fundamental requirement we shall consider for a good electrodynamic theory is center-of-mass conservation. First, consider a system of two particles m_1 and m_2 , moving at respective speeds of v_1 and v_2 in the \hat{x} direction. Conservation of linear momentum for this system gives

$$(m_1 \vec{v}_1 + m_2 \vec{v}_2) = P \hat{x}, \quad (2.26)$$

where \vec{P} is the total linear momentum of the two particles. The global center-of-mass equation with respective particle locations of x_1 and x_2 would be

$$m_1 x_1 + m_2 x_2 = (m_1 + m_2) \bar{x}. \quad (2.27)$$

where \bar{x} is the system center-of-mass location. The center-of-mass velocity is then the time derivative of this equation,

$$m_1 \frac{dx_1}{dt} + m_2 \frac{dx_2}{dt} = (m_1 + m_2) \frac{d\bar{x}}{dt} = P. \quad (2.28)$$

We have now made the left-hand side of equation 2.28 equal to the constant momentum of the system \vec{P} , meaning that conservation of linear momentum will also yield conservation of the system center-of-mass velocity. This demonstrates that conservation of momentum and center-of-mass velocity are linked for a system of particles, as equation 2.26 was derived from equation 2.28. However, these two conservation laws cannot be considered mutual for electromagnetics because the definition of electromagnetic mass. For example the electromagnetic mass of a pulse could be calculated as

$$m_e = \int_v W(x, y, z)/c^2 dv, \quad (2.29)$$

where $W(x, y, z)$ is the spatial distribution of the electromagnetic energy density. This leaves the possibility that a spatial distribution of W will conserve global linear momentum with total momentum m_e but not center-of-mass velocity. This idea has been considered by authors such as Balazs in [29, 53]. As this is a discussion on mass and energy, Einstein's mass-energy equivalence $E = mc^2$ can be stated for electromagnetic fields as

$$\vec{S} = \vec{G} c^2. \quad (2.30)$$

This equivalence of power flux density \vec{S} and momentum density \vec{G} can be found in [54, pg. 27 §9], and in more detail related to fields in [31, pg. 260 §75]. Modern texts in electrodynamics such as [55, pg. 285 sect. 11.11] and [56, pg. 269 sect 12.5] present that power flux density and momentum density are in general related by a factor of c^2 in both vacuum and matter. The implementation of equation 2.4 for a given \vec{G} is said to be a “symmetric” consideration [57, 49, 31]. Although the relation of symmetry to center-of-mass conservation was derived by Einstein in relation to relativity [30], we will show in Section 4.1 that it affects predicted observables for classical phenomena.

Chapter 3: Methods

3.1 Finite-Difference Methods

Many engineering problems are too complex to be done analytically. Computers have enabled us to simulate these problems using numerical methods. Heat transfer, fluid mechanics, and electromagnetics, each have a governing set of differential equations that can be numerically solved using finite difference methods. The underlying principle behind the finite difference method is shown in Figure 3.1. The derivative of a function $f(x)$ can be expressed as the “finite difference” between two points. A smaller step size, Δx , means a more accurate finite difference. Shown is a plot of $f(x) = x^2$, if an initial value of the function at some x_c is known, its neighboring values can be found via $f(x_c \pm \Delta x) \approx f(x_c) \pm f'(x_c)\Delta x$. This is the basic concept behind all finite difference methods. The more formal definition of a finite difference, and its accuracy, is related to the Taylor series expansion [58, pg. 104].

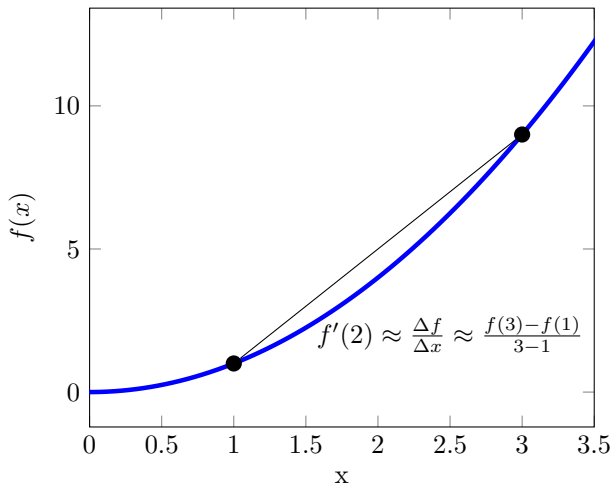


Figure 3.1: Figure showing how the derivative of $f(x)$ can be expressed by the finite difference between two points. As seen, the larger the step size between points, the more inaccurate the finite difference.

3.1.1 The FDTD Method

The Finite-Difference-Time-Domain (FDTD) method is one of the most well developed finite difference methods in computational electromagnetics. A full and complete account of its implementation can be found in [59]. As the name suggests, it is a time-domain technique, the equations used are the time-dependent Ampere's law 2.1 and Faraday's law 2.2. We will derive the FDTD equations in 1D, assuming a plane wave with only H_y and E_x components propagating in the \hat{z} direction. Amperes law simplifies to

$$\frac{\partial}{\partial z} H_y = \varepsilon_o \frac{\partial}{\partial t} E_x.$$

Next, we discretize space and time choosing index i for space and index n for time. For notation purposes we will assume spatial separation is expressed by Δz and time separation by Δt . We need to place the fields somewhere within these indexes, we will put H_y in time at $n + \frac{1}{2}$ and take its spatial derivative at i ,

$$\left[\frac{\partial}{\partial z} H_y^{n+\frac{1}{2}} \right]_i = \frac{1}{\Delta z} \left[H_y^{n+\frac{1}{2}}(i + \frac{1}{2}) - H_y^{n+\frac{1}{2}}(i - \frac{1}{2}) \right] = \varepsilon_r(i) \varepsilon_o \left[\frac{\partial}{\partial t} E_x(i) \right]_{n+\frac{1}{2}}.$$

To be consistent with our notation taking the time derivative at i forces us to place the centered difference of H_y between $(i + \frac{1}{2})$ and $(i - \frac{1}{2})$. If assume H_y exists at $n + \frac{1}{2}$, the E_x field must be located at n so that its centered difference is equal about $n + \frac{1}{2}$. The full discretized equation becomes

$$\frac{1}{\Delta z} \left[H_y^{n+\frac{1}{2}}(i + \frac{1}{2}) - H_y^{n+\frac{1}{2}}(i - \frac{1}{2}) \right] = \frac{\varepsilon_r(i) \varepsilon_o}{\Delta t} [E_x^{n+1}(i) - E_x^n(i)],$$

which can be re-arranged to solve for $E_x^{n+1}(i)$ as a function of past values. The same can be done using Faraday's law to re-arrange for $H_y^{n+\frac{1}{2}}(i + \frac{1}{2})$. The notation of using half steps such as $i + \frac{1}{2}$ is referred to as a "staggered grid" and is accredited to Yee [60]. The final update equations are

$$E_x^{n+1}(i) = E^n(i) + \frac{\Delta t}{\varepsilon_o \varepsilon_r^{n+\frac{1}{2}}(i) \Delta z} \left[H_y^{n+\frac{1}{2}}(i + \frac{1}{2}) - H_y^{n+\frac{1}{2}}(i - \frac{1}{2}) \right] \quad (3.1)$$

and

$$H_y^{n+\frac{1}{2}}(i + \frac{1}{2}) = H^{n-\frac{1}{2}}(i + \frac{1}{2}) - \frac{\Delta t}{\mu_o \mu_r^n(i + \frac{1}{2}) \Delta z} [E_x^n(i + 1) - E_x^n(i)], \quad (3.2)$$

where it has been intentionally emphasized that the material parameters of relative permittivity $\varepsilon_r^{n+\frac{1}{2}}(i)$ and permeability $\mu_r^n(i + \frac{1}{2})$ are also staggered in time and space. This is usually inconsequential as permittivity and permeability rarely vary in time and their stag-

gered spatial locations cause negligible errors. If they did vary in time, or a problem with very high spatial variation was considered, more complicated methods than FDTD may have to be employed, such as the Method of Moments, or adaptive mesh refinement (AMR) [61, 62]. For stability, equations 3.1.1 and 3.1.1 require that the spatial and temporal step sizes be related by

$$\Delta t \leq \Delta z / (2c),$$

where c is the speed of light. If Δt were larger than this value, then the algorithm could not capture wave propagation over Δz . The finite difference scheme would then be unable to approximate a solution to a wave equation.

3.1.2 One-Dimensional Force Discretization and Field Averaging

This section will introduce how to calculate \vec{S} , W , \bar{T} , and \vec{f} using a one-dimensional (1D) example. If we consider plane wave propagation along the \hat{x} axis, the only components of the magnetic and electric fields are H_y and E_x . We can place them numerically at $E_x^n(i)$ and $H_y^{n+\frac{1}{2}}(i + \frac{1}{2})$, where i is the spatial index, and n is the temporal index. There is no standard for placement of \vec{S} , W , \bar{T} , and \vec{f} numerically on the staggered Yee grid in terms of i and n . However, there is advantageous placement for reduced numerical error and fast computation. Averaging numerical quantities is quite common in other finite difference solvers such as in fluid dynamics and heat transfer [63]. The force f_z , via equation 2.7 is

$$\frac{\partial}{\partial t} G_z + \frac{\partial}{\partial z} T_{zz} = -f_z.$$

We can then start our derivation with placing force numerically at $f_z^n(i)$ ¹, express the other terms as central differences, and re-arrange for $f_z^n(i)$ as

$$f_z^n(i) = -\frac{1}{\Delta z} \left[T_{zz}^n(i + \frac{1}{2}) - T_{zz}^n(i - \frac{1}{2}) \right] - \Delta t [G_z^{n+\frac{1}{2}}(i) - G_z^{n-\frac{1}{2}}(i)]. \quad (3.3)$$

Where the act of placing \vec{f} at the index location of i and n in equation 3.3 required the stress tensor to be located at $T_{zz}^n(i + \frac{1}{2})$, and the momentum density at $G_z^{n+\frac{1}{2}}(i)$. As an example, for the Abraham form these quantities are explicitly given by

$$T_{zz}^n(i + \frac{1}{2}) = D_x(i)^n E_x(i)^n B_y(i)^n H_y(i)^n$$

and,

$$G_z^{n+\frac{1}{2}}(i) = E_x^{n+\frac{1}{2}}(i) H_y^{n+\frac{1}{2}}(i).$$

Note the fields are not defined at $B_y(i)^n$ or $H_y(i)^n$ in the normal magnetic field update equation 3.1.1. They can be solved by averaging from known quantities. For example, $B_y(i)^n$ can be approximated as

$$B_y(i)^n = \frac{1}{4} \left[B_y(i + \frac{1}{2})^{n+\frac{1}{2}} + B_y(i + \frac{1}{2})^{n-\frac{1}{2}} + B_y(i - \frac{1}{2})^{n+\frac{1}{2}} + B_y(i - \frac{1}{2})^{n-\frac{1}{2}} \right] \quad (3.4)$$

and $E_x^{n+\frac{1}{2}}(i)$ as

¹We could also solve for the mechanical momentum, \vec{g} directly through $\frac{\partial}{\partial t} g = f$, or numerically as $[\vec{g}^{n+\frac{1}{2}}(i) - \vec{g}^{n-\frac{1}{2}}]/\Delta t = \vec{f}_z^n(i)$.

$$E_x^{n+\frac{1}{2}}(i) = \frac{1}{2} [E_x^{n+1}(i) + E_x^{n-1}(i)]. \quad (3.5)$$

The discretization for W would be

$$W^n(i) = W^{n-1}(i) - \frac{\Delta t}{\Delta z} \left[S_z^{n+\frac{1}{2}}(i + \frac{1}{2}) - S_z^{n+\frac{1}{2}}(i - \frac{1}{2}) \right], \quad (3.6)$$

which requires additional field averages. For example, $S_z^{n+\frac{1}{2}}(i + \frac{1}{2})$ is given by

$$S_z^{n+\frac{1}{2}}(i + \frac{1}{2}) = E_x^{n+\frac{1}{2}}(i + \frac{1}{2}) H_y^{n+\frac{1}{2}}(i + \frac{1}{2})$$

where $E_x^{n+\frac{1}{2}}(i + \frac{1}{2})$ is a field quantity that does not exist in the normal FDTD Yee algorithm.

It can be approximated by field averaging as

$$E_x^{n+\frac{1}{2}}(i + \frac{1}{2}) = \frac{1}{4} [E_x(i+1)^{n+1} + E_x(i+1)^{n-1} + E_x(i-1)^{n+1} + E_x(i-1)^{n-1}]$$

It would be desired to reduce the number of times averaging has to be done, however the staggered mesh algorithm of FDTD makes field averaging unavoidable.

The benefits of field averaging is demonstrated in Figure 3.2 where an energy density calculation from an FDTD simulation is used as an example. In the figure a pulse enters the simulation space and then passes through an impedance-matched slab. The slab is lossless so a correct solution should show no energy density left behind. The figure shows that using FDTD to track the energy density of a pulse without field averaging can cause significant error, in the case shown, up to 2.5 %. When field averaging is used, the error is negligible at the same step size.

3.1.3 Two-Dimensional Force Discretization

We can expand our previous discussion on force discretization in one dimension to discuss problems that require two dimensional (2D) analysis. To do this, we will consider how to numerically solve for the Minkowski force density using the corresponding stress tensor, \bar{T}_{MN} and momentum density, $\vec{D} \times \vec{B}$. We will consider the 2D staggered Yee grid shown below in Figure 3.3 where only E_x , E_y , and H_z field components are present. This corresponds to “transverse-magnetic” (TM) propagation.

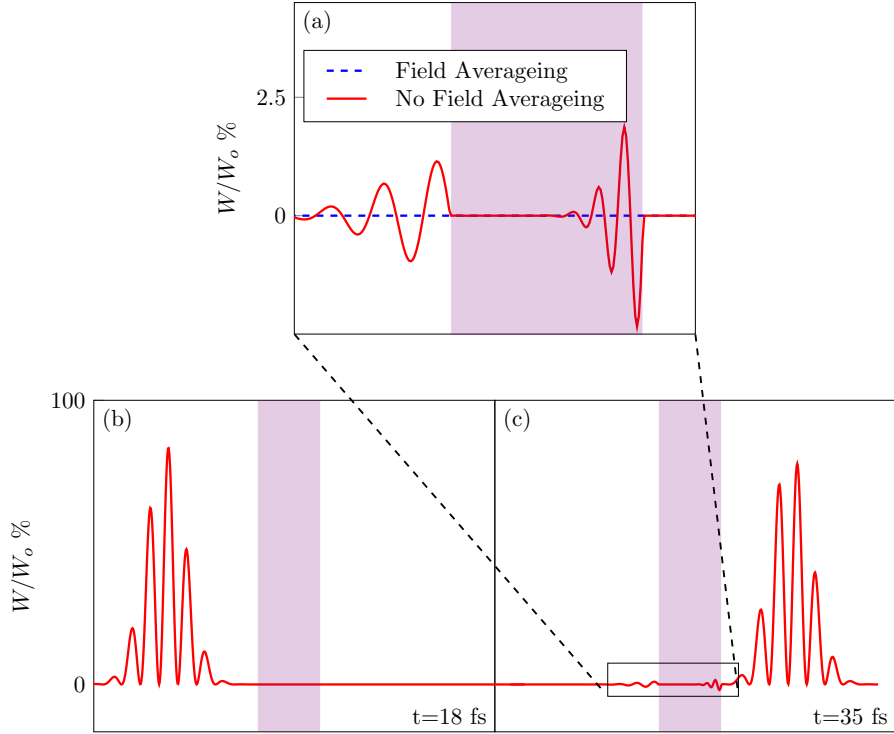


Figure 3.2: The numerical error produced when field averaging is not implemented. A pulse is directed at an impedance-matched slab from free space with refractive index $n = 2$. (a) A DC error value of energy density is at both the entrance and exit faces of the slab after the pulse propagates through. In (b) this error becomes negligible when field averaging is implemented. (c) The pulse as it exits the slab with no field averaging, the error is comparable in value to the field energy itself when no field averaging is done.

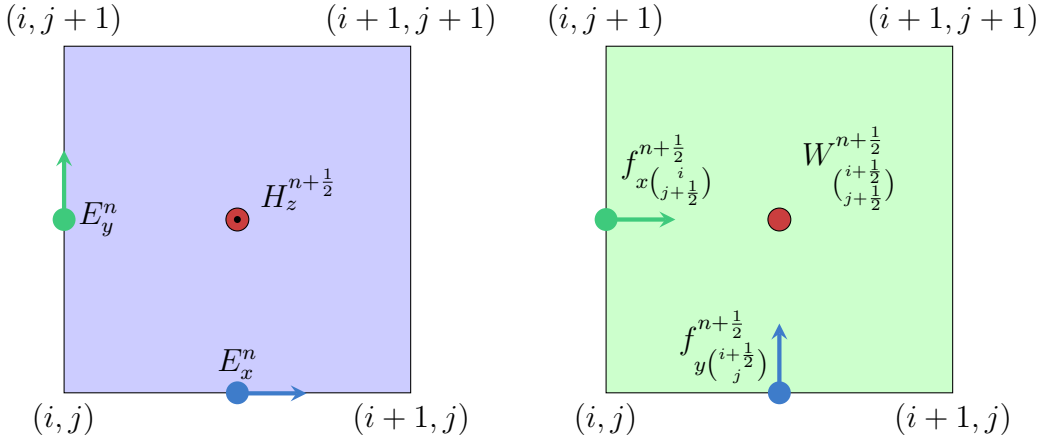


Figure 3.3: Figure showing the discretized locations of the electromagnetic field and force values on the Yee grid. The placement of f_x and f_y are such to reduce the number of field averages that need to be taken, this reduces the numerical error.

The total momentum \vec{G} in continuity equation 2.7 can be parsed into electromagnetic and mechanical contributions where $\vec{G} = \vec{G}_{MN} + \vec{G}_{mech}$. The force density is then calculated as

$$\nabla \cdot \bar{T}_{MN} + \frac{\partial}{\partial t} \vec{G}_{MN} = -\frac{\partial}{\partial t} \vec{G}_{mch} = -\vec{f}_{MN}, \quad (3.7)$$

where the Minkowski stress tensor is $\bar{T}_{MN} = \frac{1}{2}(\vec{D} \cdot \vec{E} + \vec{B} \cdot \vec{H})\bar{I} - \vec{D}\vec{E} - \vec{B}\vec{H}$, and the resulting Minkowski force density is denoted as \vec{f}_{MN} . We now need to make a choice of where to place each term on the Yee grid. The example presented here will only consider the \hat{x} -component of force. The \hat{x} component of the momentum density term $\frac{\partial}{\partial t} \vec{G}_x$ will be placed spatially at $(j+\frac{1}{2})$ and temporally at $(n + \frac{1}{2})$ to give

$$\frac{\partial}{\partial t} G_{x(j+\frac{1}{2})}^{n+\frac{1}{2}} = \frac{1}{\Delta t} \left[(D_y H_z)_{(j+\frac{1}{2})}^{n+1} - (D_y H_z)_{(j+\frac{1}{2})}^n \right].$$

We can see from the Yee grid in Figure 3.3 that D_y is already located correctly, but H_z is not spatially or temporally at the right location, to remedy this we can approximate $H_z^n_{(j+\frac{1}{2})}$ from the field average

$$H_z^n_{(j+\frac{1}{2})} = \frac{1}{4} \left[H_{z(i+\frac{1}{2})}^{n+\frac{1}{2}} + H_{z(i+\frac{1}{2})}^{n-\frac{1}{2}} + H_{z(i-\frac{1}{2})}^{n+\frac{1}{2}} + H_{z(i-\frac{1}{2})}^{n-\frac{1}{2}} \right]. \quad (3.8)$$

By using averaging such as in equation 3.8 we can use much larger step sizes before numerical error becomes apparent. To calculate the x component for force, the discretized form of equation 3.7 can now be expressed as

$$T_{x(j+\frac{1}{2})}^{n+\frac{1}{2}} + \frac{\partial}{\partial t} G_{x(j+\frac{1}{2})}^{n+\frac{1}{2}} = -f_{x(j+\frac{1}{2})}^{n+\frac{1}{2}}. \quad (3.9)$$

Which requires another field average to solve for $T_{x(j+\frac{1}{2})}^{n+\frac{1}{2}}$. Using the placement in equation 3.1.3 we can express this placement as

$$T_{x(j+\frac{1}{2})}^{n+\frac{1}{2}} = \frac{1}{2} \left[T_{x(j+\frac{1}{2})}^{n+1} + T_{x(j+\frac{1}{2})}^n \right].$$

The full expression for $T_{x(j+\frac{1}{2})}^{n+\frac{1}{2}}$ needs to be solved by numerically expanding

$$(\nabla \cdot \bar{T}_{MN}) \cdot \hat{x} = [\frac{\partial}{\partial x} T_{xx} + \frac{\partial}{\partial y} T_{xy} + \frac{\partial}{\partial z} T_{xz}] \hat{x}.$$

For our TM example, these tensor components simplify to

$$T_{xx} = \frac{1}{2} [D_x E_x + D_y E_y + B_z H_z] - D_x E_x,$$

$$T_{xy} = -D_x E_y,$$

and

$$T_{xz} = 0.$$

These expressions can be expressed as four different unique terms for discretization that we can denote here by t_1, t_2, t_3 , and t_4 within the expression

$$T_{x(j+\frac{1}{2})}^n = \frac{1}{2} \left[-t_{1(j+\frac{1}{2})}^n + t_{2(j+\frac{1}{2})}^n + t_{3(j+\frac{1}{2})}^n \right] - t_{4(j+\frac{1}{2})}^n. \quad (3.10)$$

The terms in equation 3.10 expand to

$$\begin{aligned} t_{1(j+\frac{1}{2})}^n &= \frac{1}{\Delta x} \left[(D_x E_x)_{(j+\frac{1}{2})}^n - (D_x E_x)_{(j-\frac{1}{2})}^n \right], \\ t_{2(j+\frac{1}{2})}^n &= \frac{1}{2\Delta x} \left[(D_y E_y)_{(j+\frac{1}{2})}^n - (D_y E_y)_{(j-\frac{1}{2})}^n \right], \\ t_{3(j+\frac{1}{2})}^n &= \frac{1}{\Delta x} \left[(B_z H_z)_{(j+\frac{1}{2})}^n - (B_z H_z)_{(j-\frac{1}{2})}^n \right], \end{aligned}$$

and

$$t_{4(j+\frac{1}{2})}^n = \frac{1}{\Delta y} \left[(D_x E_y)_{(j+1)}^n - (D_x E_y)_{(j)}^n \right].$$

The field averages required for t_1 are

$$D_x^n_{(j+\frac{1}{2})} = \frac{1}{2} \left[D_x^n_{(j+\frac{1}{2})} + D_x^n_{(j-\frac{1}{2})} \right]$$

and

$$D_x^n_{(j-\frac{1}{2})} = \frac{1}{2} \left[D_x^n_{(j-\frac{1}{2})} + D_x^n_{(j+\frac{1}{2})} \right].$$

For t_3 they are

$$D_x^n_{(j)} = \frac{1}{2} \left[D_x^n_{(j+\frac{1}{2})} + D_x^n_{(j-\frac{1}{2})} \right]$$

and

$$D_x^n_{(j+1)} = \frac{1}{2} \left[D_x^n_{(j+\frac{1}{2})} + D_x^n_{(j-\frac{1}{2})} \right].$$

For t_4 they are

$$E_y^n_{(j)} = \frac{1}{2} \left[E_y^n_{(j-\frac{1}{2})} + E_y^n_{(j+\frac{1}{2})} \right]$$

and

$$E_y^n_{(j+1)} = \frac{1}{2} \left[E_y^n_{(j+\frac{3}{2})} + E_y^n_{(j+\frac{1}{2})} \right].$$

The t_2 term does not require any averaging as the E_y and D_y components already exist at the $(i \pm 1, j \pm \frac{1}{2})$ locations on the Yee mesh. This averaging process can be repeated for each of the different momentum density forms and stress tensors listed in Table 1.1 . The FDTD method provides a direct way to solve for electrodynamic quantities, but care must be taken in regards to field placement and field averaging.

3.2 Finite-Difference Methods in Fluid Dynamics

For the fluid studies in this thesis, we implement a CFD method based on the marker and cell (MAC) front tracking technique, as outlined by Tryggvason [64]. A complete step-by-step guide meant for students can be found in [63]. The equation to be solved is the incompressible Navier-Stokes equation

$$\rho \frac{\partial u}{\partial t_f} = \rho \nabla \cdot uu - \nabla P + q_o \nabla^2 u + \rho g + f_o + \langle f_e \rangle, \quad (3.11)$$

where $q_o \nabla^2 u$ is the diffusion term with viscosity q_o , $\rho \nabla \cdot uu$ the advection term, ∇P is the pressure gradient, ρg is the effect of gravity, f_o are body forces including surface tension, and $\langle f_e \rangle$ is the time-averaged electromagnetic force. The electromagnetic force is time averaged because the time scales for fluid deformation is much larger than the electromagnetic timescales considered in this thesis. Interaction between electromagnetic fields and deformable fluids is described in a feedback loop cyclically modeling each on its relevant time scales under quasi-static conditions. The time-averaged electromagnetic force density is calculated using the FDTD method and acts as a body force within the MAC method, which then determines the deformation of the fluid under the combined influence of gravity, radiation pressure, surface tension, and viscous forces. Once the front interface separating the two fluids has displaced one coarse grid spacing Δ , the fluid boundaries are updated on the Yee grid, and the time-averaged electromagnetic force density (averaged over at least 30 cycles) is re-computed. In this way, the FDTD and MAC solvers progress in turn, feeding each other updated distributions of the force density and fluid-interface location at the end of their turns. The result is a series of detailed snapshots of fluid deformation under varying radiation pressure and material distribution. The algorithm for this continuous operation is shown in Figure 3.4. The initial conditions for the fluid velocity at all locations is zero.

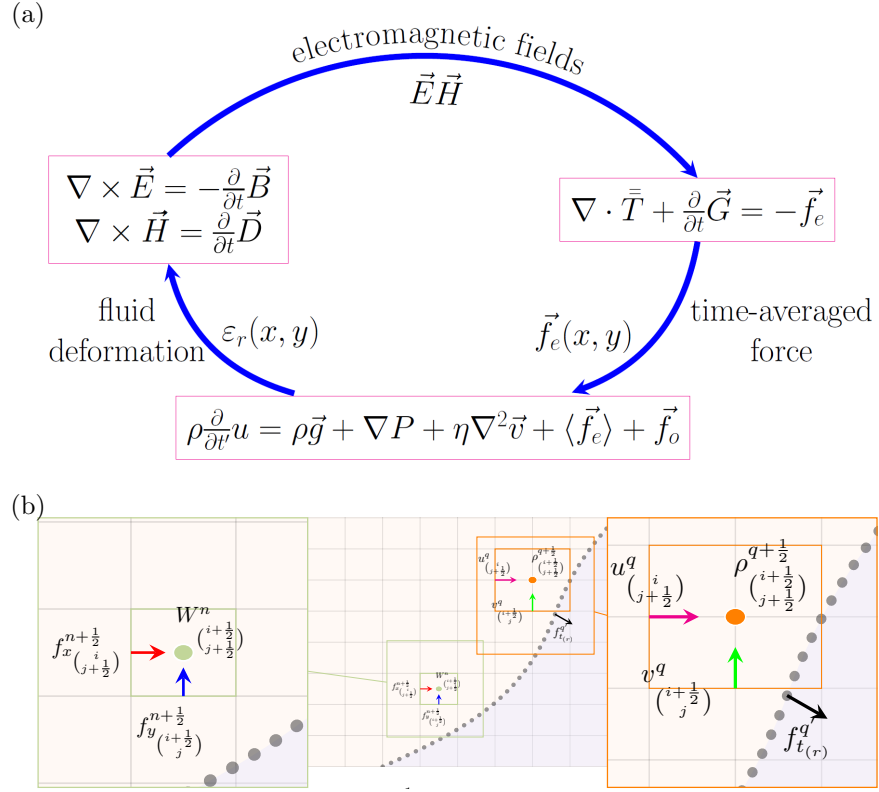


Figure 3.4: (a) The general algorithm to solve for fluid deformation under radiation pressure. The density, ρ , and the material parameters of permittivity and permeability are initialized together, with the electromagnetic grid having a finer grid resolution than the fluid grid. The electromagnetic fields are then solved and the resulting force density \vec{f}_e is time-averaged before inserted into the Navier-Stokes algorithm. (b) staggered grid locations for the electromagnetic values of f_x , f_y , and energy density W along with staggered grid location for the fluid dynamic values of the velocity components u , v , and density ρ . Also shown are the force contributions from the fluid surface tension f_t , which exists on a front with sub-cell resolution relative to both staggered grids.

Chapter 4: Results

4.1 The Balazs Thought Experiment

The Balazs thought experiment was a theoretical argument made in 1953 that compared the Abraham and Minkowski momentum densities on the premise of center-of-mass velocity conservation [29]. In his experiment, Balazs compares two hypothetical closed systems. Both systems contain a transparent impedance matched slab of length L with mass M and a pulse of mass $m \ll M$. In the first system the pulse flies over the slab and no interaction occurs, the total system momentum is mc and the system's center-of-mass velocity is $mc/(m + M)$. In the second system the pulse collides with the slab and slows down to a speed of c/n . During this interaction, the total momentum of each system must be equal to mc as there are no external sources of work to differentiate them [29] the pulse within the interacting system will have lagged behind the first system's pulse. Figure 4.1 depicts both systems of the Balazs thought experiment with lag d .

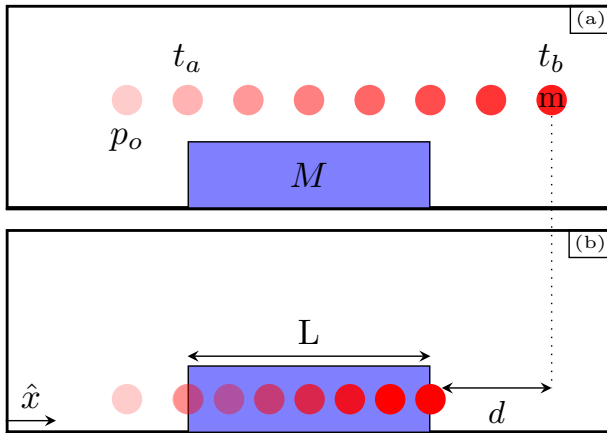


Figure 4.1: Illustration of the Balazs thought experiment. (a) In the first system a pulse of mass m does not interact with the slab, meaning global momentum is mc and global center of mass velocity is $mc/(M + m)$. (b) In the second system where the pulse enters the slab and slows down to c/n .

We will now re-produce the derivation of this thought experiment similar to the authors in [65, 66, 67] and show the expanded steps used by Barnett [66]. We take the electro-magnetic energy of a pulse to be that of a photon $\hbar\omega$, and its mass given by $m = \hbar\omega/c^2$. With the slab initially stationary, the global conserved momentum of the system at t_a is equal to only the photon momentum $mc = \hbar\omega/c$. Taking the time interval in Figure 4.1 as $\Delta t = t_b - t_a$, the difference in the photon's center of mass location between system 1 and 2 is

$$\left(\frac{\hbar\omega}{c}\Delta t\right) - \left(\frac{\hbar\omega}{cn}\Delta t\right) = \frac{\hbar\omega}{c}\Delta t \left(1 - \frac{1}{n}\right),$$

where the time interval can be expressed as $\Delta t = \frac{nL}{c}$ to give

$$\frac{\hbar\omega}{c^2} L (n - 1). \quad (4.1)$$

For uniform center-of-mass conservation between the two systems, the slab contribution to center-of-mass within the interacting system in Figure 4.1 (b) must be equal to equation 4.1. Equating the product of $M\Delta x_s$ to equation 4.1 yields a slab displacement of

$$\Delta x_s = \frac{\hbar\omega}{Mc^2} L (n - 1). \quad (4.2)$$

This displacement can be used in the equation for momentum conservation in the second system and leads to an expression for the photon momentum within the slab. Momentum conservation for the second system can be expressed as

$$\frac{\hbar\omega}{c} = M \frac{\Delta x_s}{\Delta t} + p_{em}, \quad (4.3)$$

where equation 4.2 represents Δx_s which can be combined with $\Delta t = \frac{Ln}{c}$ to give

$$p_{em} = \frac{\hbar\omega}{cn}, \quad (4.4)$$

with equation 4.4 corresponding to the Abraham momentum density. For the remainder of this thesis we will consider center-of-mass and momentum calculations in a field based description where the electrodynamic interactions are solved over continuous time intervals. This will provide useful insight beyond considering a particle picture and comparing events only in terms of before and after an interaction. For example we will be able to discuss how the Minkowski form could still be considered valid in terms of center-of-mass despite the derivation just shown.

4.1.1 Momentum and Center-of-Mass Calculations

As opposed to the assumption of a fixed pulse mass m , we can combine equations 2.6 and 2.4 to express an electromagnetic mass density in terms of any postulated \vec{G} . We will consider a case where there is no external work ($U_w = 0$), giving an energy continuity equation of

$$\nabla \cdot \vec{S} + \frac{\partial}{\partial t} W = 0,$$

where expressing the electromagnetic mass as $m = W/c^2$, and substituting $\vec{S} = \vec{G}c^2$ gives

$$m(t) = \int_0^t -(\nabla \cdot \vec{G}) dt, \quad (4.5)$$

where \vec{G} can be any form of momentum density. The Minkowski momentum density, $\vec{D} \times \vec{B}$, is made of discontinuous fields, which means that implementing the Minkowski momentum density yields a surface energy current that can be solved for by taking the volume integral of equation 1.1 at the interface between two different media. This is analogous to the current density that results when deriving the boundary conditions for the electric displacement field \vec{D} [68]. We can demonstrate this with a simple 1D-plane-wave example, as in Figure 4.2, where the interface between free space and a lossless impedance-matched medium ($\epsilon_r = \mu_r$) is considered.

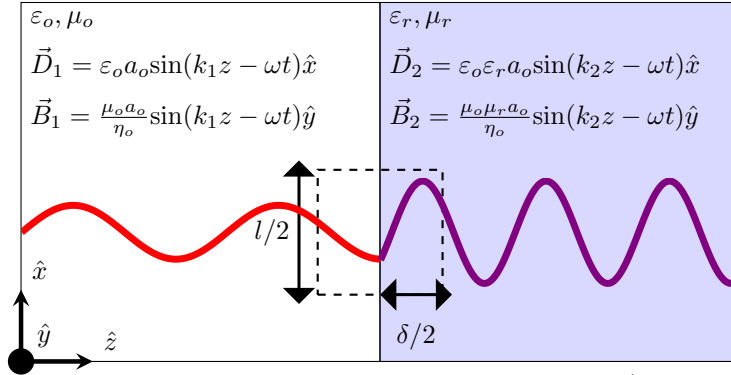


Figure 4.2: A plane wave at the interface between free space and an impedance-matched medium ($\mu_r = \epsilon_r$). The plane wave is shown in terms of \vec{D} and \vec{B} fields to illustrate the discontinuous nature of the Minkowski momentum density. The free space wavevector is described by k_1 and propagation within the impedance-matched medium is described by k_2 .

When implementing the energy continuity equation 2.6 at the boundary in Figure 4.2 with $\delta \rightarrow 0$, a surface energy current $K_w(t)$ can be defined as

$$\vec{K}_w(t) = \int_0^t (\vec{S}_1 - \vec{S}_2) dt, \quad (4.6)$$

where \vec{S}_1 is the power flux density in free space and \vec{S}_2 represents the power flux density inside the medium. This expression can be non-zero as the fields associated with the Minkowski power density can be discontinuous, as shown in Figure 4.2. The magnitude of the surface energy density [J/m^2] associated with the case in Figure 4.2 is

$$K_w(t) = \frac{a_o^2}{2\eta_o} \left[(1 - \varepsilon_r \mu_r)t + (\varepsilon_r \mu_r - 1) \left(\frac{\sin^2(2\omega t)}{2\omega} \right) \right]. \quad (4.7)$$

For a case more analogous to the pulse in the Balazs thought experiment, Figure 4.3 illustrates the electromagnetic energy density distribution as a pulse interacts with an impedance matched lossless slab of index ($n = 2$). Values are calculated using the FDTD method in Section . For the symmetric Minkowski form in Figure 4.3, illumination of the slab causes an energy extraction at the entrance face and s deposition of energy at the exit face.

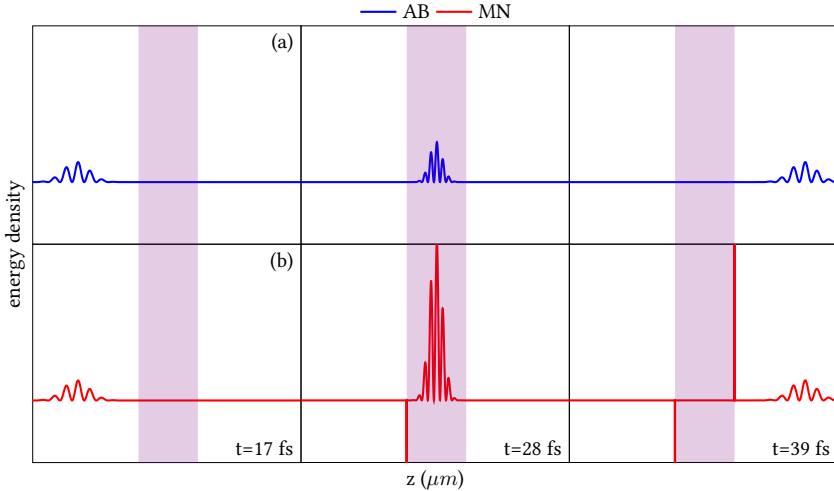


Figure 4.3: Energy density distributions at three moments in time predicted by the Abraham (a) and the Minkowski (b) postulates, for the case of a pulse normally incident onto a slab under conditions identical to those in Figure 4.4. The discontinuous nature of the Minkowski energy density predicts surface energy spikes analogous to those calculated in Figure 4.2.

For the same slab as in Figure 4.3, Figure 4.4 compares momentum and center-of-mass calculations for the Abraham and Minkowski postulates. As shown in the snap-shots of the electric field, the pulse is created at the left end of the enclosure and propagates to the right towards the slab. During this interaction, global momentum and center-of-mass velocity are conserved (i.e., both remain fixed at zero). After the pulse enters the slab, its reduction in forward momentum is compensated by the speeding up of the slab and the increase in slab momentum. However, if we replace the Abraham momentum density with the Minkowski momentum density while leaving everything else unchanged, center-of-mass conservation is lost (dashed line in Figure 4.4 (d)). Upon pulse entry, the increase in the forward pulse momentum is balanced out by the backward slab momentum, which causes the system center-of-mass velocity to stray from zero. Violation of this conservation principle has been one of the primary arguments against the validity of the Minkowski momentum density [29, 27, 37]. Using the symmetric form of the Minkowski power flux (solid line) allows the pulse mass to change in spatial density upon entering the slab and conserve the global center-of-mass velocity. This pulse mass affects the slab mass, as energy continuity implies that any changes in the pulse mass must be balanced by local changes in the slab mass.

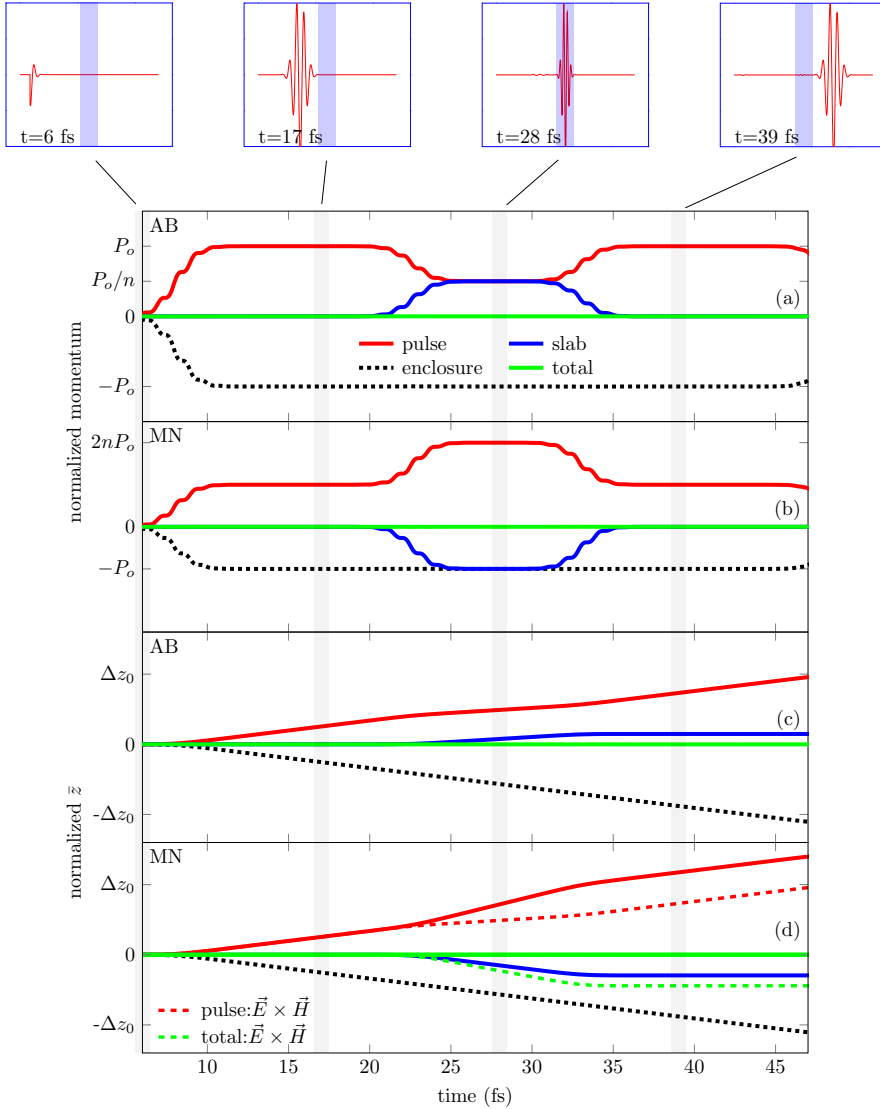


Figure 4.4: Pulse momentum exchange with an impedance-matched medium. The results are normalized to the initial free space momentum of P_o , and slab index n . (a) The Abraham model predicts a pulse momentum decrease proportional to $1/n$ when immersed in the slab, whereas the Minkowski model (b) predicts a pulse momentum increase proportional to n . (c) Conservation of center-of-mass velocity for the Abraham form. (d) Conservation of center-of-mass velocity for the Minkowski form. The Balazs implementation for the pulse and total center-of-mass displacement is shown with a dotted line, using the Abraham power flux density of $\vec{E} \times \vec{H}$, the Minkowski form does not conserve center-of-mass velocity. The solid line in (d) illustrates that when paired with its symmetrical form of power flux density, $c^2 \vec{D} \times \vec{B}$, the Minkowski form can conserve center-of-mass velocity.

4.1.2 An Experimental Variant on the Balazs Thought Experiment

Hypothesizing the existence of a surface energy such as in equation 4.6, we can consider what would happen if this energy density were real and able to thermalize. To model this, we can relate equation 4.6 to a volume generation term in the one-dimensional heat diffusion equation,

$$\frac{\partial^2 T}{\partial z^2} + \frac{\dot{q}(z, t)}{k} = \frac{1}{\alpha} \frac{\partial T}{\partial t}, \quad (4.8)$$

where $\dot{q}(z, t)$ is the internal energy generation, k is the thermal conductivity, and α is thermal diffusivity.

We propose the following experiment to distinguish the Abraham and Minkowski forms of momentum density. At microwave frequencies, a coaxial guided wave structure propagating a dominant TEM mode can easily be constructed [69]. Within the coaxial structure, a dielectric material is inserted in a section of the guide to create a boundary condition where power flows through a uniform medium. This concept is illustrated in Figure 4.6. Since the characteristic impedance of the transmission line is determined by the conductor radii, a and b , and the dielectric constant of the medium, the inner radius can be stepped down to maintain a constant characteristic impedance throughout the length of the transmission line [69, ch. 5]. If all sections of the transmission line are matched, then no reflections at the dielectric boundaries are created and a TEM wave should propagate without appreciable loss. The thermal properties for the Teflon used in this experiment are considered at their room temperature values. Teflon thermal conductivity k is 0.25 W/(m · K), and α is 0.124 mm²/s [70]. According to Figure 4.3, a cooling effect may be expected at the entrance and a heating effect would exist at the exit. If a portion of the surface energy for the Minkowski form is assumed to thermalize, a lower bound on the amount of energy converted from electromagnetic to thermal should be proportional to the loss tangent of the material. We set the total surface generation density to be equal to $\delta \cdot K_w(t)$ calculated numerically using equation 4.6 where δ is the loss tangent of Teflon, reported by [71] to be 1.2×10^{-6} at 13.56 MHz. This low loss tangent preferentially creates a situation where no observed heating would indicate an Abraham form, but an observation of appreciable heating suggests the Minkowski form.

A picture of the coaxial structure is shown in Figure 4.6, and consists of a Teflon dielectric in the mid section sandwiched between two air dielectric regions. The coaxial line is designed to have a characteristic impedance of 50Ω and measurements are made in a high-power test bed where the incident source power can be adjusted to several hundred watts. A frequency of 13.56 MHz was used with an off-the-shelf 1 kW power amplifier as a source to create large incident power fluxes. The coaxial line is terminated in a high-power 500 W load which is matched to 50Ω . Teflon has a dielectric constant of 2.1 at the operating frequency of 13.56 MHz; therefore, very low insertion loss is expected. Two small holes, labeled as spots 1 and 2 in Figure 4.5 are drilled into the outer conductor to create apertures where temperature can be imaged with an infrared camera. Figure 4.5 (b) shows a temperature difference of 0.4 K, which is much smaller than the predicted 2.0 K temperature difference from solving equation 4.8. Most importantly, Figure 4.3 predicts the exit face to be hotter than the entrance face relative to the propagation direction, a trait that holds for continuous wave illumination as well. This contradicts the observed temperature difference where Spot 2 in Figure 4.5 (a) is actually cooler than the entrance face of Spot 1. We conclude that the absence of measurable heating or cooling at the interfaces of the block more directly supports the Abraham momentum and Poynting vector without relying on whether the arguments of Laue are correct [49].

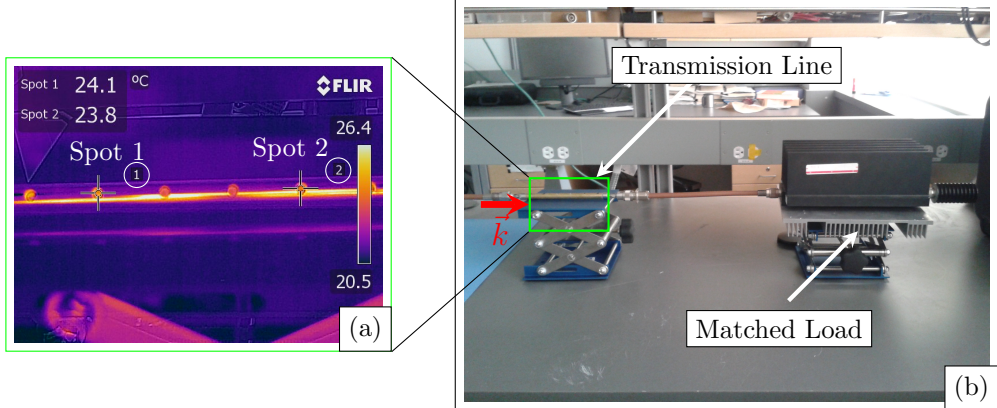


Figure 4.5: (a) Infrared image at 4 minutes showing the temperature at points (1) and (2) on either end of the Teflon segment.(b) The waveguide experimental setup where a 13.56 MHz source propagates a TEM wave in the \vec{k} direction along an impedance-matched waveguide that is terminated with a matched load.

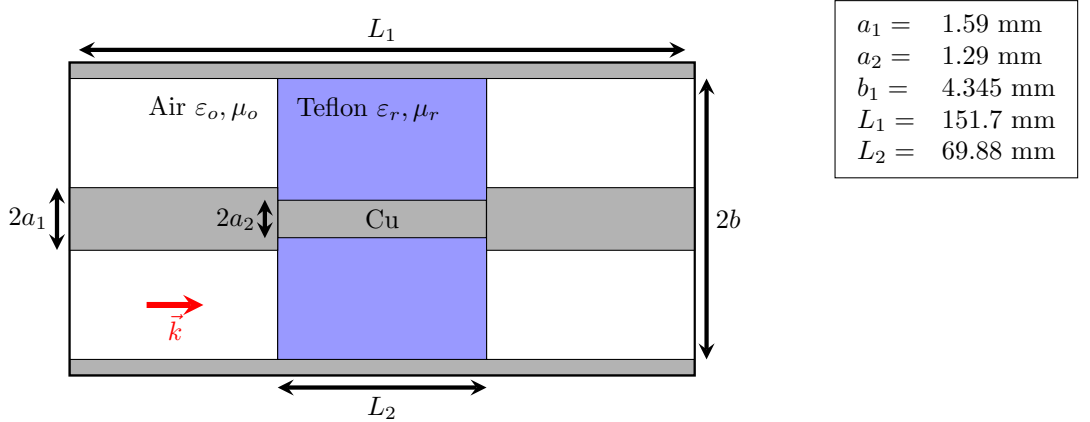


Figure 4.6: Salient dimensions for the impedance-matched waveguide labeled on the waveguide with their values tabulated. This configuration represents a close analogue to the impedance-matched medium of the Balazs thought experiment.

4.2 Discussion and Conclusions on the Balazs Thought Experiment

Is the surface energy density predicted by the Minkowski postulates real and physical? The possibility of similar discontinuities in energy density have been discussed at the surface of magnetizable media when invoking an Amperian definition of power flux $\vec{E} \times \vec{B}\mu_o$. It has been argued that these energy discontinuities are “hidden” and purely mathematical and not physically measurable [72]. Hidden energy in the Amperian definition of power flux has been rationalized because the fundamental building blocks of magnetization are current loops, which possess inherent energy necessary to sustain perpetual current motion. Similar hidden energy arguments have yet to be put forward to reconcile the Minkowski power flux, although these arguments would likely invoke hidden energy storage in both current loops and polarization charge.

We have presented here an alternative route to comparing the Abraham and Minkowski momentum forms using an experimental implementation of the Balazs thought experiment. We have examined their differences in predicted energy deposition at the interface of lossless dielectrics. The results of our experiments show that the symmetric form of the Minkowski tensor produces a surface energy term. In light of the fact that the Abraham form has shown no requirement for the existence of an anomalous surface energy current to conserve all variables, we agree with Balazs’ conclusion that the Abraham form is more likely to be correct.

4.3 Momentum and Center-of-Mass Conservation For All Five Forms

The Balazs thought experiment compared only the Minkowski and Abraham forms of momentum density; however, we can also use it to study the Amperian, Einstein-Laub, and Chu formulations. Shown below in Figure 4.7 is the momentum and center-of-mass conservation for all five electrodynamic theories for the more general case of a dispersive slab with loss. Here, the Einstein-Laub and Chu formulations are identical to the Abraham form, which is to be expected as the Einstein-Laub and Chu stress tensors in Table 1.1 are only different within their two-dimensional shearing terms. The Amperian form exhibits some unique properties. The Amperian form predicts a decrease in electromagnetic momentum compensated by an increase in slab momentum, having the same directional behavior as the Abraham form, but different in magnitude. The center-of-mass conservation for the Amperian form demonstrates (dotted line) that pairing the Amperian momentum density with the canonical Poynting vector $\vec{E} \times \vec{H}$ also causes a violation of center-of-mass velocity analogous to how the Minkowski form violates center-of-mass conservation shown in Figure 4.4. Therefore, also analogously when the power flux of the Amperian form is solved for by using equation 2.4, it does conserve center-of-mass velocity.

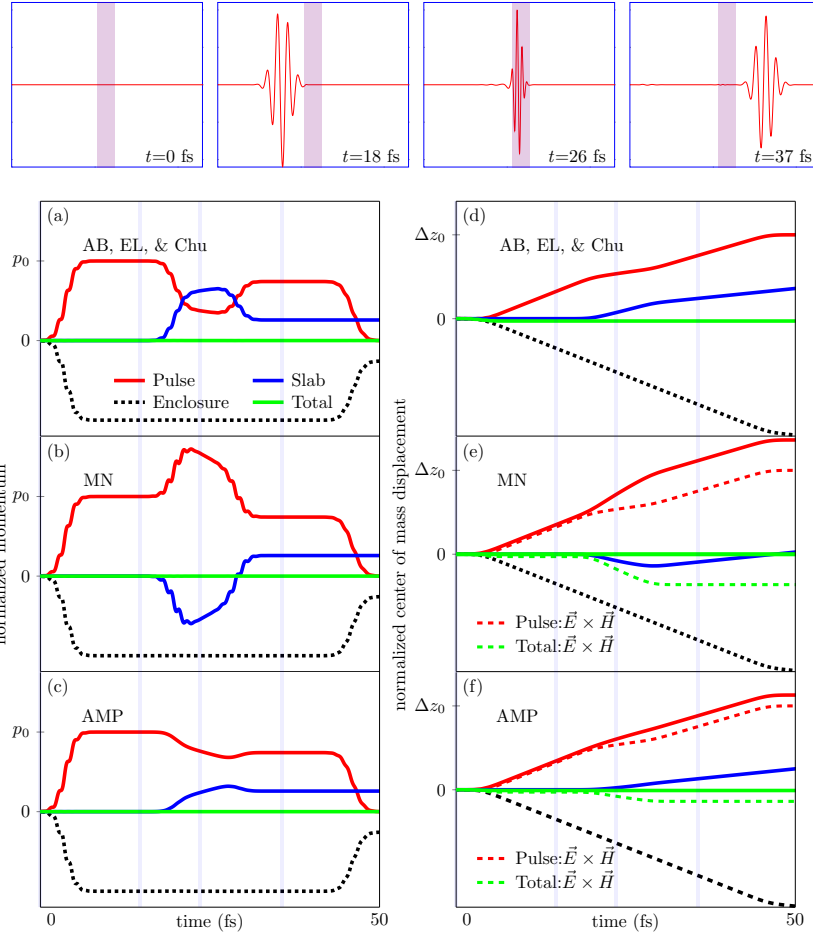


Figure 4.7: Simulations of the Minkowski, Abraham, Einstein-Laub, Amperian, and Chu postulates with conservation of momentum and center-of-mass velocity. Shown here is a general case of a lossy dispersive impedance-matched slab with refractive index $\bar{n} = 2.04 + i0.01$, using electric and magnetic drude parameters of $\gamma_e = \gamma_m = 2.5 \times 10^{14}$, $\omega_{pe} = \omega_{pm} = 1.2 \times 10^{15}$, and $\epsilon_\infty = \mu_\infty = 2.2$. The pulse is centered at a free-space wavelength $\lambda_0 = 632$ nm with a pulse width $\tau = 2$ fs. Both the pulse and slab are immersed in vacuum and contained in a rigid enclosure. (top row) Snapshots of the pulse electric field emitting from the left side of the enclosure, propagating through the slab, and disappearing on the right side of the enclosure. (a)-(c) Momentum contained in the pulse (red), slab (blue), and enclosure (black) as described by (a) the Abraham, Einstein-Laub, and Chu postulates, (b) the Minkowski postulates, and (c) the Amperian postulates. Momentum is normalized to the free-space momentum of the pulse, p_0 . The total momentum (green) is always conserved and fixed at zero. (d)-(f) Center-of-mass displacement of the pulse (red), slab (blue), and enclosure (black) as described by (d) the Abraham, Einstein-Laub, and Chu postulates, (e) the Minkowski postulates using either $\vec{E} \times \vec{H}$ (dashed) or $\vec{D} \times \vec{B}$ (solid) as the power flux, and (f) the Amperian postulates using either $\vec{E} \times \vec{H}$ (dashed) or $\epsilon_0 \vec{E} \times \vec{B}$ (solid) as the power flux. The center-of-mass displacement is normalized to the net slab displacement divided by its mass ratio. The system center-of-mass (solid-green) predicted by the Minkowski and Amperian postulates with the Poynting vector $\vec{E} \times \vec{H}$ (dashed green) strays from zero and thus, is inconsistent with center-of-mass velocity conservation.

The energy density for the momentum and center-of-mass calculations in Figure 4.7 is shown in Figure 4.8. As with the previous analysis in Figure 4.3, surface energy density exists for the discontinuous Minkowski and Amperian power flux forms. In addition, some energy is left behind in the bulk of the material for all forms proportional to the loss of the dispersive slab.

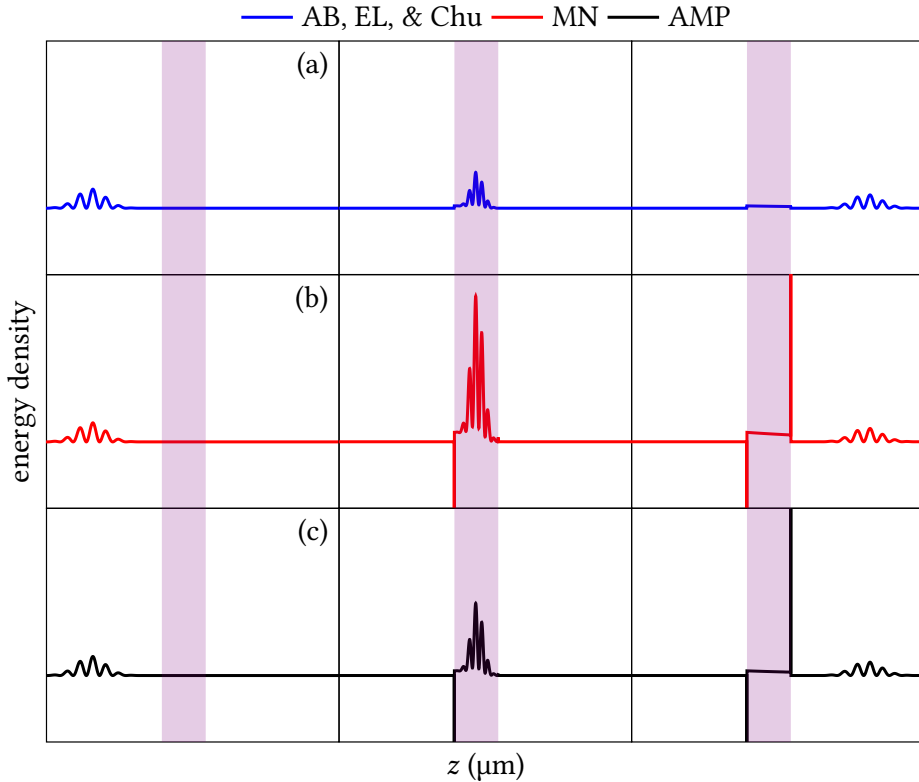


Figure 4.8: Instantaneous energy density distributions at three moments in time predicted by (a) the Abraham, Einstein-Laub, and Chu postulates, (b) the Minkowski postulates, and (c) the Amperian postulates, for the case of a pulse normally incident onto a slab under conditions identical to those in Figure 4.7.

4.4 Conservation in Two Dimensions

We next model the electrodynamic interaction between a pulse and a slab in two-dimensions. Extension of the analysis to more than one dimension is important, as it incorporates additional sources of electromagnetic momentum associated with electrostriction, magnetostriction, field gradients, and out-of-plane scattering (refraction) which are unavoidable in many experiments. As well, the shear terms previously mentioned for the stress tensor of the Einstein-Laub and Chu formulations become applicable. We use all five sets of electrodynamic postulates to study two configurations in which a finite-width pulse strikes a tilted planar slab at 45° immersed in vacuum: one in which the slab is made of positive-index glass and the other in which the slab is made of a hypothetical negative-index medium. As shown in Figure 4.9, global momentum and center-of-mass velocity are conserved using all five postulates regardless of whether the pulse undergoes a positive or negative refraction in the slab. This example shows that the methods used in this thesis for force density calculations are consistent with conservation laws in two dimensions. Direct numerical calculations offer an alternative to other approaches in multiple dimensions that separate force density terms in order to explicitly describe the effects of scattering and field gradients such as in [73].

As shown in Figure 4.9 and 4.10, the five postulates make different predictions of the slab recoil and therefore, can potentially be distinguished by experiments. For the case of a glass slab, the Minkowski postulates predict a momentary backward slab recoil, whereas all other postulates predict a forward slab recoil. This difference could be observed using short pulses in which recoil imbalances upon pulse entry and exit are separated in time. Measurements of pulse-induced recoil have yet to be performed, but according to these simulations could be a means to empirically validate a unique electrodynamic theory.

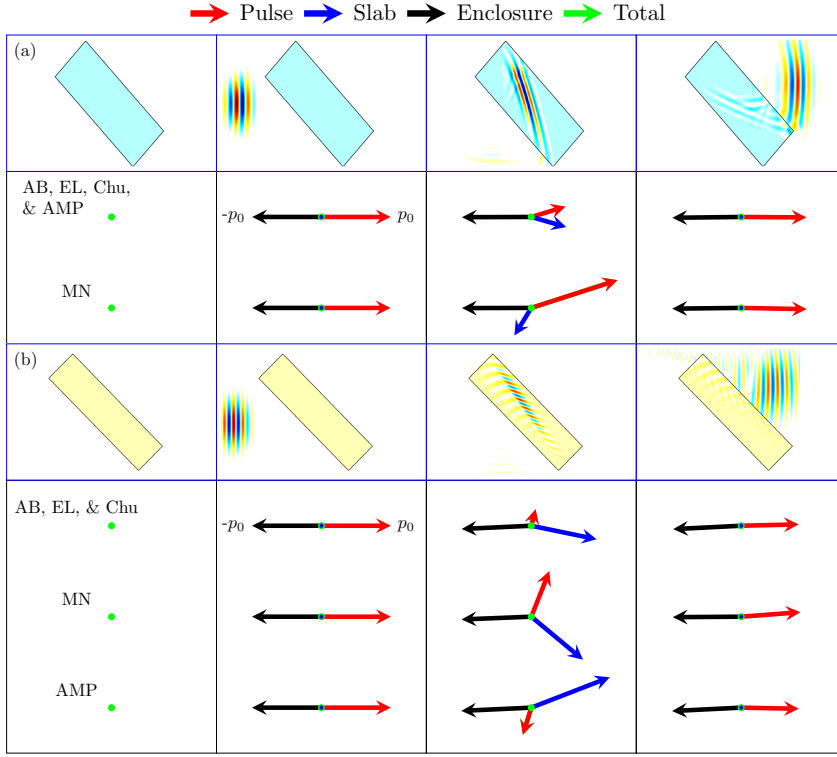


Figure 4.9: Two-dimensional field-based implementation of the Balazs thought experiment. Non-degenerate momentum predictions made by the Minkowski, Abraham, Einstein-Laub, Chu, and Amperian postulates for closed systems in which finite pulses are obliquely incident onto tilted impedance-matched slabs having (a) $n = \sqrt{3}$ (blue) and (b) $n = -1.3 + i0.07$ (yellow). The vector diagrams show instantaneous momentum of the pulse (red arrow), slab (blue arrow), enclosure (black arrow), and total system (green arrow) as the pulse propagates through the slabs. The total system momentum is conserved for all cases, as indicated by the stationary green dots. Slab thicknesses ($d = 5250$ nm for the positive-index slab and $d = 3500$ nm for the negative-index slab) have been chosen so that the incident pulse ($\lambda_o = 500$ nm, $\tau = 2$ fs) is fully immersed in the slab prior to exit. Dispersion of the negative-index slab is described by a Drude model for the permittivity and permeability with the following parameters: scattering rate $\Gamma = 2250$ THz, plasma frequency $\omega_p = 1200$ THz, static permittivity $\varepsilon_\infty = 1.4$, and static permeability $\mu_\infty = 1.4$.

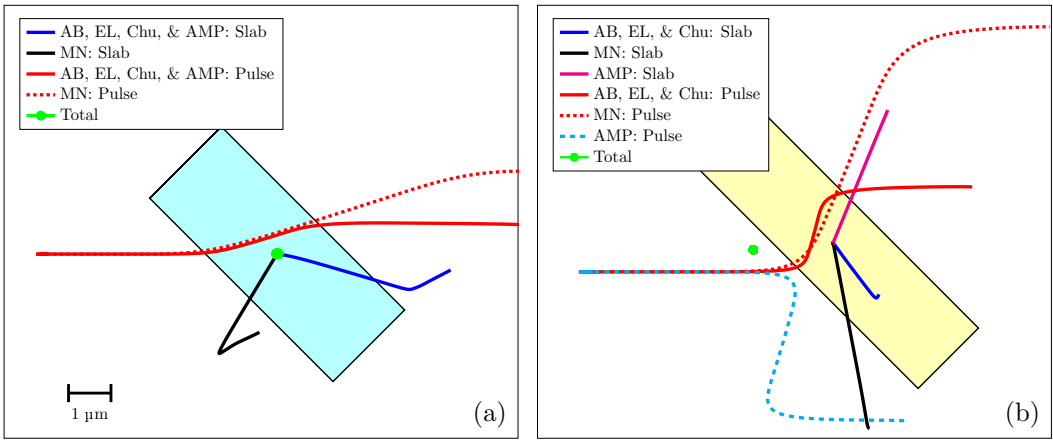


Figure 4.10: Non-degenerate center-of-mass displacement predictions made by the Minkowski (MN), Abraham (AB), Einstein-Laub (EL), Chu, and Amperian (AMP) postulates for closed systems in which finite pulses are obliquely incident onto tilted impedance-matched slabs having (a) $n = \sqrt{3}$ (blue) and (b) $\tilde{n} = -1.3 + i0.07$ (yellow). The configurations are identical to those in Figure 4.9. Note that the total center-of-mass displacement remains fixed, as indicated by the stationary green dots.

4.5 Radiation Pressure on Submerged Mirrors

Experiments to study radiation pressure in the early 1900s by Lebedev [3], Nichols and Hull [4, 5], and later by Bell and Green [74], proved that light impinging from a vacuum could transfer momentum to macroscopic objects. It was not until the mid-1900s that attempts were made to probe the momentum conferred by light impinging from dielectric media. In 1954, Jones and Richards [13] immersed a rhodium-coated silver mirror in various dispersive liquids ranging in refractive index from 1.33 to 1.63, and observed its displacement caused by tungsten lamp illumination. They concluded that light of a fixed intensity exerted a normalized pressure that is proportional to the refractive index of the liquids within an error margin of $\pm 1.2\%$. This experiment was later refined in 1978 by Jones and Leslie [14]. The lamp was replaced with a HeNe laser to increase light coherence, and the rhodium-coated silver mirror was replaced with a multi-layered dielectric mirror (of unknown composition) to mitigate heating and thermal expansion. Improved experimental precision yielded confirmation, within an error margin of $\pm 0.05\%$, of a linear dependence of normalized radiation pressure on the refractive index of the immersing fluids. Although the results of the Jones-Richards and Jones-Leslie experiments are directly explained by how light momentum of the Minkowski form scales with refractive index [25, 26, 27, 28], there has been growing evidence that the experiments could be modelled using different electrodynamic formulations [40, 42, 75, 76, 77, 78]. As early as 1978, Jones [40] proposed an Abraham model to explain momentum transfer to submerged mirrors based on mechanical perturbations in the fluid which add to the electromagnetic contribution of momentum to give a Minkowski-like total momentum. Field-based descriptions of the experiments have accurately predicted the dependence of radiation pressure on refractive index using the Einstein-Laub postulates [77], the Minkowski and Chu postulates [28, 78], and the Lorentz force density [75, 76]. These efforts, in turn, have been used as evidence to support the Abraham momentum density [77], the Minkowski momentum density [28, 78], or the arithmetic mean of the two [75, 76].

Different routes can be taken to arrive at identical predictions of radiation pressure. This is illustrated by considering pulse interaction with a reflective mirror assumed to be a perfect electric conductor, a common approximation of the mirrors used in the Jones-Richards and Jones-Leslie experiments [77, 42, 28]. The pulse, mirror, and surrounding dielectric medium are within an enclosure that is initially stationary such that 1) dynamic momentum must always achieve a zero sum and 2) the origins of the mirror momentum can be visualized in time. We assume that the surrounding medium and enclosure are connected. A pulse is created from the left end of the enclosure and bounces off the mirror

at normal incidence. As shown in Figure 4.11, the postulates predict dynamics that are all consistent with global momentum conservation and indistinguishable except for one. The Minkowski postulates, the lone outlier, describe the transfer of momentum upon reflection as a two-body process involving just the pulse and mirror. The pulse is created with momentum np_0 and the system recoils with equal and opposite momentum $-np_0$, where p_0 is the momentum of the pulse in vacuum. With the system momentum fixed at $-np_0$ over the remaining duration of the simulation, the pulse confers momentum $2np_0$ directly to the mirror upon reflection. The other postulates (Abraham, Einstein-Laub, Amperian, and Chu) describe the transfer of momentum as a three-body process involving the pulse, surrounding fluid, and the mirror. The pulse is created with momentum p_0/n and the system recoils with momentum $-p_0/n$. When the pulse is reflected from the mirror, two mechanisms transfer momentum to the mirror. The mirror receives a parcel of momentum $2p_0/n$ due to reversal of the pulse direction and another parcel of momentum $2(n^2 - 1)p_0/n$ present in the surrounding fluid, resulting in a final mirror momentum $2np_0$. Because the final mirror momentum for all postulates is the same, and differences in the mediating mechanisms are likely immeasurable, the five postulates in this case are degenerate.

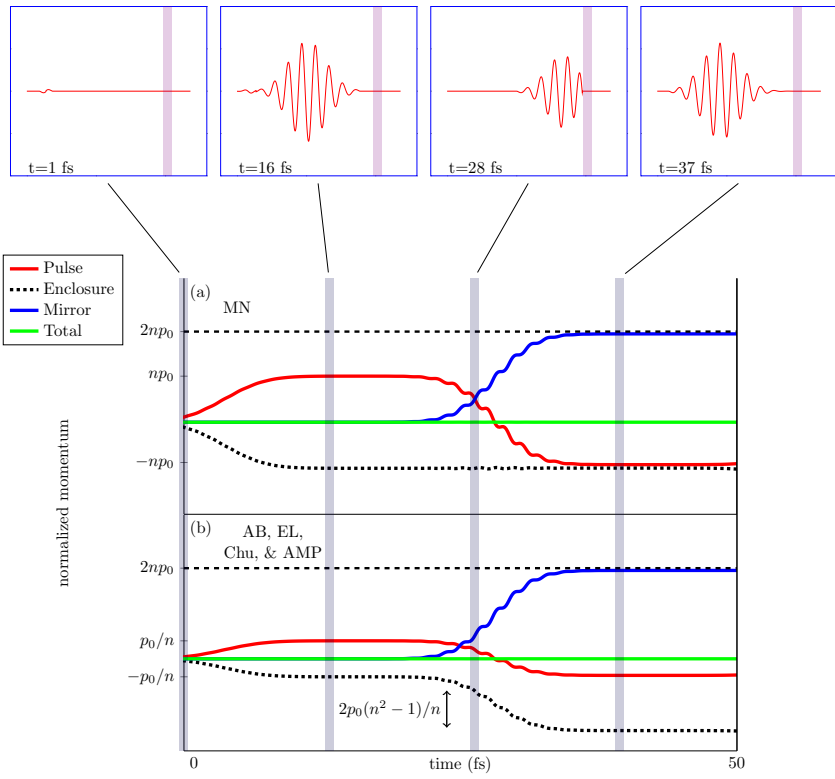


Figure 4.11: Momentum transfer between a pulse ($\lambda_0 = 632$ nm, $\tau = 2$ fs) in an enclosure containing a fluid ($n = 1.6$) and a submerged mirror approximated as a perfect electric conductor. The top panel shows simulation snap-shots of the electric field as the pulse is reflected from the mirror. The momentum of the pulse (red solid line), enclosure and surrounding fluid (black dotted line), mirror (blue solid line), and total system (green solid line) predicted by (a) the Minkowski postulates and (b) the Abraham, Einstein-Laub, Chu, and Amperian postulates. All five postulates predict the same final slab momentum of $2np_0$. Note that the enclosure and surrounding fluid are connected such that the momentum associated with both are lumped together.

Lorentz force calculations of radiation pressure on a submerged reflector imparting arbitrary phase show that the acquired momentum can vary continuously with phase between an upper bound of the Minkowski momentum and a lower bound of the Abraham momentum [75, 76]. Pulse interaction with a perfect magnetic conductor – the compliment of a perfect electric conductor – illustrates how a half-cycle phase shift in the reflected electric field can drastically alter radiation pressure predictions. Repeating the previous example using a perfect magnetic conductor in Figure 4.12 shows that all postulates remain faithful to global momentum conservation, but the degeneracy of the final mirror momentum is now broken. The Minkowski and Abraham postulates predict a final mirror momentum $2np_0$ resulting from either two-body or three-body momentum transfer processes upon pulse reflection. The Einstein-Laub, Chu, and Amperian postulates, on the other hand, predict a smaller final slab momentum of $2p_0/n$, which is acquired directly by the reversal of the pulse momentum without the accompanying system recoil observed for the case of a perfect electric conductor.

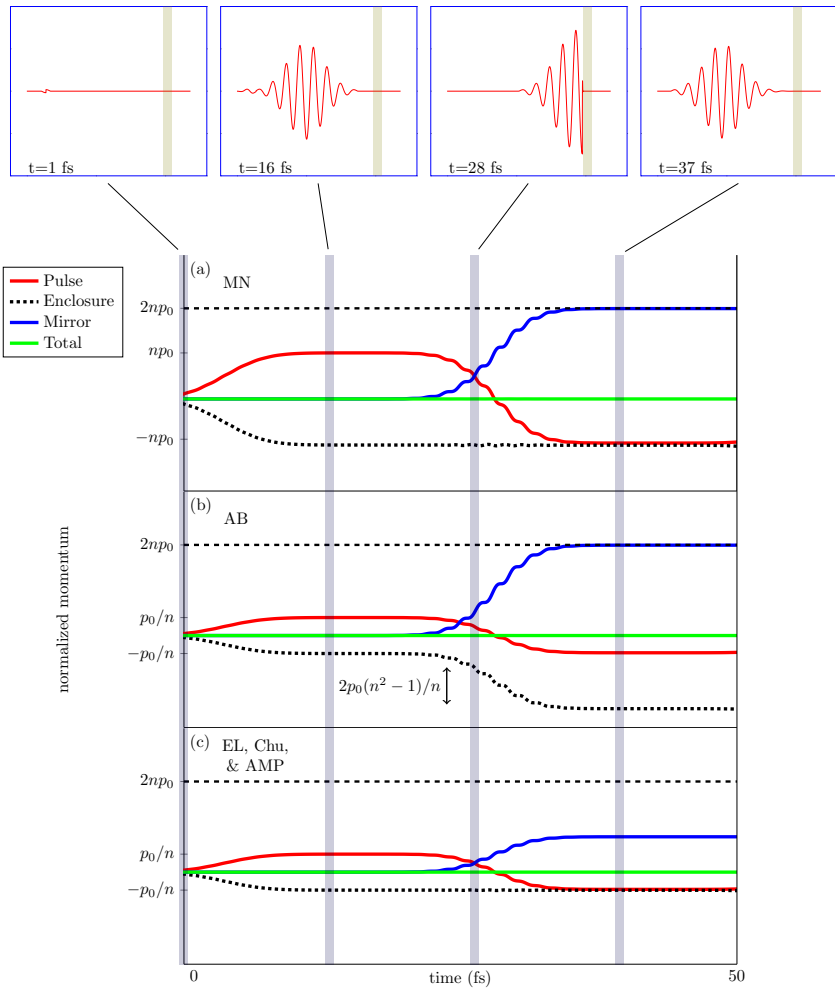


Figure 4.12: Momentum transfer between a pulse ($\lambda_0 = 632 \text{ nm}$, $\tau = 2 \text{ fs}$) in an enclosure containing a fluid ($n = 1.6$) and a submerged mirror approximated as a perfect magnetic conductor. The top panel shows simulation snap-shots of the electric field as the pulse is reflected from the mirror. The momentum of the pulse (red solid line), enclosure and the surrounding fluid (black dotted line), mirror (blue solid line), and total system (green solid line) predicted by (a) the Minkowski postulates, (b) the Abraham postulates, and (c) the Einstein-Laub, Chu, and Amperian postulates. The Minkowski and Abraham postulates predict a final slab momentum of $2np_0$, whereas the Einstein-Laub, Chu, and Amperian postulates predict a final slab momentum of $2p_0/n$. Note that the enclosure and surrounding fluid are connected such that the momentum associated with both are lumped together.

Given that radiation pressure on submerged mirrors is not completely degenerate and can be phase dependent, accurate modelling of the Jones-Richards and Jones-Leslie experiments must fully account for the specific configurations in which radiation pressure is generated. We use the five electrodynamic postulates in simulations that describe the two experiments to a degree of realism unmatched to date. The simulations incorporate realistic experimental conditions such as broadband illumination, the skin effect in a metallic mirror, multiple reflections in a dielectric mirror, and frequency-dependent dispersion. To mimic power normalization used in both experiments, the incident time-averaged power flux for each case of immersing fluid is kept constant, a consideration whose importance has been recently pointed out [77].

We begin by considering the Jones-Richards experiment in which incoherent, broadband light from a tungsten lamp illuminates a rhodium-coated silver mirror. Virtual replication of the original experiment is limited by missing information, such as the spectral distribution of the tungsten lamp, the complex permittivity of the rhodium-coated silver, and the thicknesses of rhodium and silver. In the absence of these details, we make the reasonable assumption that the mirror is made from either bulk rhodium or bulk silver, modelling each metal by fitting the Drude model to experimentally measured permittivity values found in [79] for rhodium and [80] for silver. The tungsten light source is modelled as a summation of incoherent plane waves with a Gaussian spectral distribution centered at the wavelength 632 nm. Key assumptions of the analysis, including how the Drude model is fitted to permittivity values of rhodium and silver, and the assumed spectral distribution of the tungsten light source, are shown in Figure 4.13.

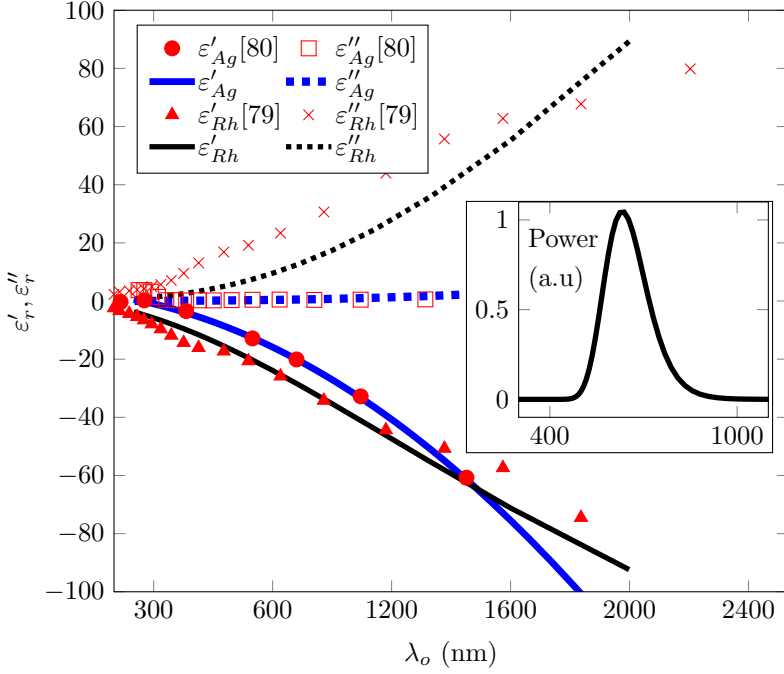


Figure 4.13: Key assumptions used to model the Jones-Richards experiment. The real part of complex permittivity ϵ' (solid lines) and the imaginary part of the complex permittivity ϵ'' (dotted lines) produced by the Drude model when fitted to tabulated permittivity values of rhodium (markers: triangle, cross) [79] or silver (markers: circle, square) [80]. The inset depicts the power spectrum of a broadband incoherent light source assumed to emulate light from the tungsten lamp used in the Jones-Richards experiment.

The radiation pressure on a submerged metallic mirror predicted by different postulates can change dramatically depending on the assumed properties of the mirror. As shown in Figure 4.14 (a), if the mirror is assumed to be a perfect electric conductor, all five postulates identically predict pressure that linearly scales with the fluid index, a result that matches within the experimental error. Not surprisingly, the predicted pressure becomes inversely proportional to the fluid index for the Einstein-Laub, Chu, and Amperian postulates when the perfect electric mirror is replaced by a perfect magnetic mirror. However, when we model the metallic mirror as a dispersive metal, the coincidence between theory and experiment seen before by assuming a perfect electric conductor is weakened. Incorporating the dispersion of the metal introduces two realistic effects: losses in the metal and a slight, but non-zero, phase shift imparted by reflection. As shown in Figure 4.14 (b), the pressures predicted by all five postulates exhibit departures from the Jones-Richards experimental data that become significant for higher fluid index values. This departure is even more pronounced if the mirror is rhodium as opposed to silver, due to the larger optical losses of rhodium, which fall further from the perfect electric conductor approximation. For identical

simulation parameters, the Einstein-Laub, Chu, and Amperian postulates are generally in worse agreement to the experimental data than the Abraham and Minkowski postulates. However, without detailed knowledge of the exact composition of the rhodium-coated silver mirror, it is not possible to conclude whether any of the postulates accurately predict the Jones-Richards results. Further radiation pressure measurements using well-characterized metallic mirrors are thus a necessary step toward the isolation of an electrodynamic theory.

We next consider the Jones-Leslie experiment in which coherent radiation from a laser illuminates a submerged dielectric layered mirror, which results in pressure scaling linearly with fluid index. Again, virtual replication of the original experiment is limited because the composition of the dielectric mirror (which was purchased from a vendor) was not reported. Here, we assume a dielectric mirror made from alternating, quarter-wavelength-thick layers of MgF_2 ($n = 1.37$) and ZnS ($n = 2.35$), a recipe reported by Jones and Leslie [14] to make some of the other mirrors used in their experiment. Interestingly, the ordering of the layers can significantly alter the radiation pressure predicted by some of the postulates, as shown in Figure 4.14 (c). The Abraham and Minkowski postulates predict a pressure proportional to n regardless of the layer ordering, but the other three postulates predict either n -proportional or $1/n$ -proportional radiation pressure depending on whether the higher-index layer (ZnS) or the lower-index layer (MgF_2) is the exterior layer in contact with the surrounding fluid. The sensitivity of the radiation pressure to the layer ordering arises from the phase variations in the reflection from a dielectric mirror. That is, the phase of reflection from a dielectric mirror when capped by the higher-index layer is like that from a perfect electric mirror. When capped by the lower-index layer, it is like that from a perfect magnetic mirror. Without knowing the composition of the dielectric mirror used in the Jones-Leslie experiment, we cannot rule out any of the postulates on the basis of the experimental accord, since all postulates are capable of predicting the n -proportional radiation pressure in agreement with the experimental data. In light of this analysis, an essential experiment to test the hypothesis of phase-dependent radiation pressure is to measure the radiation pressure difference on two submerged dielectric mirrors whose layers are ordered differently but otherwise identical.

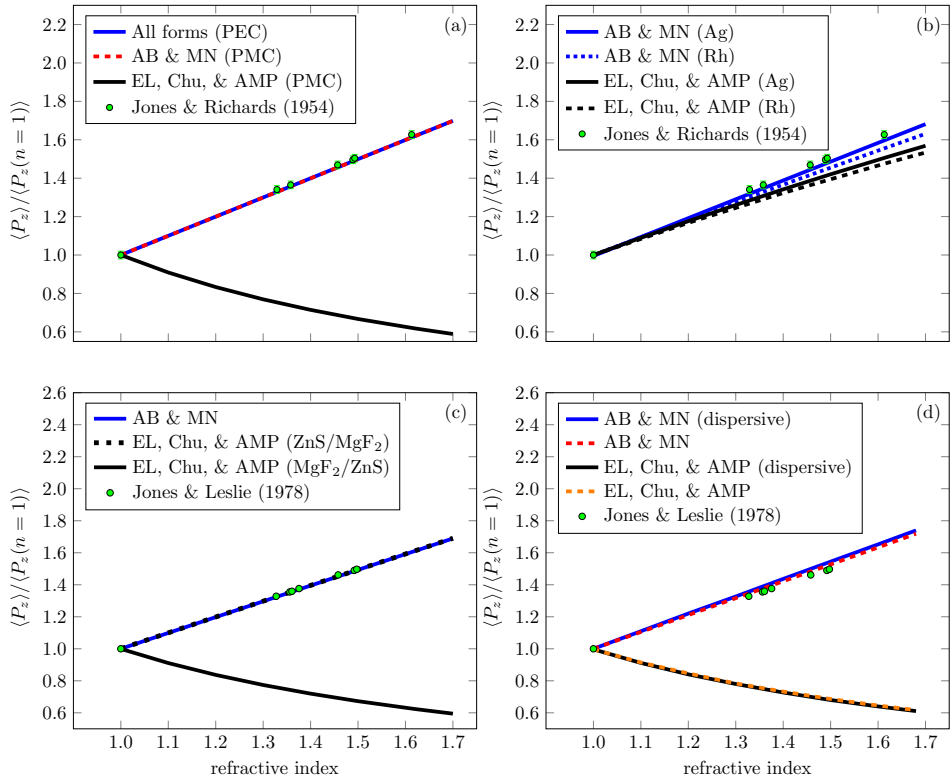


Figure 4.14: Normalized time-averaged radiation pressure on submerged mirrors predicted by the Minkowski, Abraham, Einstein-Laub, Chu, and Amperian postulates. The green dots and error bars in (a) and (b) are data from the 1954 Jones-Richards experiment [13]. The green dots in (c) and (d) are data from the 1978 Jones-Leslie experiment [14]. Note that the error in the 1978 Jones-Leslie experiment is smaller than the dot size. The mirrors, immersed in fluids with refractive index n that varies from 1.0 to 1.7 in steps of 0.1, are illuminated at normal incidence. Pressure predictions are made for the following cases: (a) A perfect mirror (electric or magnetic) submerged in fluids without dispersion; (b) a mirror made of dispersive silver or rhodium (whose permittivity is modeled using the Drude model fitted to tabulated data [80, 79]); (c) a multi-layered dielectric mirror composed of alternating $\lambda_0/4$ -thick layers of MgF₂ (refractive index 1.38) and ZnS (refractive index 2.35) submerged in fluids without dispersion fluids for configurations in which the outermost dielectric layer is MgF₂ (MgF₂/ZnS) or ZnS (ZnS/MgF₂); (d) a multi-layered (MgF₂/ZnS) dielectric mirror where the amount of dispersion in the fluids is set to $n_g \approx 1.03n$, where n_g is the group refractive index and n is the phase refractive index (corresponding to the maximum upper bound of the fluid dispersion as reported by Jones and Leslie [14]). The mirrors in (a) and (b) are illuminated at normal incidence by an incoherent white light source with spectral intensity shown in the inset of Figure 4.13, which approximates a tungsten lamp. The mirrors in (c) and (d) are illuminated at normal incidence at the wavelength $\lambda_0 = 632.8$ nm.

An important conclusion of the Jones-Leslie experiment is that radiation pressure is dependent on the phase refractive index as opposed to the group refractive index. We simulate the pressure on dielectric mirrors (with a low-index capping layer) immersed in fluids that are modelled as dispersive dielectrics with variations in group and phase refractive index matching those reported by Jones and Leslie [14]. As shown in Figure 4.14 (d), adding the effect of dispersion to the surrounding fluid medium has a negligible effect on the pressure trends for all postulates, which remain dependent on phase refractive index.

Interpretations of radiation pressure on submerged mirrors are muddled by the presence of force densities residing in the adjacent fluid. There is no consensus on the importance of these contributions to the total radiation pressure on the mirror, as they have been neglected by some [77] and incorporated by others [78, 81]. To illustrate their relative importance for each of the five postulates, Figures 4.15 (a) and (b) plot the time-averaged force density exerted by a normally incident continuous wave onto a multi-layered dielectric mirror, capped by a low-index layer and a high-index layer, respectively. The Minkowski and Abraham postulates predict a series of pressure spikes localized at the interfaces of the dielectric mirror but no force density in the fluid region. The Einstein-Laub, Chu, and Amperian postulates, on the other hand, predict oscillatory force density patterns that span across the fluid and dielectric mirror regions. Consistent with previous observations, the force density in the dielectric mirror is larger when the mirror is capped by the higher-index layer. The force density in the fluid region can add or subtract to the total radiation pressure on the submerged mirror. As shown in Figure 4.16, the pressure on the mirror oscillates between n and $1/n$ by accounting for the force density every quarter cycle into the fluid, matching similar predictions made in [42, 75]. This adds an additional layer of complexity to the interpretation of the Jones-Leslie experiments, as the observed index proportionality of radiation pressure measured by Jones and Leslie can be recovered by the Einstein-Laub, Chu, and Amperian postulates through selective force density integration into the fluid.

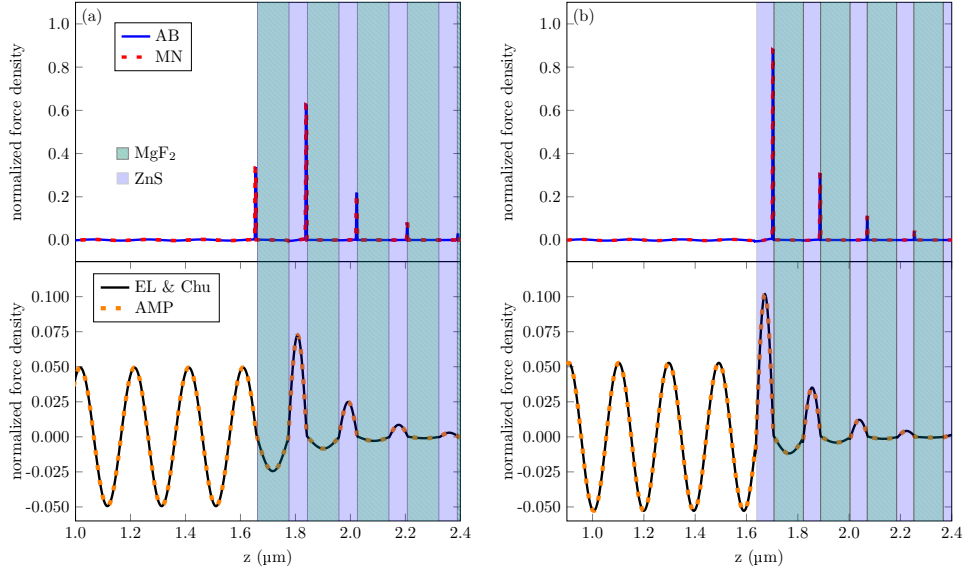


Figure 4.15: Time-averaged force density distributions predicted by the Minkowski, Abraham, Einstein-Laub, Chu, and Amperian postulates, shown for the case of a continuous-wave beam ($\lambda_0 = 632.8$ nm) normally incident onto a dielectric mirror composed of alternating $\lambda_0/4$ -thick layers of MgF_2 and ZnS submerged in a fluid of refractive index $n = 1.6$. We consider the configuration for which the dielectric mirror is capped by (a) the lower-index layer and (b) the higher-index layer. Degenerate time-averaged force density distributions predicted by (top) the Abraham (solid blue) and Minkowski (dashed red) postulates and (bottom) the Einstein-Laub and Chu postulates (solid black) and the Amperian postulates (dashed orange). The former is dominated by strong surface forces localized at transitions from high to low refractive index regions, whereas the latter is dominated by weaker oscillatory body forces extending across the fluid and mirror regions. All force density distributions have been normalized to the peak instantaneous Abraham force density.

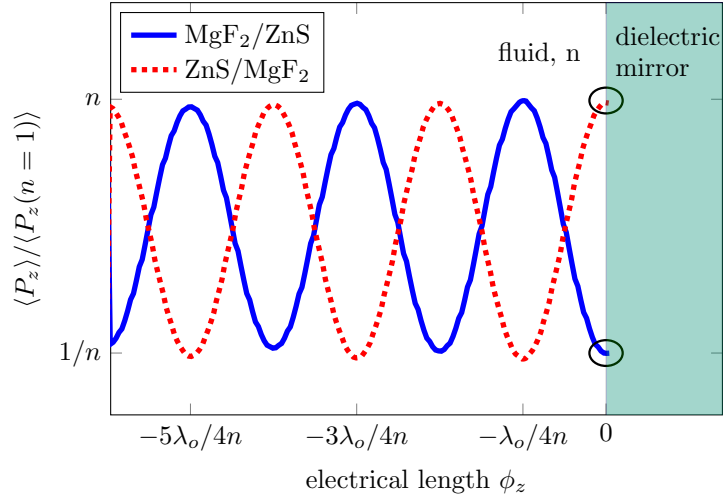


Figure 4.16: Normalized radiation pressure on a submerged dielectric mirror predicted by the Einstein-Laub, Chu, and Amperian postulates as a function of the force density integration distance into the fluid for cases in which the dielectric mirror is capped by either the lower-index layer (blue solid) or the higher-index layer (red dashed). Here, n represents the refractive index of the surrounding fluid medium. The circles denote the nominal radiation pressure when the force density is integrated up to the boundary of the mirror. The addition of body forces in the fluid causes the normalized radiation pressure to oscillate between an upper bound of n and a lower bound of $1/n$.

4.6 Radiation Pressure at Fluid Interfaces

Perhaps the simplest configuration to probe the momentum of light is to observe its passage across the threshold between vacuum and a dielectric medium. Changes in the momentum of light upon entering the medium should be offset by an-axis recoil dependent on whether momentum takes on Minkowski or Abraham forms [82, 83]. For the simple case of a beam of intensity I normally incident from air onto a dielectric medium of refractive index n , the Minkowski form of momentum predicts a negative pressure (pull) of [82]

$$P = -\frac{2I}{c} \frac{n-1}{n+1}, \quad (4.9)$$

whereas the Abraham form of momentum predicts a positive pressure (push) of

$$P = \frac{2I}{c} \frac{n-1}{n+1}. \quad (4.10)$$

In 1973, Ashkin and Dziedzic [15] performed an experiment to measure the longitudinal recoil exerted by pulses entering a deformable dielectric medium. In their experiment, an air-water interface was illuminated with high-power (3 kW), 60-ns-long, 530-nm-wavelength laser pulses focused down to a spot size of radius 2 μm . Based on the far-field profile of the transmitted pulse, they inferred that the pulse induced a momentary, micron-scale, upward bulge on the water surface, overcoming both surface tension ($\simeq 7 \text{ mJ/m}^2$ at room temperature) and gravity. The direction of the bulge, consistent for illumination downward from the air or upward from water, was initially interpreted by Ashkin and Dziedzic as evidence of the on-axis recoil associated with the Minkowski form of light momentum [15]. Subsequently, Gordon [84] proposed an alternative explanation based on compressive lateral radiation forces squeezing the water into the highest-intensity region of the beam, a so-called “toothpaste” effect that forced water to bulge up into the air above. This viewpoint has gained traction [25, 85] but has yet to be proven. Recently, laser-induced deformations of an air-water interface were shown to be accurately modelled without explicitly invoking compressive forces [83, 86]. The model described interface deformation using the Navier-Stokes equation driven by a Minkowski-like on-axis recoil given by equation 4.9, which is evidence that suggests a Minkowski form of momentum.

Radiation-induced fluid deformations of much greater effect have been studied by Casner et al. [16, 17, 18, 19, 20]. In place of an air-water interface was a carefully designed liquid-liquid interface, where the composition of the liquids was tuned to achieve a surface tension 10^4 times smaller than that of an air-water interface. Because the higher-index fluid sat

atop the lower-index fluid, deformation of the interface towards the lower-index fluid would be directed along, rather than opposed to, gravity. It was shown that illumination of the fluid-fluid interface with even a moderately-powered ($\simeq 150$ mW) continuous-wave 632-nm-wavelength laser beam could cause millimeter-scale downward bulges into the lower-index liquid, irrespectively of the illumination direction [19, 20]. The much larger bulge magnitudes enabled detailed studies of the interface morphology and asymmetric deformations dependent on illumination direction [87]. The similarities in the light-induced deformations observed for air-water and liquid-liquid interfaces – both deform from high-index to low-index regions – suggest a common physical origin, but a consolidated model rooted in the basic electrodynamic postulates has yet to be proposed. Such efforts, however, are important for resolving the roles of lateral and longitudinal forces and elucidating the link, if any, between fluid deformations and light momentum in matter.

Realistic descriptions of radiation-induced fluid deformation must abandon the assumption of material rigidity, a significant departure from ideality that requires careful re-examination of the nature of recoil. Figure 4.17 shows snap-shots of the instantaneous force density distribution described by all five postulates, in the case of a plane wave impinging at normal incidence onto a dielectric from free space. The force density distributions are characterized by localized surface pressure (Minkowski), undulating body forces (Einstein-Laub, Chu, and Amperian), or a combination of both (Abraham). Under the assumption that the medium is rigid, momentary imbalances in the force density distribution extending across the entire medium can result in a net recoil. However, under the realistic assumption that the medium is deformable, such recoil mechanisms are impossible as it requires instantaneous communication of force density across finite extents. Instead, each element of the medium is locally driven by a time-averaged force density, which, as shown in Figure 4.17, can be substantially different from the instantaneous force density. Time-averaging generally diminishes the undulations in the instantaneous force density distributions, so much so for the Abraham force density that it becomes indistinguishable from the Minkowski force density. In this case, models of recoil based on the Minkowski and Abraham time-averaged force densities predict identical backwards recoil driven entirely by surface pressure. This contrasts to classical models of recoil based simply on changes in light momentum at threshold of a dielectric, which predict opposing recoils for light momentum of Minkowski and Abraham forms [82, 83].

Both electrodynamics and fluid dynamics are needed to completely understand how fluids deform under radiation pressure. Since the time scales of fluid deformation are much greater than the times scales of electromagnetic oscillation (particularly at visible

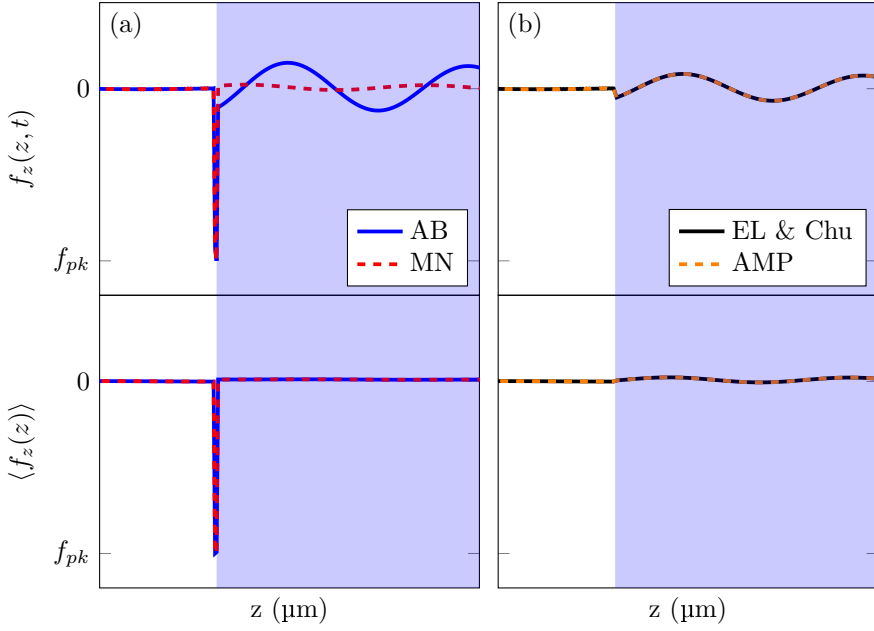


Figure 4.17: Instantaneous (top row) and time-averaged (bottom row) electromagnetic force density distribution exerted by a continuous-wave beam ($\lambda_0 = 632.8$ nm) normally incident from air onto water ($n = 1.33$) predicted by (a) the Abraham (solid blue) and Minkowski (dashed red) postulates and (b) the Einstein-Laub and Chu postulates (solid black) and the Amperian postulates (dashed orange).

frequencies), the physics of radiation-induced fluid deformation can be captured without solving the electrodynamic and fluid dynamic equations simultaneously. We use a coupled electrodynamic-hydrodynamic simulator in which Maxwell's equations and the Navier-Stokes equations are solved on respective grids of fine and coarse spatio-temporal resolution. The electrodynamic simulator calculates the time-averaged force density, which is ported to the hydrodynamic simulator to calculate an updated fluid geometry. We examine two configurations: pulsed excitation of an air-water interface like in the Ashkin-Dziedzic experiment [15] and continuous-wave visible excitation of a low-tension fluid-fluid interface like in the experiments by Casner et al. [19, 20]. To emulate impulsive excitation, we drive the hydrodynamic simulator at a single coarse time step with the time-averaged force density profile calculated for the initial fluid configuration, which is a valid procedure only because the coarse time step is several orders of magnitude longer than the pulse duration. To emulate continuous-wave excitation, we cyclically compute the time-averaged force density and resulting fluid geometry each time the interface has deformed by at least one coarse space step. The simulations assume a simplified two-dimensional configuration which does not fully describe the tightly focused beams used in the experiments [15, 19, 20], but has a sufficient degree of complexity to illustrate lateral forces associated with electrostriction and field gradients.

Figure 4.18 illustrates the initial time-average force distribution applied to an impulsively-excited air-water interface and the ensuing interface deformation and fluid velocity. Three unique sets of bulge dynamics emerge. For both transverse-magnetic (TM) and transverse-electric (TE) polarizations, only the Abraham, Minkowski, and Einstein-Laub postulates predict an upward bulge for illumination from air or water, qualitatively consistent with the results of the Ashkin-Dziedzic experiment [15]. The Amperian and Chu postulates, on the other hand, predict upward bulges for TE polarization, which are smaller than those predicted by the other postulates, and downward bulges for TM polarization. The latter case provides further proof of the empirical invalidity of the Amperian and Chu postulates. This conclusion is consistent with those made by Mansuripur et al. [88] after comparing the effect imparted by a beam to a dielectric medium using the Einstein-Laub and Lorentz force densities.

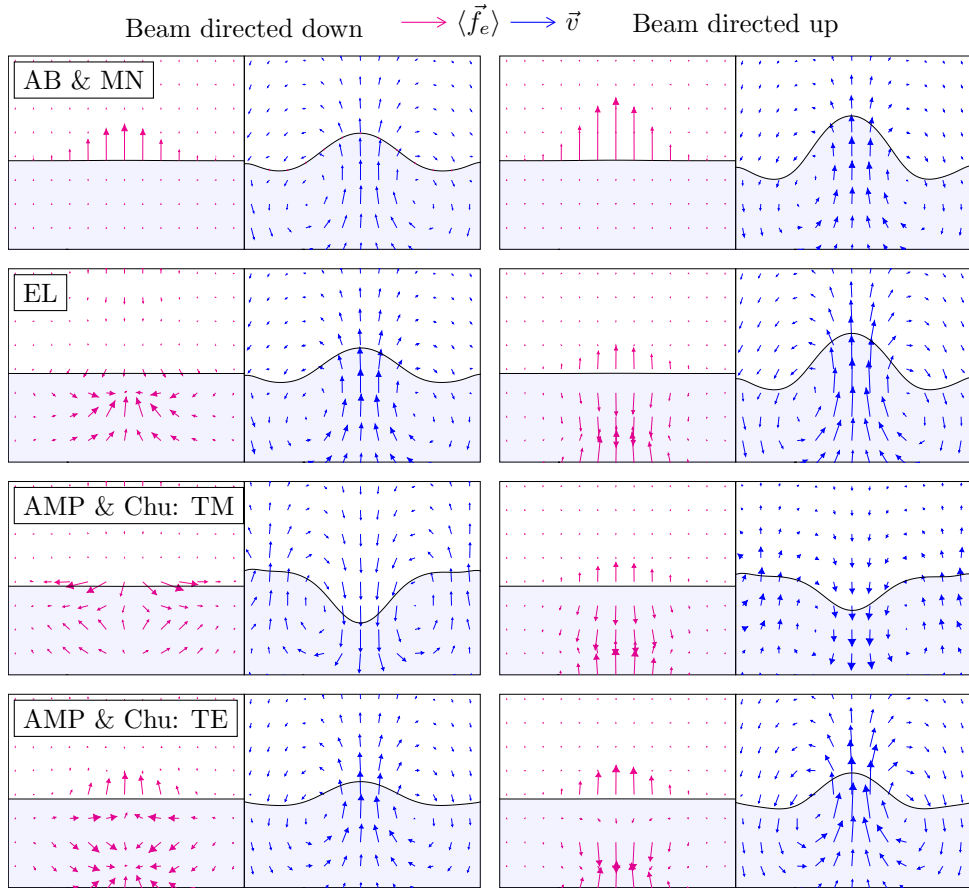


Figure 4.18: Two-dimensional fluid dynamic simulations representative of the Ashkin-Dziedzic experiment [15]. The lower fluid (blue) represents water ($n=1.33$) and the upper fluid (white) represents air ($n=1$). The air-water interface is excited by a 60-ns-long, 530-nm-wavelength pulse at normal incidence. The time-averaged force density distributions exerted by the pulse are calculated using the Minkowski, Abraham, Einstein-Laub, Chu, and Amperian postulates (magenta arrows), which are shown next to the resulting velocity field (blue arrows) of the deformed interface. We set the surface tension of the water-air interface to $\sigma = 0.7 \text{ mN/m}$ and the viscosity of water to $\eta = 1 \text{ mPa}\cdot\text{s}$. The Abraham, Minkowski, and Einstein-Laub postulates predict an upward bulge for TE and TM polarizations for both illumination directions. The Amperian postulates predict an upward or downward bulge for TM and TE polarizations, respectively. Mesh refinement studies have been performed to ensure convergence of the simulated fluid behaviour.

The Abraham, Minkowski, and Einstein-Laub postulates offer two physical mechanisms to explain the appearance of an upward bulge: it can arise from a longitudinal upward force density localized at the interface (Minkowski and Abraham) or a lateral compressive force density applied to the bulk of water (Einstein-Laub). The former is consistent with the Minkowski surface recoil described by equation 4.9, and the latter describes the toothpaste effect suggested by Gordon [84]. The bulge shape and size resulting from either mechanism are nearly identical and indistinguishable with respect to the precision of the Ashkin-Dziedzic experiment [15], although repetition of the experiment with fluids of different viscosities and mass densities may lead to more diverse bulge shapes that better distinguish surface and body effects. For the Abraham, Minkowski, and Einstein-Laub postulates, illumination from water yields larger bulges than illumination from air, a general consequence of the larger field magnitudes and larger force densities in water when it is used as the incidence region. The interplay between force density distributions and interface deformation can be complex. For example, the Einstein-Laub postulates predict downward body forces when illuminated from water, which are overwhelmed by an upward surface force and overall compressive forces that conspire to generate an upward bulge.

The bulge dynamics observed by Casner et al. [19, 20] for a fluid-fluid interface have been distinguished by two regimes: a low-power regime in which the bulge sizes are small and scale linearly with power and a high-power regime in which the bulge exhibits large interface instabilities. Recent investigations have suggested that the instabilities in the high-power regime are likely caused by surface heating [87], which cannot be treated by our simulations. We therefore restrict our analysis to the low-power regime. Figure 4.19 shows two sets of simulated bulge and force distribution dynamics: one predicted by the Abraham or Minkowski postulates and the other by the Einstein-Laub postulates. The bulge dynamics of the fluid-fluid interface are consistent with the dynamics of the air-water interface, but reversed in direction since the optically denser region now resides above the interface. The downward bulge for both illumination directions and the slightly larger bulge sizes for downward illumination are both consistent with the observations [19, 20]. The bulge can originate from a downward surface pressure (Minkowski and Abraham) or a pinching effect distributed throughout the bulk (Einstein-Laub). Bulges due to surface pressure exhibit larger asymmetries with respect to illumination direction, a feature potentially useful for empirical validation of the two mechanisms of bulge formation.

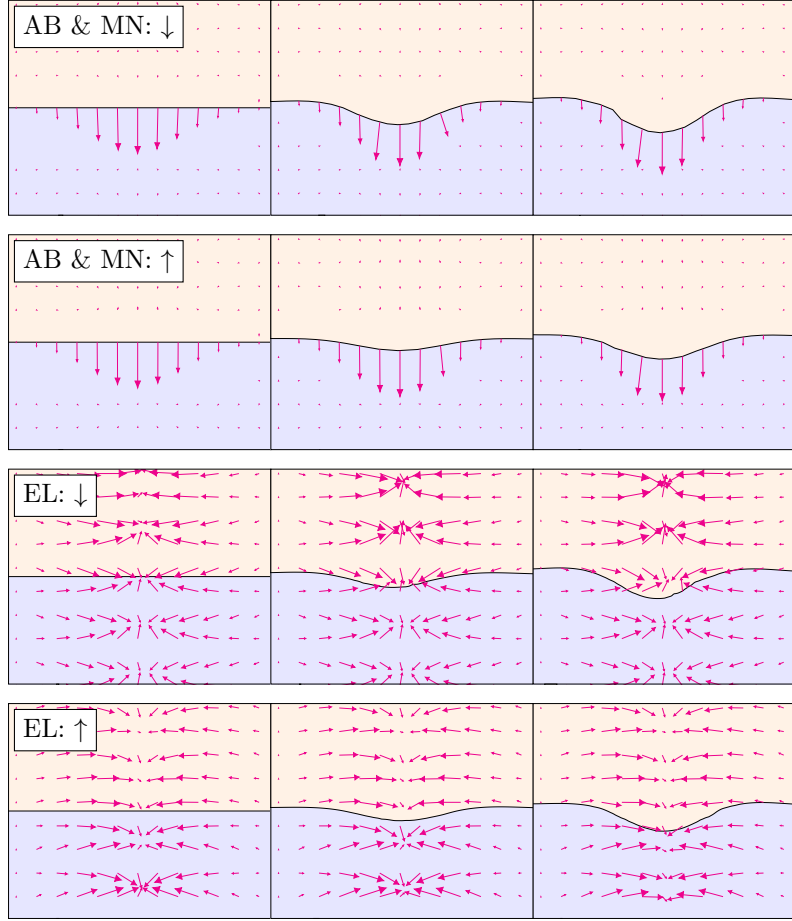


Figure 4.19: Two-dimensional fluid dynamic simulations representative of the experiments by Casner et al. [19, 20]. These experiments used a micellar phase of microemulsions made from a liquid mixture of mass composition 9% water, 4% sodium dodecyl sulfate, 70% toluene, and 17% n-butanol. Below the critical temperature of 35 C° , the mixture separates into two phases of different micellar concentrations. The two phases are represented in the simulations as two continuous fluid media in which the upper fluid (beige) has index $n = 1.49$ and mass density $\rho = 853\text{ kg/m}^3$ and the lower fluid (blue) has index $n = 1.46$ and mass density $\rho = 1017\text{ kg/m}^3$ [89]. Near the critical temperature, the fluids have the same viscosity of $\eta = 1.3\text{ mPa}\cdot\text{s}$ and an extremely low surface tension of $0.1\text{ }\mu\text{N/m}$. The fluid mixture is excited by a continuous-wave TM-polarized beam ($\lambda_0 = 532\text{ nm}$) with a Gaussian profile. The time-averaged electromagnetic force density distributions (magenta arrows) calculated using the Minkowski, Abraham, and Einstein-Laub postulates for downward (\downarrow) and upward (\uparrow) illumination are shown for three instances during the evolution of a radiation-pressure-driven surface bulge. The three postulates all predict downward bulge formation from the high-index region into the low-index region, consistent with the observations by Casner et al.[89]. Mesh refinement studies have been performed to ensure convergence of the simulated fluid behaviour.

4.7 Optical Tweezing

The most common application of radiation pressure is for moving small objects in low-friction environments, a practice known as optical tweezing. Popular examples are found in biology, such as trapping of bacteria for selective destruction [90] and measurement of the forces involved in RNA transcription [91]. Optical tweezers are generally considered to operate using two different kinds of forces: gradient forces, and scattering forces. Gradient forces refer to a particle's tendency to move towards the location of highest beam intensity, and scattering forces are related to forces produced during reflection and transmission at the interface between two media. Gradient forces can be thought of as primarily dependent on the spatial derivative of the electromagnetic energy density, whereas scattering forces can exist in the absence of spatial gradients. Interestingly, one way to understand gradient forces is based on energy minimization. Recall in Section 2.3.1 where the force on a piece of steel was found by considering a force equal to the work needed to overcome the change in magnetic energy inside the iron relative to that just outside it. Gradient forces on dielectric particles can be understood in a similar way, where the energy of an optical tweezing system is minimized when a dielectric particle is at the center of highest beam intensity [92]. For optical tweezers, the magnitude of this gradient force relative to the scattering forces also has to be considered, an interesting topic that is outside of the scope of this thesis. An avenue of potential further work is to use the numerical methods in this thesis to quantify the different magnitudes of scattering and gradient forces for various optical tweezing configurations. This would be an important step towards a complete theory of optical tweezers, which has yet to be developed [93, 48].

Barton et al. [94] pioneered the approach of using Mie theory to express the fields scattered from a spherical particle in conjunction with the electromagnetic stress tensor to calculate the force on that particle. The original expressions derived by this approach [94] used the Minkowski form of the stress tensor, whose use was based on the work by [25] and [27]. The decision to use the Minkowski stress tensor over the alternatives has little consequence. As shown previously, the Minkowski form is identical to the Abraham predictions for all time-averaged cases considered so far. Pfeifer et al. [95] have also argued that the Minkowski and Abraham postulates describe optical tweezers equivalently, differing only with respect to ease of implementation. This seems to contradict calculations by Mansuripur et al. [88] of the force density within illuminated dielectric particles, which suggest that various postulates can be distinguished by differences in their distributions of force density.

To explore how different postulates describe optical tweezer effects, Figure 4.20 (a) depicts simulations that use all five postulates to model the interaction between a focused continuous-wave laser beam with a small submerged dielectric cylinder placed at the edge of the beam's focus. For both TM and TE polarizations, only the Minkowski, Abraham, and Einstein-Laub postulates are consistent with optical trapping: the beam exerts a time-averaged force that drags the particle into the focus and pushes it along the direction of beam propagation [96]. The Amperian and Chu postulates, on the other hand, predict particle trapping for TE polarization and particle expulsion for TM polarization. Forces predicted by the Einstein-Laub postulates also exhibit polarization sensitivity, but to a much lesser extent. The reason for this difference is because the Einstein-Laub, Chu, and Amperian forms have dominant body force terms that are dependent on the interference pattern within the particle. In contrast, the Abraham and Minkowski forms are dominated by momentum exchange at the interface between two media, as demonstrated previously in Figure 4.15.

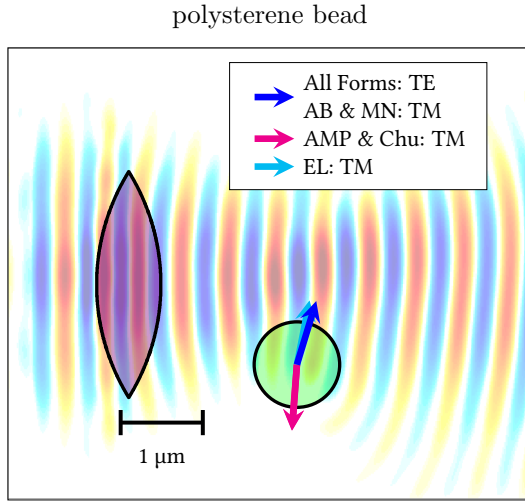


Figure 4.20: Simulated radiation pressure on a polystyrene bead (green) placed at the edge of the focal point of a continuous-wave beam ($\lambda_0 = 532$ nm) in a background medium of water ($n = 1.33$). The polystyrene bead ($n = 1.58$) has a diameter of 820 nm and the force acting on it has been determined under the rigid body assumption by integrating the force density distribution within the bead calculated using the Minkowski, Abraham, Einstein-Laub, Chu, and Amperian postulates. The bead is shown immersed in a background electromagnetic field calculated using the FDTD method.

Experiments by Ashkin [96] have shown that air bubbles near a focused beam are repelled from the focus and pushed along the direction of beam propagation. Whereas the actuation of a dielectric particle is driven by optical forces acting on or within the particle, the actuation of an air bubble is driven by optical forces acting on the fluid region surrounding the bubble. To compare experimental observations with theory, we simulate the dynamics of an air bubble near a focused beam using the electrodynamic-hydrodynamic simulator. As shown in Figure 4.21 (b), the five postulates all predict that the air bubble is displaced away from the beam focus and along the direction of beam propagation, which is qualitatively consistent with past observations by Ashkin [96]. Predictions of bubble expulsion differ in terms of rate, shape, and trajectory. Similar to previous examples, the five postulates applied to the case of TM polarization yield three unique sets of dynamics: one degenerate for Abraham and Minkowski postulates, another for the Einstein-Laub postulates, and a third degenerate for Amperian and Chu postulates. With all things equal, lateral bubble expulsion is predicted to be fastest for the Einstein-Laub postulates and slowest for the Amperian and Chu postulates, discrepancies which can potentially be validated by measurements.

In recent years, there has been increased interest in using light beams to “pull” on a particle such that the projection of its displacement onto the incident beam direction has a negative sign. This has been referred to as “tractor beaming” [97, 98, 99, 100, 101, 102, 103, 104]. For example, Kajorndejnukul et al. [103] showed that oil droplets confined at the interface of air and water can be pulled along the interface and into the direction of a lightly focused beam obliquely incident onto the droplets from the air region. This observation was interpreted to arise from an increase in the forward light momentum inside the droplet, propelling the droplet in the backward direction. Since the refractive index of the droplet is higher than that of air or water, an increase of light momentum in the droplet was attributed to a Minkowski form of momentum. Simulations of these experiments suggest that alternative explanations are feasible. As shown in Figure 4.22, the Minkowski, Abraham, and Einstein-Laub postulates all predict that an oil droplet resting at the interface of air and water can be pulled into the direction of an obliquely incident laser beam, despite differences in how they predict light momentum to scale with refractive index. The Amperian and Chu postulates, on the other hand, predict a push.

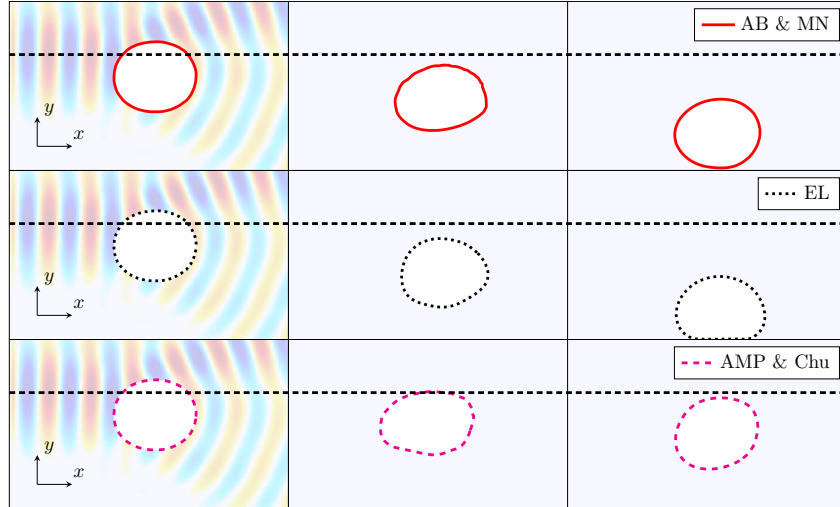


Figure 4.21: Simulated dynamics of an air bubble placed at the edge of the focal point of a TM-polarized, continuous-wave beam ($\lambda_0 = 532$ nm) in a background medium of water ($n = 1.33$, $\sigma = 0.7$ mN/m, $\eta = 1$ mPa·s). The air bubble ($n = 1.00$) has a diameter of 820 nm. The evolution of the deformable bubble in a background electromagnetic field is modelled in two-dimensions by solving both electrodynamic and fluid dynamic equations. The simulated bubble dynamics predicted by (top row) the Minkowski and Abraham postulates, (center row) the Einstein-Laub postulates, and (bottom row) the Chu and Amperian postulates. The dashed horizontal line indicates the axis of the focused beam. In all cases, the bubble is pushed away from the beam axis and along the direction of beam propagation, albeit with different bubble shapes and trajectories. Overall, the simulated behaviour using all postulates is qualitatively consistent with observations by Ashkin [96].

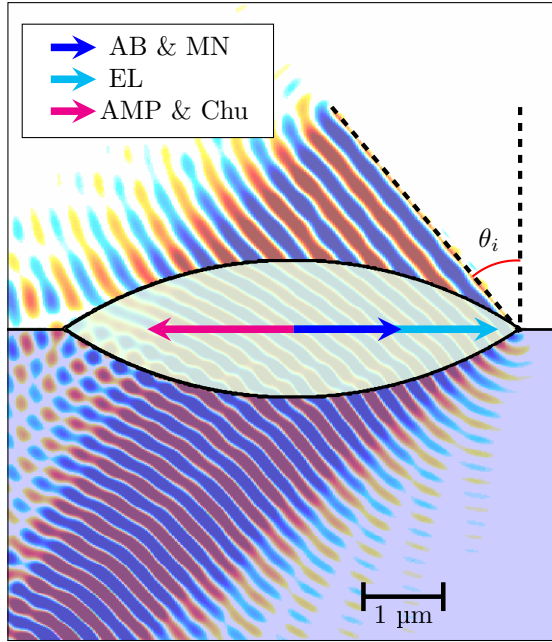


Figure 4.22: Tractor beaming of an oil droplet ($n = 1.42$) resting at the interface between air ($n = 1.0$) and water ($n = 1.33$). The length, height, and radius of curvature of the droplet are $6.4 \mu\text{m}$, $2 \mu\text{m}$, and $6 \mu\text{m}$, respectively, which are comparable to the dimensions of the droplets studied in [99]. A TM-polarized plane-wave ($\lambda_0 = 532 \text{ nm}$) is incident onto the droplet at an angle of incidence $\theta_i = 50^\circ$. Resulting forces predicted by the Minkowski and Abraham postulates (blue arrow), the Einstein-Laub postulates (dashed black arrow), and the Amperian and Chu postulates (magenta arrow). The reflected fields bouncing off the droplet and propagating behind the diagonal source line have been removed for clarity.

In another example of tractor beaming, Brzobohatý et al. [104] showed that two obliquely-incident plane waves can exert pulling forces on a dielectric particle placed in the region of beam interference. This observation was modeled by Barton et al. using the Minkowski stress tensor [94]. Figure 4.23 (a) and (b) shows simulations of a dielectric particle illuminated by two obliquely incident plane waves that work together to pull on the particle. Due to the highly symmetric illumination conditions that establish standing waves, all five postulates make identical force predictions for both polarizations. As shown in Figure 4.23 (c), the angle- and polarization-dependence of the normalized lateral force match the results from calculations presented in [104], all of which indicate a tractor-beaming effect for TE polarization and at steep angles of incidence. Thus, recent studies of tractor beaming do not offer experimental proof to pin down a single electrodynamic theory. Also demonstrated in this section is that a large portion of optical tweezer phenomena can be calculated using two dimensional finite difference techniques as opposed to complicated Mie theory approaches commonly implemented [104].

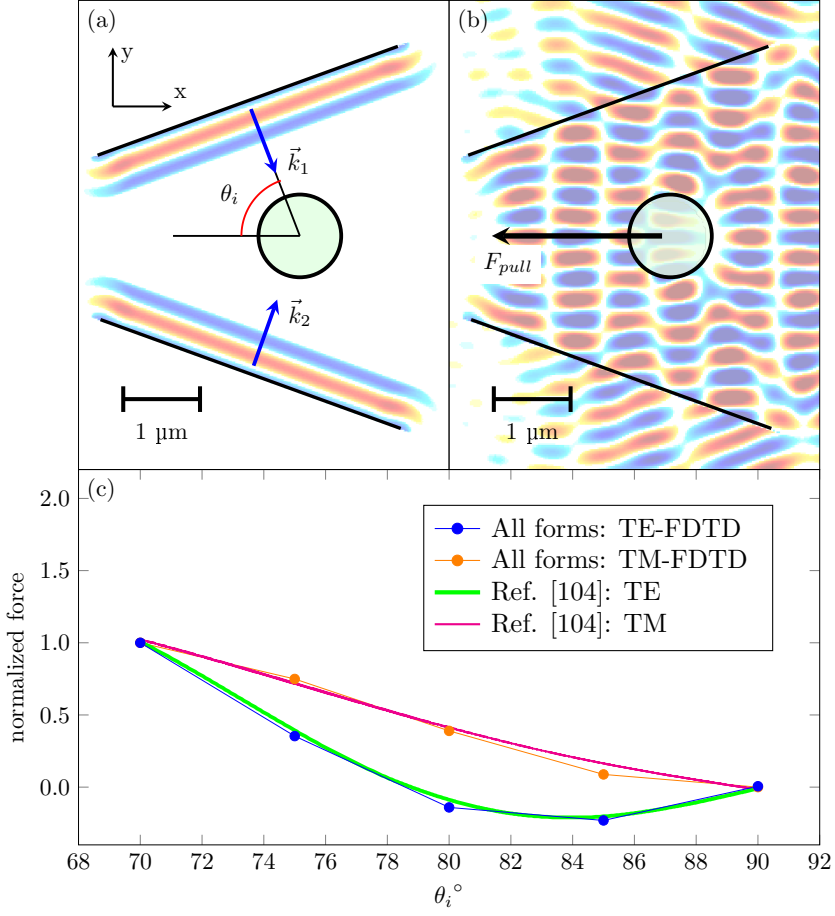


Figure 4.23: Tractor beaming of a dielectric particle using two obliquely incident plane waves. Simulation snapshots of two TE-polarized plane waves ($\lambda_0 = 532 \text{ nm}$) incident at $\theta_i = 70^\circ$ onto a polystyrene cylinder ($d = 820 \text{ nm}$, $n = 1.58$) immersed in water ($n = 1.33$), shown (a) before the plane waves strike the bead and (b) at steady state when the plane waves collide to exert a pulling force in the $-x$ direction. (c) Force on the bead calculated by FDTD using the Minkowski, Abraham, Einstein-Laub, Chu, and Amperian postulates for both TE (blue circles) and TM (orange circles) polarizations as a function of incident angle θ_i . The forces have been normalized to the force magnitude at $\theta_i = 70^\circ$. Under the highly symmetric illumination conditions studied here, all five postulates make degenerate force predictions. Pulling forces are only achieved for TE polarization within the range $76^\circ < \theta_i < 90^\circ$. Excellent agreement is observed with the three-dimensional Mie-theory calculations (solid lines) by Brzobohatý et al. [104], despite the reduced dimensionality of the simulations.

4.8 Radiation Pressure in Negative Index Materials

In 1968 V. Veselago proposed that materials with negative values of μ and ϵ could be used to produce optical effects not possible with naturally occurring materials [105]. Most of his predicted effects, such as negative refraction and a reversed doppler effect, have been realized [101, 106]. One that remains to be tested is his prediction that a mirror immersed in a negative index medium would be pulled towards the light source. Veselago based his prediction of negative radiation pressure on a description of momentum density derived by Rytov [107] (valid for a dispersive medium under the slowly varying envelop approximation) given by

$$\vec{G}_R = \frac{\epsilon\mu}{c^2} \vec{E} \times \vec{H} + \frac{\vec{k}}{2} \left[\frac{\partial\epsilon}{\partial\omega} \vec{E}^2 + \frac{\partial\mu}{\partial\omega} \vec{H}^2 \right], \quad (4.11)$$

where \vec{k} is the wave vector associated with the carrier phase velocity of the wave. If electromagnetic momentum density is proportional to phase velocity, then plane waves in negative-index media would carry momentum opposite to the direction of energy propagation. As a corollary, it was proposed that reversal of wave momentum would cause illuminated objects immersed in a left-handed medium to be pulled towards the light source. It will be shown here that the Abraham and Minkowski postulates do indeed predict a pull on a mirror for light incident from a negative index medium. However, this pull is likely not observable as it is smaller than the push felt by the surrounding medium during the interaction.

It has not been established that the momentum of an electromagnetic wave in a left-handed medium reverses direction relative to energy propagation, as the validity of equation 4.11 has been challenged [108]. We will use simulation to compare equation 4.11 with the five electrodynamic postulate within Table 1.1 and see if we may consider electromagnetic momentum as negative within left handed media. To calculate the magnitude of the carrier wave vector \vec{k} , we use the spatial fourier transform of the electric field profile and use the wave vector of peak intensity. Figure 4.24 tracks the electromagnetic momentum of a pulse entering a negative index medium from free space. Shown in Figure 4.24 (a) to (d), all postulates remain positive except for the Amperian form of momentum. This is because the Amperian definition of momentum is $\vec{E} \times \vec{B}$, and a property of ideal negative index materials is that \vec{E} and \vec{B} are 180° out of phase.

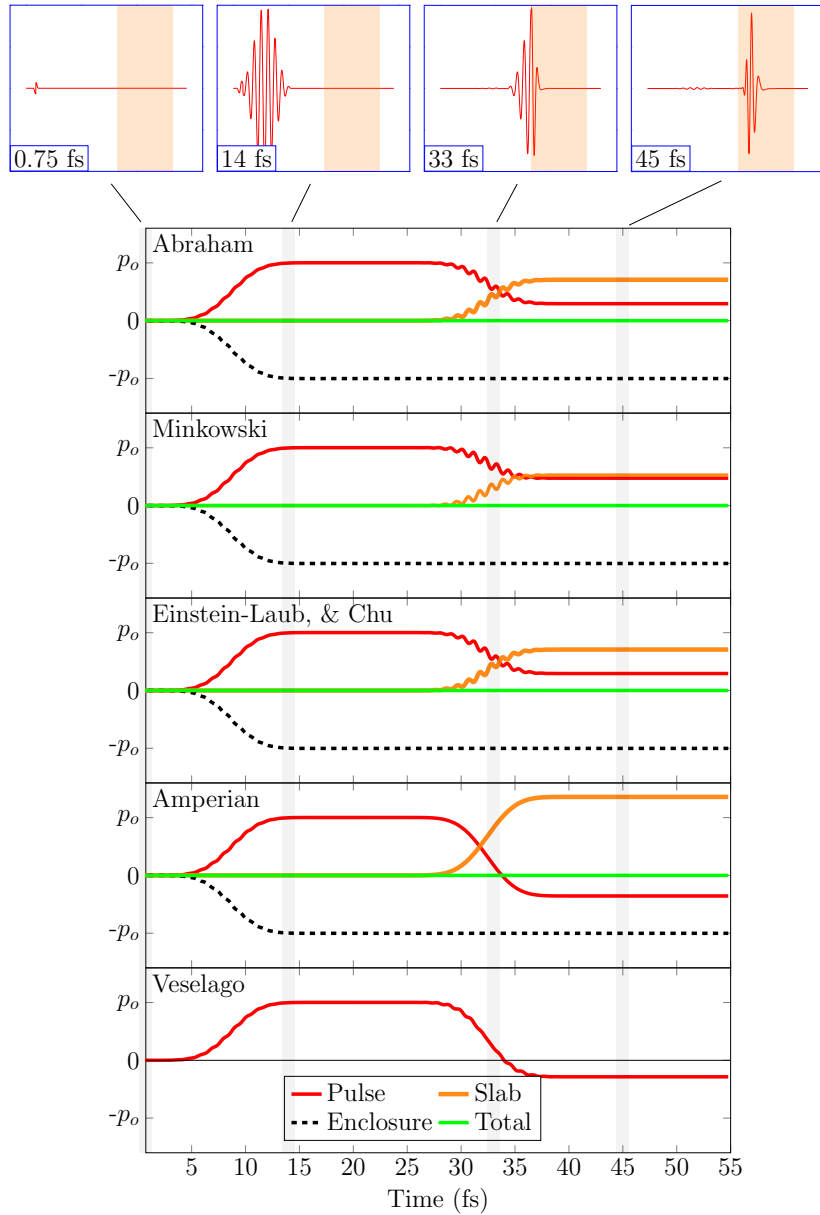


Figure 4.24: A perfectly absorbing enclosure is partially filled with a negative-index slab. The enclosure produces a pulse and the electromagnetic momentum density of the pulse is tracked as it is born from within the left end of the enclosure and then enters the negative index slab. Momentum predictions shown are the: (a) Abraham, (b) Minkowski, (c) Einstein-Laub & Chu, (d) Amperian, and (e) Veselago forms. All forms predict a decrease of the pulse electromagnetic momentum, but only the Veselago and Amperian forms are negative. The refractive index is set to $n = -1.2$ and impedance matched using the Drude model. The Drude parameters are $\epsilon_\infty = \mu_\infty = \sqrt{1.2}$, $\omega_p = 4.53 \times 10^{15}$, and $\gamma_e \approx 0$, making the medium approximately lossless.

Now we explore the prediction of negative radiation pressure, Figure 4.25 shows a pulse created within the same negative index medium as in Figure 4.24, but is now reflected from a mirror, replicating the configuration of negative radiation pressure proposed by Veselago. For both the Abraham and Minkowski cases, indeed the mirror is pulled as Veselago predicted. Unfortunately, this interesting effect is likely unobservable as the mechanical momentum imparted to the surrounding negative index medium after reflection is larger than the momentum imparted to the mirror. Each form describes reflection as a three body process involving the mirror, surrounding medium, and pulse momentum. If we consider the net momentum imparted to both the mirror and surrounding medium, the net effect would be positive. Again we see that the force on the mirror cannot be inferred from the perspective of assuming the momentum from Figure 4.24 reflects and the mirror receives momentum equal to this change. This is similar to what was shown in the Section 4.5, where the mechanical component of momentum within the surrounding medium for each form other than Minkowski was needed to calculate the total force on the mirror.

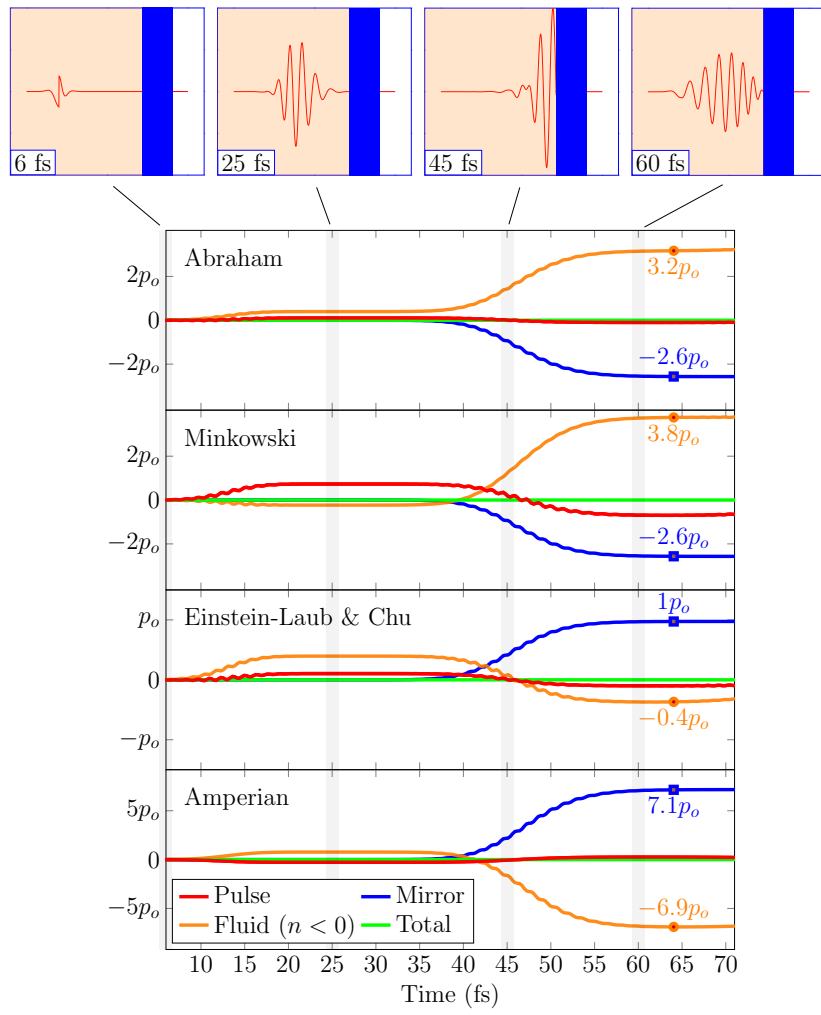


Figure 4.25: A perfectly absorbing enclosure is filled with negative index fluid and an Ag mirror. The enclosure produces a pulse and the momentum of the pulse, fluid, and mirror is tracked. Momentum predictions shown are the: (a) Abraham, (b) Minkowski, (c) Einstein-Laub & Chu, and (d) Amperian forms. Interestingly, the Abraham and Minkowski postulates do indeed predict a pull on the mirror, but this pull is smaller in magnitude than the net push received by the fluid after reflection. The Einstein-Laub and Amperian forms differ in that the mirror is pushed and the fluid is pulled. The negative index material parameters are the same in as in figure 4.24.

We create an analog to the Jones and Leslie section by simulating the pressure dependence of a mirror submerged in media with varying refractive index spanning from positive to negative values. The results are shown below in Figure 4.26. For the positive index case of a PEC, all forms predicted the same trend of an increase in pressure with the refractive index. However, for the negative index regime, we see very different behavior. The Abraham and Minkowski postulates predict an identical increase in negative pressure proportional to the index. The Einstein-Laub and Chu forms interestingly no longer agree with any other form, and produce essentially no change in pressure within the negative index regime. The Amperian form predicts a push that grows non-linearly as the surrounding medium becomes more negative.

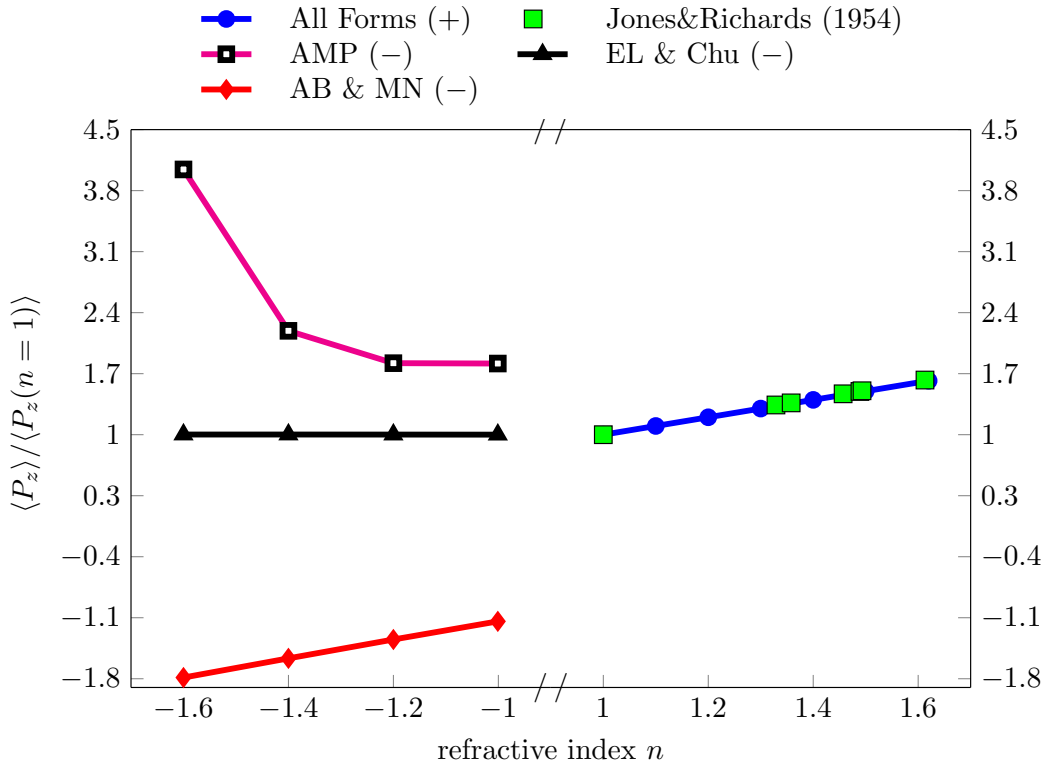


Figure 4.26: Demonstration of the momentum a mirror experiences with respect to its surrounding refractive index. All forms predict degenerate results for a refractive index $n > 1$, but differences arise for $n < 1$. The Abraham and Minkowski postulates predict degenerate trends of an increasing pull force as the index of the surrounding fluid becomes more negative. The Einstein-Laub and Chu forms predict no appreciable change in force as the index of the surrounding fluid becomes more negative. The Amperian form predicts an exponential increase in pressure as the refractive index becomes more negative.

4.8.1 Optical Tweezing With a Negative Index Bead

To further demonstrate how radiation pressure effects are different when negative index media are involved, we can look at how optical tweezing effects change when the object being “tweezed” has a negative refractive index. As shown in Section 4.7, a particle will drift towards the location of highest field intensity. Figure 4.27 (a) shows simulation results for a Gaussian beam illuminating a particle located $\approx 1\mu m$ from the beam axis and submerged in a medium with refractive index $n = 1.33$. Figure 4.27 (b) shows another simulation with identical parameters as (a), except the bead has a negative index of refraction. The negative index bead force results are different for all forms except the Amperian form, which still predicts the same push away from the beam center as in the positive index case. The other forms of Abraham, Minkowski, and Einstein-Laub, which previously predicted a pull towards the beam center, now predict a push. The Einstein-Laub form still predicts a pull towards the beam center however its magnitude relative to the other forms is quite reduced.

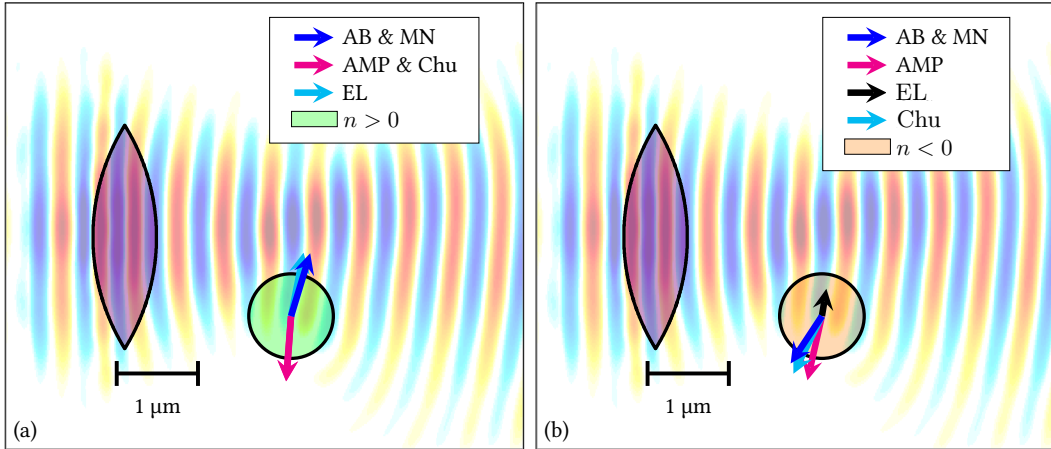


Figure 4.27: Optical tweezing of an impedance matched negative index bead under TM illumination. The bead is placed at the edge of the focal point of a continuous-wave beam ($\lambda_0 = 532$ nm) in a background medium of water ($n = 1.33$). The bead has a diameter of 820 nm and the net force is solved for the bead for two cases, positive index in (a) with ($n = 1.58$) and negative index in (b) with ($n = -1.58$) the force acting on it has been determined under the rigid body assumption by integrating the force density distribution within the bead calculated using the Minkowski (MN), Abraham (AB), Einstein-Laub (EL), Chu, and Amperian (AMP) postulates. It can be seen that the positive index results in (a) from [1] are significantly different for the negative index bead in (b). The Abraham and Minkowski, Amperian, and Chu postulates predict that a negative index bead in water is pushed away from the beam center, while the Einstein-Laub form predicts a pull into the beam focus. The negative index bead’s drude parameters are set to $\epsilon_\infty = \mu_\infty = 1.1$, $\omega_e = \omega_m = 6.21 \times 10^{15}$, and $\gamma_e = \gamma_m \approx 0$.

This hypothetical optical tweezing experiment is not experimentally feasible with present technology. However, as technology advances to possibly include situations such as Figure 4.27, this thought experiment reaffirms our current understanding of electrodynamic

modeling needs to also advance. This was another example of how the five forms listed in Table 1.1 are experimentally distinguishable and enables further work to be done in understanding the behavior of each form in the negative index regime.

Chapter 5: Conclusion

This thesis presents a consolidated analysis of radiation pressure observations using classical electrodynamics described by five different formulations. The analysis included theoretical considerations of center-of-mass translation presented by Balazs [29], radiation pressure measurements on mirrors [13, 14], observations of radiation-induced deformation of fluid interfaces [15, 16, 17, 18, 19, 20], optical tweezers, [96, 103, 104], and thought experiments involving radiation pressure in negative index materials [105]. Out of the five electrodynamic theories considered, namely the Abraham, Minkowski, Einstein-Laub, Amperian, and Chu forms, at least two were shown to reproduce each observable considered. Each electromagnetic formulation was tested against their respective ability to conserve energy, momentum, and center-of-mass velocity. Within this thesis, the results obtained were:

- The symmetric form of the Minkowski and Amperian formulations can conserve center-of-mass velocity, but both require a surface energy term whose existence must be rationalized. A simple experiment was carried out where this surface energy was predicted to present itself as a measurable temperature difference across the entrance and exit faces of an illuminated waveguide. No temperature difference was observed.
- Section 4.5 simulated past experiments done to measure the force on metallic and dielectric mirrors while submerged in liquids with different values of refractive index [13, 14]. For the 1978 dielectric mirror experiments, it was shown that the Einstein-Laub, Chu, and Amperian forms can predict a decrease in pressure with the surrounding refractive index depending on the order of the dielectric layers, the Abraham and Minkowski forms maintain the same behavior for both possible orderings. The layer ordering was never recorded for the original experiment, this means a second experiment could be done using both possible layer orderings.
- The two dimensional analysis in Section 4.6 demonstrated that the Chu and Amperian forms could be differentiated by repeating the Ashkin or Casner experiments and comparing results for TM and TE illumination.

- The results of two optical tweezing experiments were reproduced, the tendency of a particle being tweezed to move towards the beam's focus [96], and the ability of two interfering beams to pull on a particle [104]. Results agreed with [95] that both the Abraham and Minkowski forms are sufficient to predict the forces involved in optical tweezing. Polarization dependence was found for the Einstein-Laub, Chu, and Amperian forms that may be testable.
- Lastly, in Section 4.8 we considered a thought experiment done by V. Veselago who predicted electromagnetic momentum in negative index media could be considered negative, and that a mirror immersed in a negative index medium would be pulled towards the light source. It was shown that for an ideal case only the Amperian form predicts an electromagnetic momentum density that is negative. For his second prediction we demonstrated that the Abraham and Minkowski forms do indeed pull on a mirror, but the pull force is less than the push that exists outside of the mirror in the surrounding medium. As well, when a negative-index analogue of the Jones and Leslie experiments was re-created in Section 4.8 very distinct differences were seen between the five forms. It was also shown that optical tweezing effects reversed from a pull towards the beam focus to a push for the Abraham and Minkowski forms if the object being moved was negative index.

Rigorous simulations of five electrodynamic models demonstrated several situations where each model yielded different predictions. This large catalog of results agree with the prevalent argument that the definition of electrodynamic theory is not arbitrary. Differences in both theoretical and experimental predictions of each form were shown and plausible experiments have been suggested to isolate a single true electrodynamic theory.

Appendix A: Speeding up Matlab Code

Figure Handles

Matlab is used extensively in research applications. When used for simulation, real time plotting is common to help the user visualize their results. It is not immediately obvious to the typical Matlab user that their code can run much faster depending on how data is plotted in a figure window. Updating the handle on a plot can speed up your code exponentially. An example of a slow plotting method and a fast plotting method are shown below in Figure 5.1, speedup will vary between computers but was ≈ 10 times faster for the computer used in this example. If your code uses many surface plots in two dimensions, it would not be unusual to see speedups of 500% by using handles instead of recalling the "figure" function every time a plot is to be updated.

```

1 %% Slow Plotting
2 f=60; % Frequency [Hz]
3 T=1/f; % Period [s]
4 dt=T/200; % Time step [s]
5
6 t=[0:dt:4*T]; % Time axis [s]
7 Nt=length(t); % # of points[#]
8 E=zeros(1,Nt); % Electric field [V/m]
9
10 for n=1:Nt
11
12 E(n)=sin(2*pi*f*t(n));
13 figure(1)
14 plot(t(1:Nt),E(1:Nt));
15 xlabel('time')
16 ylabel('E-field')
17
18 end

```

```

1 %% Fast Plotting
2 f=60; % Frequency [Hz]
3 T=1/f; % Period [s]
4 dt=T/200; % Time step [s]
5
6 t=[0:dt:4*T]; % Time axis [s]
7 Nt=length(t); % # of points[#]
8 E=zeros(1,Nt); % Electric field [V/m]
9
10 figure(1)
11 plot_handle=plot(t,E);
12 xlabel('time')
13 ylabel('E-field')
14
15 for n=1:Nt
16 E(n)=sin(2*pi*f*t(n));
17 set(plot_handle,'XDATA',t,'YDATA',E);
18 end

```

Figure 5.1: A minimum working example (MWE) to demonstrate how to use handles to update a figure as opposed to re-calling the “figure” function. The code above will produce a figure of a simple sine wave.

Vectorization

When possible, a second method is to replace any loops in the code with a vector , Matlab is more efficient at dealing with matrixies as vectors rather than loops. Figure 5.2 below shows Matlab code that will plot a 2D surface of a plane wave varying in time, the code takes ≈ 10 seconds to run using `for` loops, and ≈ 4 seconds when vectorized as shown.

```

1 f=60;                                % Frequency [Hz]
2 T=1/f;                                 % Period [s]
3 lambda=10;                             % Wavelength [m]
4 k=2*pi/lambda;                         % Wavevector [rad/m]
5 dt=T/90;                               % Time step [s]
6 dx=lambda/30;                           % Space step [m]
7 dy=lambda/30;                           % Space step [m]
8
9 t=[0:dt:4*T];                          % t axis [s]
10 x=[0:dx:3*lambda];                   % x axis [m]
11 y=[0:dy:3*lambda];                   % y axis [m]
12
13 Nt=length(t);                        % # of t points[#]
14 Nx=length(x);                        % # of x points[#]
15 Ny=length(y);                        % # of y points[#]
16
17 E=zeros(Nx,Ny,Nt);                  % Electric field [V/m]
18
19 figure(1)
20 plot_handle=surf(x,y,E(:,:,1));
21 shading flat
22 xlabel('x [m]')
23 ylabel('y [m]')
24 zlabel('E(x,n)')
25 h_title=title('');
26 start_time=tic;                      % start timer
27
28 for n=1:Nt
29   for i=1:Nx
30     for j=1:Ny
31       E(i,j,n)=ones(length(y(j)),1)*sin(k*x(i)-2*pi*f*t(n));
32     end
33   end
34   % update plot
35   set(plot_handle,'ZDATA',E(:,:,n));
36   set(h_title,'String',[ 'time= ' num2str(toc(start_time))]) Vectorized
37   drawnow
38 end
39
40 %% Vectorized loop (faster)
41 for n=1:Nt
42   i=1:Nx;
43   j=1:Ny;
44   E(i,j,n)=ones(length(y(j)),1)*sin(k*x(i)-2*pi*f*t(n));
45 ...

```

Figure 5.2: An example to demonstrate how vectorizing for loops improves the speed of matlab code. A surface plot of a simple plane wave is sped up by replacing loops through individual values such as `for i=1:Nx;`, to simply the whole vector `i=1:Nx;`.

Bibliography

- [1] M. Bethune-Waddell and K. J. Chau. “Simulations of radiation pressure experiments narrow down the energy and momentum of light in matter”. In: *Reports on Progress in Physics* 78.12 (2015), p. 122401.
- [2] J. C. Maxwell. *A Treatise on Electricity and Magnetism*. Vol. 2. Dover, 1891.
- [3] P. N. Lebedev. “Untersuchungen über die Druckkräfte des Lichtes[Investigations Over the compressive forces of light]”. In: *Ann. Phys.* 6 (1900), 433–458.
- [4] E. F. Nichols and G. F. Hull. “A Preliminary communication on the pressure of heat and light radiation”. In: *Phys. Rev. (Series 1)* 13 (1901), 307–320.
- [5] E. F. Nichols and G. F. Hull. “The pressure due to radiation. (Second Paper.)” In: *Phys. Rev. (Series 1)* 17 (1903), 26–50.
- [6] H. Minkowski. “Die Grundgleichungen für die elektromagnetischen Vorgänge in bewegten Körpern”. In: *Nachr. Ges. Wiss. Göttingen* (1908), 53–111.
- [7] M. Abraham. “Zur Elektrodynamik bewegter Körper[The electrodynamics of moving bodies]”. In: *R. C. Circ. Mat. Palermo* 28 (1909), 1–28.
- [8] A. Einstein and J. Laub. “Über die elektromagnetischen Grundgleichungen für bewegte Körper[About the electromagnetic fundamental equations for moving bodies]”. In: *Ann. Phys.* 26 (1908). Trans. A. Beck *The Collected Papers of Albert Einstein*, 329–348, Princeton University Press, Princeton, 1989., 541–550.
- [9] R. M. Fano, L. J. Chu, and R. B. Adler. *Electromagnetic fields, energy, and forces*. New York: John Wiley & Sons, 1960.
- [10] L. J. Chu, H. Haus, and P. Penfield Jr. “The force density in polarizable and magnetizable fluids”. In: *Proc. IEEE* 54 (1966), 920–935.
- [11] P. Penfield and H. A. Haus. *Electrodynamics of Moving Media*. Cambridge: M.I.T. Press, 1967.
- [12] Y. N. Obukhov and F. W. Hehl. “Electromagnetic energy-momentum and forces in matter”. In: *Phys. Lett. A* 311 (2003), 277–284.

- [13] R. V. Jones and J. C. S. Richards. “The Pressure of Radiation in a Refracting Medium”. In: *Proc. R. Soc. Lond.* 221 (1954), 480–498.
- [14] R. V. Jones and B. Leslie. “The Measurement of Optical Radiation Pressure in Dispersive Media”. In: *Proc. R. Soc. Lond. A* 360 (1978), 347–363.
- [15] A. Ashkin and J. M. Dziedzic. “Radiation pressure on a free liquid surface”. In: *Phys. Rev. Lett.* 30 (1973), 139–142.
- [16] A. Casner and J-P. Delville. “Giant deformations of a liquid-liquid interface induced by the optical radiation pressure”. In: *Phys. Rev. Lett.* 87 (2001), 054503.
- [17] A. Casner, J-P. Delville, and I. Brevik. “Asymmetric optical radiation pressure effects on liquid interfaces under intense illumination”. In: *J. Opt. Soc. Am. B* 20 (2003), 2355–2362.
- [18] A. Casner and J-P. Delville. “Laser-Induced hydrodynamic instability of fluid interfaces”. In: *Phys. Rev. Lett.* 90 (2003), 144503.
- [19] R. Wunenburger, A. Casner, and J-P. Delville. “Light-induced deformation and instability of a liquid interface. I. Statics”. In: *Phys. Rev. E* 73 (2006), 036314.
- [20] R. Wunenburger, A. Casner, and J-P. Delville. “Light-induced deformation and instability of a liquid interface. II. Dynamics”. In: *Phys. Rev. E* 73 (2006), 036315.
- [21] A. F. Gibson, M. F. Kimmitt, and A. C. Walker. “Photon drag in germanium”. In: *Appl. Phys. Lett.* 17 (1970), 75–77.
- [22] A. M. Danishevskii, A. A. Kastal'skii, S. M. Ryvkin, and I. D. Yaroshetskii. “Dragging of free carriers by photons in direct interband transitions in semiconductors”. In: *Sov. Phys. JETP* 31 (1970), 292–295.
- [23] A. F. Gibson, M. F. Kimmitt, A. O. Koohian, D. E. Evans, and G. F. D. Levy. “A study of radiation pressure in a refractive medium by the photon drag effect”. In: *Proc. R. Soc. Lond. A* 370 (1980), 303–311.
- [24] G. K. Campbell, A. E. Leanhardt, J. Mun, M. Boyd, E. W. Streed, W. Ketterle, and D. E. Pritchard. “Photon recoil momentum in dispersive media”. In: *Phys. Rev. Lett.* 94 (2005), 170403.
- [25] F. N. H. Robinson. “Electromagnetic stress and momentum in matter”. In: *Phys. Rep.* 16 (1975), 313–354.
- [26] Z. Mikura. “Variational formulation of the electrodynamics of fluids and its application to the radiation pressure problem”. In: *Phys. Rev. A* 13 (1976), 2265–2275.
- [27] I. Brevik. “Experiments in phenomenological electrodynamics and the electromagnetic energy-momentum tensor”. In: *Phys. Rep.* 52 (1979), 133–201.

- [28] B. A. Kemp and T. M. Grzegorczyk. “The observable pressure of light in dielectric fluids”. In: *Opt. Lett.* 36 (2011), 493–495.
- [29] N. L. Balazs. “The energy-momentum tensor of the electromagnetic field inside matter”. In: *Phys. Rev.* 91 (1953), 408–411.
- [30] A. Einstein. “Das Prinzip von der Erhaltung der Schwerpunktsbewegung und die Trägheit der Energie[The principle of conservation of the center of gravity and the inertia of energy]”. In: *Ann. Phys.* 20 (1906), 627–633.
- [31] L. D. Landau and E. M. Lifshitz. *Electrodynamics of Continuous Media, Second Edition*. Vol. 8. Course of Theoretical Physics. 1984.
- [32] M. Kranyš. “About the equivalence of Abraham’s and Minkowski’s electrodynamics”. In: *Can. J. Phys.* 57 (1979), 1022–1026.
- [33] R. N. C. Pfeifer, T. A. Nieminen, N. R. Heckenberg, and H. Rubinsztein-Dunlop. “Momentum of an electromagnetic wave in dielectric media”. In: *Rev. Mod. Phys.* 79 (2007), pp. 1197–1216.
- [34] D. F. Nelson. “Momentum, pseudomomentum, and wave momentum: Toward resolving the Minkowski-Abraham controversy”. In: *Phys. Rev. A* 44 (1991), 3985–3996.
- [35] E. A. Hinds and A. M. Barnett. “Momentum exchange between light and a single atom: Abraham or Minkowski?” In: *Phys. Rev. Lett.* 102 (2009), 050403.
- [36] P. W. Milonni and R. W. Boyd. “Momentum of light in a dielectric medium”. In: *Adv. Opt. Phot.* 2 (2010), 519–553.
- [37] S. M. Barnett. “Resolution of the Abraham-Minkowski dilemma”. In: *Phys. Rev. Lett.* 104 (2010), 070401.
- [38] C. Baxter and R. Loudon. “Radiation pressure and the photon momentum in dielectrics”. In: *J. Mod. Opt.* 57 (2010), 830–842.
- [39] B. A. Kemp. “Resolution of the Abraham-Minkowski debate: Implications for the electromagnetic wave theory of light in matter”. In: *J. Appl. Phys.* 109 (2011), 111101.
- [40] R. V. Jones. “Radiation pressure of light in a dispersive medium”. In: *Proc. R. Soc. Lond. A* 360 (1978), 365–371.
- [41] R. Peierls. “The momentum of light in a refracting medium”. In: *Proc. R. Soc. Lond. A* 347 (1976), 475–491.
- [42] M. Mansuripur. “Radiation pressure and the linear momentum of the electromagnetic field”. In: *Opt. Express* 12 (2004), 5375–5401.

- [43] M. Mansuripur. “Radiation pressure and the linear momentum of light in dispersive dielectric media”. In: *Opt. Express* 13 (2005), 2245–2250.
- [44] M. Mansuripur, A. R. Zakharian, and J. V. Moloney. “Radiation pressure on a dielectric wedge”. In: *Opt. Express* 13 (2005), 2064–2074.
- [45] J. C. Garrison and R. Y. Chiao. “Canonical and kinetic forms of the electromagnetic momentum in an ad hoc quantization scheme for a dispersive dielectric”. In: *Phys. Rev. A* 70 (2004), 053826.
- [46] P. L. Saldanha. “Division of the momentum of electromagnetic waves in linear media into electromagnetic and material parts”. In: *Opt. Express* 18 (2011), 2258–2268.
- [47] I. Brevik and S. Å. Ellingsen. “Electromagnetic momentum conservation in media”. In: *Ann. Phys.* 326 (2011), 754–769.
- [48] M. Mansuripur. “Momentum exchange effect”. In: *Nature Photon.* 7 (2013), 765–766.
- [49] M. V. Laue. “Zur Minkowskischen Elektrodynamik der bewegten Körper.[The Minkowski electrodynamics of moving bodies]”. In: *Z. Physik* 128 (1950), 387–394.
- [50] J. H. Poynting. “On the transfer of energy in the electromagnetic field”. In: *Phil. Trans. R. Soc.* 175 (1884), 343–361.
- [51] J. D. Jackson. *Magnetic Actuators and Sensors, 2nd Edition*. John Wiley and Sons, 2014.
- [52] “Pull Force Case 3”. In: *K&J Magnetics Inc.* (2015). Accessed: 2015-11-01. URL: <https://www.kjmagnetics.com/largergraph.asp?CI=3&pName=DAC>.
- [53] N. L. Balazs. “On the propagation of energy in elastic media”. In: *Proc. Phys. Soc. A* 67 (1954), 726–727.
- [54] L. D. Landau and E. M. Lifshitz. *The Classical Theory of Fields*. Vol. 2. Course of Theoretical Physics. 1951. ISBN: 978-0-08-030275-1. DOI: <http://dx.doi.org/10.1016/B978-0-08-030275-1.50025-4>.
- [55] J. D. Jackson. *Classical Electrodynamics, Third Edition*. John Wiley and Sons, 1999.
- [56] C. S. Helrich. *The Classical Theory of Fields-Electromagnetism*. Vol. 2. Graduate Texts in Physics. Springer, 2012.
- [57] M. Abraham. “Zur Frage der Symmetrie des elektroniagnetischen Spannungstensors[On the issue of symmetry of the electromagnetic stress tensor]”. In: *Annal. Phys.* 349 (1914), 537–544.
- [58] D. Griffths and I. M. Smith. *Numerical methods for engineers*. Chapman & Hall, 2006.

- [59] A. Taflove and S. C. Hagness. *Computational Electrodynamics: The Finite-Difference Time-Domain Method*, 3rd Ed. Norwood, MA: Artec House, 2005.
- [60] K. Yee. “Numerical solution of initial boundary value problems involving Maxwell’s equations in isotropic media”. In: vol. 13. 3. IEEE Transactions on Antennas and Propagation, 1966.
- [61] S. N. Makarov. *Antenna and EM Modeling with Matlab*. New York: Wiley & Sons, 2002.
- [62] L. Yaxun and C. D. Sarris. “AMR-FDTD: a dynamically adaptive mesh refinement scheme for the finite-difference time-domain technique”. In: *Antennas and Propagation Society International Symposium, 2005 IEEE*. Vol. 1A. 2005, 134–137.
- [63] G. Tryggvason. “A Front-tracking/Finite-Volume Navier-Stokes Solver for Direct Numerical Simulations of Multiphase Flows”. In: (2012). Unpublished. URL: www3.nd.edu/~gtryggva/MultiphaseDNS/DNS-Solver.pd.
- [64] G. Tryggvason, B. Bunner, A. Esmaeeli, D. Juric, N. Al-Rawahi, W. Tauber W, J. Han, S. Nas, and J-Y. Jan. “A front-tracking method for the computations of multiphase flow”. In: *J. Comp. Phys.* 169 (2001), 708–759.
- [65] M. Mansuripur. *Momentum in Classical Electrodynamics*.: Bentham Books, 2011.
- [66] S. M. Barnett and R. Loudon. “The enigma of optical momentum in a medium”. In: *Phil. Trans. R. Soc. A* 368 (2010), 927–939.
- [67] K. J. Chau and H. Lezec. “Revisiting the Balazs thought experiment in the case of a left-handed material: electromagnetic-pulse-induced displacement of a dispersive, dissipative negative-index slab”. In: *Opt. Express* 20 (2012), 10138–10162.
- [68] M. Sadiku. *Elements of Electromagnetics*. 4th ed. Oxford University Press, 2007.
- [69] D. M. Pozar. *Microwave Engineering*. 3rd ed. Wiley, 2005.
- [70] J. Blumm, A. Lindermann, M. Meyer, and C. Strasser. “Characterization of PTFE Using Advanced Thermal Analysis Techniques”. In: *Int. J. Thermophys.* 31 (2008), 1919–1927.
- [71] I. Perepechko. *Low-Temperature Properties of Polymers*.: Elsevier, 2013.
- [72] M. Mansuripur. “Nature of electric and magnetic dipoles gleaned from the Poynting theorem and the Lorentz force law of classical electrodynamics”. In: *Opt. Commun.* 284 (2011), 594–602.
- [73] A. Rohrbach and E. H. K. Stelzer. “Optical trapping of dielectric particles in arbitrary fields”. In: *J. Opt. Soc. Am. A* 18 (2001), 839–853.

- [74] M. Bell and S. E. Green. “On radiometer action and the pressure of radiation”. In: *Proc. Phys. Soc.* 45 (1933), 320–357.
- [75] M. Mansuripur. “Radiation pressure on submerged mirrors: implications for the momentum of light in dielectric media”. In: *Opt. Express* 15 (2007), 2677–2682.
- [76] M. Mansuripur. “Deducing radiation pressure on a submerged mirror from the doppler shift”. In: *Phys. Rev. A* 85 (2012), 023807.
- [77] K. J. Webb. “Dependence of the radiation pressure on the background refractive index”. In: *Phys. Rev. Lett.* 111 (2013), 043602.
- [78] C. J. Sheppard and B. A. Kemp. “Optical pressure deduced from energy relations within relativistic formulations of electrodynamics”. In: *Phys. Rev. A* 89 (2014), 013825.
- [79] E. Palik and G. Ghosh. *Handbook on optical constants of solids*. San Diego: Academic Press, 1998.
- [80] P. B. Johnson and R. W. Christy. “Optical constants of the noble metals”. In: *Phys. Rev. B* 4 (1972), 4370–4379.
- [81] B. A. Kemp. “Macroscopic theory of optical momentum”. In: *Prog. Opt.* 60 (2015), 437–488.
- [82] M. G. Burt and R. Peierls. “The momentum of a light Wave in a refracting medium”. In: *Proc. R. Soc. Lond. A* 333 (1973), 149–156.
- [83] N. G. C. Astrath, G. V. B. Lukasievicz, L. C. Malacarne and S. E. Bialkowski. “Surface deformation effects induced by radiation pressure and electrostriction forces in dielectric solids”. In: *Appl. Phys. Lett.* 102 (2013), 231903.
- [84] J. P. Gordon. “Radiation Forces and Momenta in Dielectric”. In: *Phys. Rev. A* 8 (1973), 14–21.
- [85] R. Loudon. “Radiation pressure and momentum in dielectrics”. In: *Fortschr. Phys.* 52 (2004), 1134–1140.
- [86] N. G. C. Astrath, L. C. Malacarne, M. L. Baesso, G. V. B. Lukasievicz and S. E. Bialkowski. “Unravelling the effects of radiation forces in water”. In: *Nat. Commun.* 5 (2014), 023826.
- [87] N. S. Aanensen, S. Å. Ellingsen, and I. Brevik. “Theoretical considerations of laser-induced liquid-liquid interface deformation”. In: *Phys. Scr.* 87 (2013), 055402.
- [88] M. Mansuripur. “On the foundational equations of the classical theory of electrodynamics”. In: *Resonance* 18 (2013), 130–155.

- [89] A. Casner. “Déformations, manipulations et instabilités d’interfaces liquides induites par la pression de radiation d’une onde laser”. PhD thesis. University of Bordeaux, 2002.
- [90] K. C. Neumann, E. H. Liou, G. F. Bergman, and S. M. Block. “Characterization of photodamage to Escherichia coli in optical traps”. In: *Biophys. J.* 77 (1999), 2856–2863.
- [91] M. D. Wang, H. Yin, R. Landick, J. Gelles, and S. M. Block. “Stretching DNA with optical tweezers”. In: *Biophys. J.* 72 (1997), 1335–1346.
- [92] P. H. Jones, O. M. Marago, and G. Volpe. *Optical Tweezers: Principles and Applications*. Cambridge University Press, 2016.
- [93] D. G. Grier. “A revolution in optical manipulation”. In: *Nature* 424 (2003), 810–816.
- [94] J. P. Barton, D. R. Alexander and S. A. Schaub. “Theoretical determination of net radiation force and torque for a spherical particle illuminated by a focused laser beam”. In: *J. Appl. Phys.* 66 (1989), 4594–4602.
- [95] R. N. C. Pfeifer, T. A. Nieminen, N. R. Heckenberg and H. Rubinsztein-Dunlop. “Optical tweezers and paradoxes in electromagnetism”. In: *J. Opt.* 13 (2011), 044017.
- [96] A. Ashkin. “Acceleration and trapping of particles by radiation pressure”. In: *Phys. Rev. Lett.* 24 (1970), 156–159.
- [97] P. L. Marston. “Axial radiation force of a Bessel beam on a sphere and direction reversal of the force”. In: *J. Acoust. Soc. Am.* 120 (2006), 3518.
- [98] S. Sukhov and A. Dogariu. “On the concept of “tractor beams””. In: *Opt. Lett.* 35 (2010), 3847–3849.
- [99] S. Sukhov and A. Dogariu. “Negative nonconservative Forces: Optical “Tractor Beams” for arbitrary objects”. In: *Phys. Rev. Lett.* 107 (2011), 203602.
- [100] A. Novitsky, C-W. Qiu and H. Wang. “Single gradientless light beam drags particles as tractor beams”. In: *Phys. Rev. Lett.* 107 (2011), 203601.
- [101] J. Chen, Y. Wang, B. Jia, T. Geng, X. Li, L. Feng, W. Qian, B. Liang, X. Zhang, M. Gu, and S. Zhuang. “Observation of the inverse Doppler effect in negative-index materials at optical frequencies”. In: *Nat. Phot.* 5 (2011), 239–245.
- [102] D. B. Ruffner and D. G. Grier. “Optical conveyors: a class of active tractor beams”. In: *Phys. Rev. Lett.* 109 (2012), 163903.
- [103] V. Kajorndejnukul, W. Ding, S. Sukhov, C-W. Qiu and A. Dogariu. “Linear momentum increase and negative optical forces at dielectric interface”. In: *Nature Photonics* 7 (2013), 787–790.

- [104] O. Brzobohatý, V. Karásek, M. Šiler, L. Chvátal, T. Čižmár and P. Zemánek. “Experimental demonstration of optical transport, sorting and self-arrangement using a ‘tractor beam’”. In: *Nature Photon.* 7 (2013), 123–127.
- [105] V. G. Veselago. “The Electrodynamics of Substances with Simultaneously Negative values of ϵ and μ ”. In: *Sov. Phys. Usp.* 10 (1968), 509–514.
- [106] R. A. Shelby, D. R. Smith, and S. Schultz. “Experimental Verification of a Negative Index of Refraction”. In: *Science* 292 (5514 2001), 77–79.
- [107] S. M. Rytov. “Some Theorems on the group velocity of electromagnetic waves”. In: *J. Exp. Th. Phys.* 17 (1947), 930–936.
- [108] V. P. Makarov, and A. A. Rukhadze. “Negative group velocity electromagnetic waves and the energy-momentum tensor”. In: 54 (12 2011), pp. 1285–1296.